Reduced Basis Approximations for Electromagnetic Applications

Dissertation

zur Erlangung des akademischen Grades

doctor rerum naturalium
(Dr. rer. nat.)

von M.Sc. Martin Heß

geb. am 27. August 1983 in Berlin

genehmigt durch die Fakultät für Mathematik
der Otto-von-Guericke-Universität Magdeburg

Gutachter: Prof. Dr. Peter Benner
Prof. Dr. Jan Hesthaven

eingereicht am: 22.02.2016
Verteidigung am: 22.07.2016

Heß, Martin
Reduced Basis Approximations for Electromagnetic Applications
Dissertation, Fakultät für Mathematik
Otto-von-Guericke-Universität Magdeburg, July 2016

Publications

Parts of this thesis have been published or are accepted for publication, in particular:

Chapter 4 is an extended and revised version of the results published in

- M. W. Hess and P. Benner, Fast Evaluations of Time-Harmonic Maxwell's Equations Using the Reduced Basis Method, IEEE Transactions on Microwave Theory and Techniques, 2013, volume 61, issue 6, pages 2265 - 2274, [HB13a],
- M. W. Hess and P. Benner, A Reduced Basis Method for Microwave Semiconductor Devices with Geometric Variations, COMPEL - The International Journal for Computation and Mathematics in Electrical and Electronic Engineering, 2014, volume 33, issue 4, pages 1071 - 1081, [HB14].

Parts of the results found in Chapter 5 are published in

- M. W. Hess, S. Grundel and P. Benner, Estimating the Inf-Sup Constant in Reduced Basis Methods for Time-Harmonic Maxwell's Equations, IEEE Transactions on Microwave Theory and Techniques, 2015, volume 63, issue 11, pages 3549 - 3557, [HGB15],
- M. W. Hess and P. Benner, Reduced Basis Generation for Maxwell's Equations by Rigorous Error Estimation, Proceedings of 19th International Conference on the Computation of Electromagnetic Fields (COMPUMAG 2013), Paper PD2-10 (2 pp.), 2013, [HB13b].

Chapter 6 is an extended and revised version of the results accepted for publication in

- M. W. Hess and P. Benner, Reduced Basis Modeling for Uncertainty Quantification of Electromagnetic Problems in Stochastically Varying Domains, 10th International Conference on Scientific Computing in Electrical Engineering, Springer Series "Mathematics in Industry": accepted for publication.

Acknowledgement

First of all, I thank my PhD supervisor Prof. Peter Benner for introducing me to the field of model order reduction and giving me the opportunity to carry out this work in his group. I am grateful for his support and trust over the past years.

I thank Prof. Jan Hesthaven for the opportunity to conduct a research stay in his group and the helpful advice I received while working at EPFL.

I also thank Prof. Christopher Beattie, Prof. Karen Veroy, Dr. Martin Stoll, Dr. Jens Saak and Dr. Sara Grundel for fruitful discussions, opening up new directions of research for me.

I thank my colleagues at the MPI Magdeburg, in particular Dr. Tobias Breiten, Dr. Matthias Voigt, Patrick Kürschner, Yongjin Zhang and Akwum Onwunta for creating a great and fun work environment.

Abstract

The semiconductor industry requires increasingly complex simulations, as with reduced feature sizes and increasing working frequencies, parasitic effects like crosstalk and signal delay need to be accounted for. Due to increasing working frequencies and reduced feature sizes, the numerical solution of Maxwell's equations to simulate model behaviour is desirable. To optimize model behaviour, parametrizations are incorporated into the model. To deal with the significant computational effort of exploring the model behavior over the parameter domain, parametric model order reduction is used.

In this thesis, the reduced basis parametric model order reduction technique is applied to electromagnetic problems. The focus is on microwave devices governed by the time-harmonic Maxwell's equations in first and second order form, with considered parametric variations in frequency, geometry and material. The three-dimensional models resemble real-world problems encountered in electrical engineering and this work shows how the reduced basis method can be applied successfully in this application area. In particular, a coplanar waveguide, a branchline coupler and a printed circuit board is used for numerical simulations with up to 233060 degrees of freedom.

Furthermore, stochastically varying domains are considered, where the reduced basis computational approach is used to sample statistical moments. The weighted reduced basis method allows to take the underlying probability distribution into account.

To certify the approximation error between the full order model and reduced order model, rigorous error estimation is required. This topic is explored in depth and multiple methods and techniques are compared, whereby the MinRes estimator for the inf-sup stability constant shows the most promising results.

On one example, the reduced basis technique is compared with two other commen model reduction techniques, namely the proper orthogonal decomposition and the moment matching.

Moreover, a time-dependent example of Maxwell's equations with stochastic temporal dispersion is considered. The derivation of a coupled system in the electric field and the polarization is shown and the reduced basis machinery for time-dependent problems is applied. Also, stochastic coefficients are taken into account for the parameters of the dispersion.

Zusammenfassung

Die Halbleiterindustrie benötigt zunehmend komplexere Simulationen, da mit kleineren Abmessungen und höheren Frequenzen parasitische Effekte wie crosstalk und Signalverzögerung miteinbezogen werden müssen. Aufgrund höherer Frequenzen und kleinerer Abmessungen wird die numerische Lösung der Maxwellschen Gleichungen für die Simulation des Modellverhaltens wünschenswert. Für die Optimierung des Modellverhaltens wird das Modell parametrisiert. Um den signifikanten numerischen Aufwand zu leisten, den die Auswertung des Modellverhaltens über den Parameterbereich beinhaltet, werden parametrische Modellreduktionsverfahren benutzt.

In dieser Arbeit wird die Reduzierte Basis Methode als Methode der parametrischen Modellreduktion auf elektromagnetische Probleme angewandt. Der Fokus liegt auf Mikrowellenbauelementen, die von den zeitharmonischen Maxwellschen Gleichungen in der Formulierung erster oder zweiter Ordnung bestimmt werden. Die betrachteten Parametervariationen sind die Frequenz, die Geometrie und Materialkoeffizienten. Die dreidimensionalen Modelle spiegeln realistische Beispiele aus der Elektrotechnik wieder und diese Arbeit zeigt, wie die Reduzierte Basis Methode erfolgreich in diesem Gebiet angewendet werden kann. Im Einzelnen wird ein koplanarer Wellenleiter, ein Koppler und eine Schaltungsplatine mit bis zu 233060 Freiheitsgraden betrachtet.

Des Weiteren werden stochastische Definitionsbereiche betrachtet, wobei der Reduzierte Basis Ansatz benutzt wird, um die statistischen Momente zu samplen. Die gewichtete Reduzierte Basis Methode ermöglicht es, die zugrunde liegende Wahrscheinlichkeitsdichte miteinzubeziehen.

Um den Approximationsfehler zwischen dem hochdimensionalen und reduzierten Modell zu zertifizieren, ist eine rigorose Fehlerschätzung notwendig. Dieses Thema wird im Detail untersucht und mehrere Methoden und Techniken werden verglichen, wobei sich der MinRes Schätzer für die inf-sup Stabilitätskonstante als aussichtsreich erweist.

An einem Beispiel wird die Reduzierte Basis Methode mit zwei anderen häufig genutzten Modellreduktionsverfahren verglichen, nämlich der 'proper orthogonal decomposition' und dem 'moment matching'.

Außerdem wird ein zeitabhängiges Beispiel der Maxwellschen Gleichungen mit stochastischer zeitlicher Dispersion betrachtet. Die Herleitung eines gekoppelten Systems im elektrischen Feld und der Polarisation wird gezeigt und die Reduzierte Basis Methode für zeitabhängige Probleme angewandt. Stochastische Koeffizienten werden hier ebenfalls betrachtet für die Parameter der Dispersion.

Contents

List of Figures

List of Tables

1 Introduction

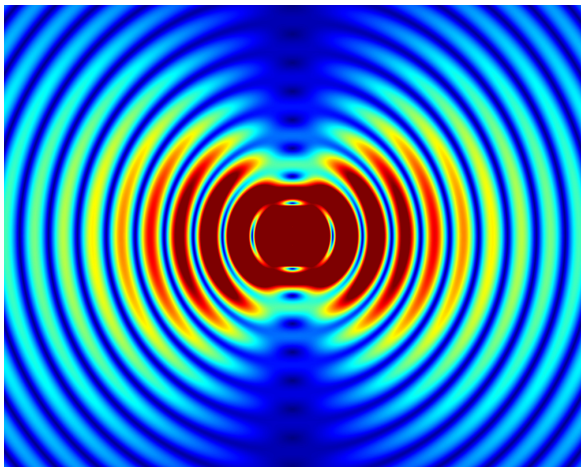

Figure 1.1: Hertzian dipole as a source of electromagnetic radiation[1].

1.1 Motivation

The simulation of Maxwell's equations gives insight into electromagnetic (EM) and optic phenomena and is used in industry as part of efficient production.

For instance, the semiconductor industry depends on the ability to simulate device behavior. Building actual prototypes is a long and expensive process, so that the number of prototypes should be kept to a minimum. In chip design, the increasing clock frequencies and miniaturization cause various effects like crosstalk [DLK10]. The design is unimaginable without an efficient simulation of complex, parametrized models to high accuracy.

Due to improved algorithms and computing power, more and more complex simulations can be performed. Parametrized models can benefit from model reduction in particular, as information obtained from a few parameter solves might extend to other parameter settings as well. When this is the case and how this can be used will be the topic of this work.

[1] Picture thanks to James Nagel from the University of Utah in Salt Lake City, Utah.

Of further interest are uncertain parameters, which is the right setting for many practical applications and this work discusses the model reduction of wave propagation simulation in dispersive media with uncertain parameters in particular.

1.2 Parametric Model Order Reduction

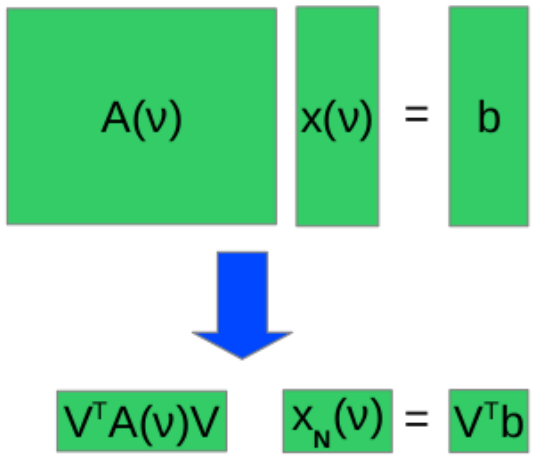

Figure 1.2: Model reduction of the large-scale equation $Ax = b$ with dependence on parameter ν using a projection matrix V.

Parametric model order reduction (PMOR) techniques achieve computational improvements in solving parametrized partial differential equations (PDEs) to enable real-time and many-query applications. An embedded system for instance, which is required to give real-time responses, can only compute with a small scale model. A PMOR technique can be used to generate an appropriate small scale model to be used in the embedded system. In design optimization, a parameter configuration is sought, which gives optimal results. Finding this configuration requires many solves of the underlying model. So that computation time does not become prohibitive, a PMOR technique is useful.

The PMOR by a projection matrix V is depicted in Fig. 1.2. Assume that the underlying PDE has been discretized into a matrix A and input vector b of large dimension $\mathcal{N} > 10.000$ and depends on a parameter ν. The field solution is the, also parameter dependent, state vector $x = x(\nu)$. Using a rectangular projection matrix V reduces the problem size to typically $N < 100$, so that the resulting system can be solved with little computational effort. However, the matrix V needs to be chosen carefully to ensure a low approximation error $\|x - Vx_N\|$.

1.3 Previous Work

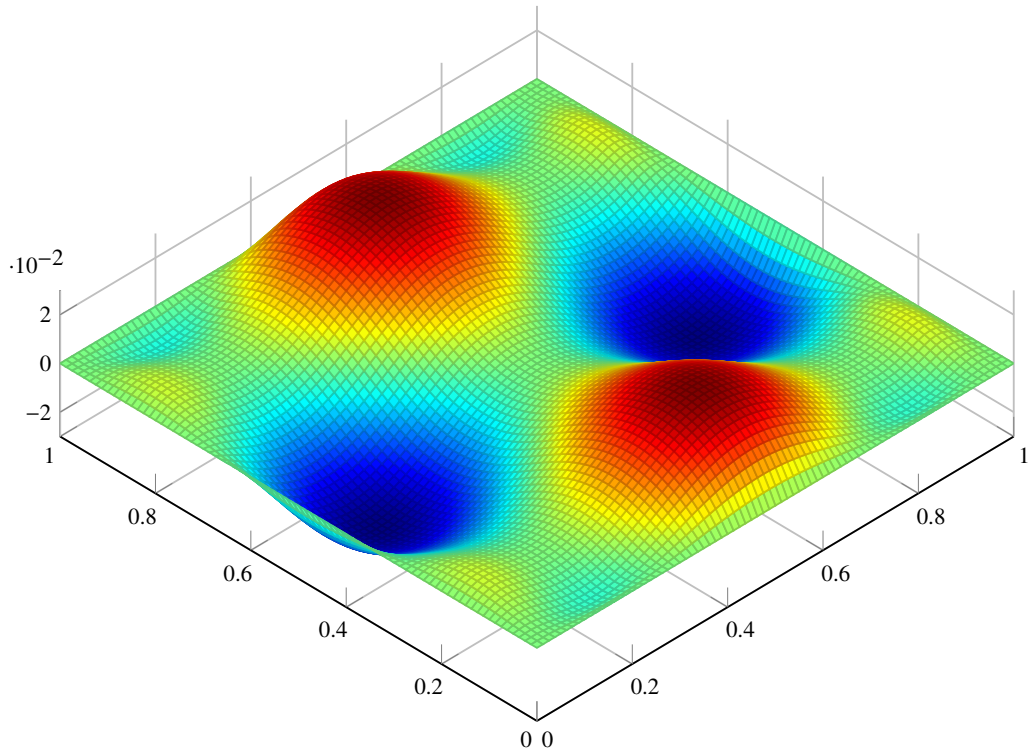

Figure 1.3: Maxwell eigenmode (10th) of a square with zero boundary conditions.

Various model order reduction (MOR) algorithms have been applied in computational electromagnetics (CEM). An early effort was the modal expansion [BM82], then the moment matching model reduction, also called asymptotic waveform evaluation [PR90], [PDEL97], [AD11] and [Bod13], Padé via Lanczos model reduction [ZDP00] and [MWWI00], Krylov subspace acceleration [Fre04], [SDK09] and [NS10], a two-step Lanczos scheme [WMSW02] and Proper Orthogonal Decomposition (POD) and Discrete Empirical Interpolation (DEI) [HC14], to name a few examples. An overview can be found in [Sta12] or in chapter 11 of [YZC06]. Model reduction techniques are also applied in Maxwell eigenvalue problems, see [BW12] for instance.

Besides MOR techniques which work with the state equations, surrogate modeling techniques based on direct interpolation of the output are used. Results on surrogate modeling techniques in computational electromagnetics can be found in [GDFZ99], [LKM03], [CGDD11] and [FKDA13].

Here, the reduced basis method (RBM) is applied, that in recent years has become a widely used approach for reducing parametrized models described by PDEs.

The RBM was first used in the late 1970s in the field of nonlinear structural analysis [ASB78], [Nag79] and [Noo80]. By introducing further concepts such as affine parameter dependence, rigorous error estimation in the state, output error bounds and empirical interpolation, the applicability of the RBM grew considerably.

Output bounds for elliptic PDEs can be found in [MMP01] and [PRV$^+$01] and for noncoercive linear problems in [MPR02]. In [MPT02], a theoretical framework for the uniform exponential convergence of the RBM has been given. A reduced basis element method is introduced in [MR02]. An application of the RBM to a nonlinear problem is found in [VPP03] and the empirical interpolation technique is introduced in [BMNP04]. The extension to parabolic problems can be found in [MA05], an application to Stokes and Navier-Stokes problems in [VP05], [Dep08] and [RHM13]. Natural norm estimators can be found in [SVH$^+$06], and the estimation techniques for stability factors in [HRSP07] and [CHMR08]. They allow a rigorous error estimation by either moving to a parameter-dependent ('natural') norm or using the successive constraint method to compute lower and upper bounds to the stability constant. Finite volume discretizations are used in [BM08], high-dimensional parameter settings (i.e. 25 parameters) in [Sen08] and stochastic parameter settings in [BBM$^+$09]. The hp-RBM can be found in [EPR10] an application to optimal control in [Ded10], and a coupled fluid-structure setting is covered in [LQR12], to give an impression of the scope of the RBM.

The RBM has also been applied to computational electromagnetics in a number of works. A 2D time-harmonic Maxwell problem with a focus on the error estimation can be found in [CHMR09], the extension to error bounds in the output can be found in [CHMR10] and [RLM15]. Electromagnetic scattering is the application in [Pom10], [GHS12] and [CHM$^+$12], a reduced basis element method in [CHM11]. A first introduction of the RBM to microwave devices has been established in [dlRRM09]. The eddy current equations are the focus of [Jun12] while reduced basis MOR of the electric field integral equation can be found in [HSZ12] and [FHMS11].

1.4 Thesis Contribution

The RBM in electromagnetic applications shows the potential to enable real-time and many-query tasks of large-scale models, which would not be possible without model reduction.

The main focus of this work are microwave devices, where three models, a coplanar waveguide, a branchline coupler and a printed circuit board are considered. Building on [dlRRM09] and [CHMR09], this work extends the RBM in electromagnetics to 3-dimensional, multi-parameter models, related to [Pom10] in optical applications. The RBM shows exponential convergence in the maximum approximation error, such that low-order models of high accuracy are generated, even in the case of resonant

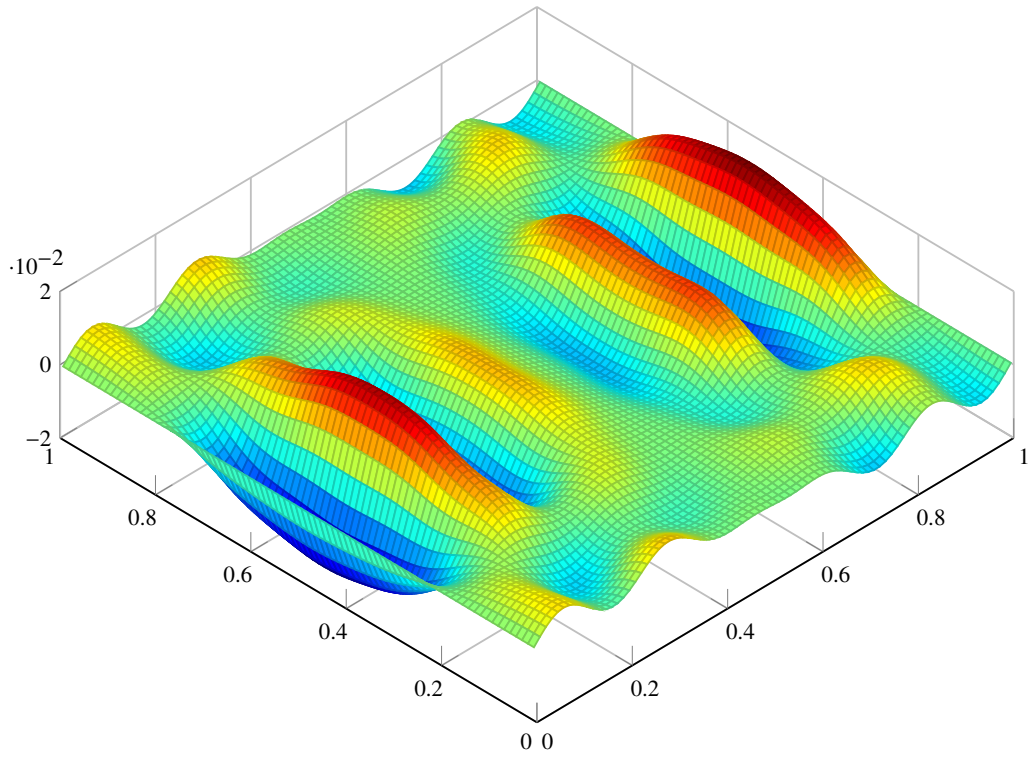

Figure 1.4: POD mode (1st) of the electric field in a square domain.

behavior. The parameter studies cover the RBM using bounds on the error in the state and primal-dual methods giving bounds on the output. The electromagnetic components considered are excited by ports, i.e. parts of the structure where external sources such as voltages and currents are applied. The transfer function is then given as the ratio between output and input signals (cf. [WSW06], [Sta12]). Additionally, a comparison of Lagrange RB and Taylor RB is performed, as well as a comparison of the reduced basis, moment matching and proper orthogonal decomposition model reduction methods.

Furthermore, an accurate lower bound of the inf-sup stability constant is required for rigorous error estimation. Multiple techniques for obtaining rigorous and non-rigorous bounds to the stability constant are shown and compared. As resonant parameter configurations can be captured by the stability constant, this information can potentially be used a priori in the construction of the reduced model. Novel bounds are presented, which take information of multiple eigenvalues at a single parameter configuration into account.

An important task towards more physically accurate parameter settings involve uncertain parameters, since model behavior can often only be quantified with respect

to statistical quantities. The uncertainty quantification by Monte-Carlo and stochastic collocation is performed on the time-harmonic microwave model of a coplanar waveguide and a time-dependent dispersion model.

This is the first application of the RBM to a dispersive electromagnetic model, to the best of my knowledge. The POD-Greedy method is used for the reduction of the time-dependent model and stochastic collocation to quantify statistical quantities. Fig. 1.4 shows the first POD mode of the electric field in one spatial component. Again, exponential convergence can be observed, when having two dispersion parameters in the model. This allows to use a low-order model in the uncertainty quantification.

1.5 The Stability Constant

To have a rigorous error estimation available, the stability constant of the weak form of the associated PDE needs to be determined. Besides error estimation, the stability constant is an important concept for proving existence, uniqueness and well-posedness of solutions to the weak form of the PDE. Electromagnetics features the inf-sup stability constant, which is a generalization of the coercivity constant.

Assume the weak form of the PDE is represented by a complex-valued sesquilinearform $a(\cdot,\cdot) : X \times X \to \mathbb{C}$, over a Hilbert space X. The sesquilinearform is coercive, if it is real-valued and there exists an $\alpha > 0$, so that

$$a(u,u) \geq \alpha \|u\|_X^2, \quad \forall u \in X. \tag{1.1}$$

The largest possible choice for α is called the coercivity constant, defined as

$$\alpha = \inf_{u \in X} \frac{a(u,u)}{\|u\|_X^2}. \tag{1.2}$$

Let A denote the system matrix, which assembles $a(\cdot,\cdot)$ for a discretisation method of choice, and M the corresponding mass matrix or inner product matrix. In the finite dimensional setting, the definition (1.2) is also valid, except that the infimum is actually attained by a minimizer. Using that $a(u,u) = x^T Ax$ and $\|u\|_X^2 = x^T Mx$ with x the coordinate representation in the discrete basis of the function u, a generalized eigenvalue problem is formulated for the computation of α, namely for

$$Av = \lambda Mv, \tag{1.3}$$

the minimum eigenvalue λ_{min} is the discrete coercivity constant. The condition (1.1) thus translates as having a positive definite system matrix.

The time-harmonic Maxwell's equations do not satisfy (1.1), but the inf-sup condition does grant solvability. It holds

$$0 < \beta = \inf_{u \in X} \sup_{v \in X} \frac{|a(u,v)|}{\|u\|_X \|v\|_X}. \tag{1.4}$$

Here, β is called the inf-sup stability constant and (1.4) is called the inf-sup condition or Babuška-Brezzi condition or LBB condition. The corresponding eigenvalue problem (1.3) gives the discrete inf-sup constant as the eigenvalue of minimum magnitude. The condition (1.4) thus translates as having a nonsingular system matrix and can thus be seen as a generalization of coercivity.

1.6 Thesis Outline

Chapter 2 introduces the topic of computational electromagnetics with a particular focus on the finite element method, while chapter 3 introduces the certified reduced basis method. In chapter 4, parameter studies are performed with three microwave models, a coplanar waveguide, a branchline coupler and a printed circuit board. For rigorous error estimation, the estimation of the inf-sup stability constant plays a particular role, which is unfolded in chapter 5. Using reduced order models to quantify model behavior under uncertain parameters is discussed in chapter 6. Numerical studies of the time-dependent, dispersive case can be found in chapter 7, and chapter 8 concludes and summarizes the findings.

2 Computational Electromagnetics

2.1 Maxwell's Equations

James Clerk Maxwell[1] first formulated Maxwell's equations in his paper "A Dynamical Theory of the Electromagnetic Field" in 1865. He describes electric and magnetic phenomena and their interaction, which are now known as classical electromagnetism. The outline given in this section can be found with more detail in [Mon03], [Zag06] and [Jin14].

The time- and space-dependent vector fields involved in Maxwell's equations are

- the electric field intensity E, measured in $\left[\frac{V}{m}\right]$,
- the magnetic field intensity H, measured in $\left[\frac{A}{m}\right]$,
- the electric flux D, measured in $\left[\frac{As}{m^2}\right]$,
- and the magnetic flux B, measured in $\left[\frac{Vs}{m^2}\right]$,

further quantities of importance are

- the charge density ρ, measured in $\left[\frac{As}{m^3}\right]$,
- and the current density j, measured in $\left[\frac{A}{m^2}\right]$,

with the **SI** units meter (m), second (s), Ampère (A) and Volt (V).

2.1.1 Integral Form of Maxwell's Equations

The integral form of the macroscopic Maxwell's equations is stated for arbitrarily chosen volume V with boundary ∂V (with outer normal vector n) and surface S (with normal vector n) with boundary ∂S (with tangential vector τ). It consists of the four equations:

Faraday's induction law:

$$\int_S \frac{\partial B}{\partial t} \cdot n dS + \int_{\partial S} E \cdot \tau ds = 0, \tag{2.1}$$

[1] 13th June 1831 - 5th November 1879

Ampère's law with displacement current density:

$$\int_{\partial S} H \cdot \tau ds = \int_S \frac{\partial D}{\partial t} \cdot n dS + \int_S j \cdot n dS, \tag{2.2}$$

Gauß' law:

$$\int_{\partial V} D \cdot n dS = \int_V \rho dx, \tag{2.3}$$

Gauß' law for magnetism:

$$\int_{\partial V} B \cdot n dS = 0. \tag{2.4}$$

2.1.2 Differential Form of Maxwell's Equations

Using Stokes' and Gauß' theorems, the integral form rewrites in the classical, differential form as

$$\begin{aligned} \frac{\partial B}{\partial t} + \nabla \times E &= 0, & (2.5)\\ \nabla \cdot B &= 0, & (2.6)\\ \frac{\partial D}{\partial t} - \nabla \times H &= -j, & (2.7)\\ \nabla \cdot D &= \rho. & (2.8) \end{aligned}$$

The equation (2.5) is the Faraday equation and equation (2.7) is the Ampère equation. The equations (2.5) - (2.8) will be rewritten in second order form, suitable for numerical computations, as can be seen in subsection 2.1.6.

2.1.3 Charge Conservation

The continuity equation or conservation of charge is derived by taking the divergence of equation (2.7) and using equation (2.8) to obtain

$$\nabla \cdot j + \frac{\partial \rho}{\partial t} = 0. \tag{2.9}$$

Either the equations (2.5), (2.7) and (2.8) can be taken as independent equations, or the set of equations (2.5), (2.7) and (2.9) can be taken as independent. The respective remaining equations can then be derived, cf. [Jin14].

2.1.4 Constitutive Material Relations

The field strengths are related to the fluxes by the relations

$$D = \epsilon E, \tag{2.10}$$
$$B = \mu H, \tag{2.11}$$

with the material parameters permeability ϵ and permittivity μ. The permittivity of a medium describes how much electric flux is 'generated' per unit charge in that medium. Permeability is the measure of the ability of a material to support the formation of a magnetic field within itself. In free space these constants are given by

$$\epsilon_0 = 8.854187817 \times 10^{-12} \frac{As}{Vm}, \tag{2.12}$$
$$\mu_0 = 4\pi \times 10^{-7} \frac{Vs}{Am}. \tag{2.13}$$

In a linear medium it holds $\epsilon = \epsilon_r \epsilon_0$ with relative permittivity $\epsilon_r \geq 1$ and $\mu = \mu_r \mu_0$ with relative permeability $\mu_r \geq 1$. The propagation velocity of the electromagnetic wave in a non-dispersive medium is given by $v = \frac{1}{\sqrt{\epsilon\mu}}$, which in vacuum is the speed of light $c = \frac{1}{\sqrt{\epsilon_0 \mu_0}}$.

The total source current density j is composed of impressed current density j_i and conduction current density j_c as

$$j = j_c + j_i, \tag{2.14}$$
$$j_c = \sigma E, \tag{2.15}$$

with conductivity σ as a material parameter.

2.1.5 Boundary Conditions

Boundary conditions in electromagnetics are related to the type of material that is assumed on the boundary. A perfectly electric conducting (PEC) boundary assumes a $\sigma \to \infty$ relationship inside the bounding material and all fields are assumed to be zero inside a PEC material. It is used to model metallic boundaries. A perfectly magnetic conducting (PMC) boundary models a material with very high permeability. It is only introduced as a mathematical concept for vanishing tangential magnetic fields at the bounding surface.

Perfectly Electric Conducting Boundary

The PEC boundary is characterized by a vanishing tangential electric field E at the boundary, i.e.

$$n \times E = 0, \tag{2.16}$$

and is also referred to as an essential or Dirichlet boundary.

Perfectly Magnetic Conducting Boundary

The PMC boundary is characterized by

$$n \times \nabla \times E = 0, \tag{2.17}$$

and is also referred to as a free or Neumann boundary.

2.1.6 Time-Dependent Maxwell's Equations

There is a variety of formulations of Maxwell's equations (2.5) - (2.8) suitable for discretization and numerical computations. Following [Mon03], the derivation of the second order formulation in the electric field E is shown, which is used subsequently. See the literature [Zag06], [Bod13], [RIB13] and [Jin14] for alternative formulations as saddle point problem in the electric and magnetic field or potential formulations.

From the differential form of Maxwell's Equations (2.5), (2.7) and the material relations, it follows

$$\frac{\partial H}{\partial t} = -\frac{1}{\mu}\nabla \times E, \tag{2.18}$$

$$\epsilon\frac{\partial^2 E}{\partial t^2} - \nabla \times \frac{\partial H}{\partial t} = -\frac{\partial j}{\partial t}, \tag{2.19}$$

such that H can be eliminated, leading to

$$\epsilon\frac{\partial^2 E}{\partial t^2} + \nabla \times \frac{1}{\mu}\nabla \times E = -\frac{\partial j}{\partial t}. \tag{2.20}$$

Using (2.14) and (2.15), the second-order, time-dependent Maxwell equation in the electric field E is derived

$$\epsilon\frac{\partial^2 E}{\partial t^2} + \sigma\frac{\partial E}{\partial t} + \nabla \times \frac{1}{\mu}\nabla \times E = -\frac{\partial j_i}{\partial t}, \tag{2.21}$$

with material parameters

- the electric permittivity ϵ, measured in $[\frac{As}{Vm}]$,
- the magnetic permeability μ, measured in $[\frac{Vs}{Am}]$,
- the conductivity σ, measured in $[\frac{A}{Vm}]$.

Taking the divergence of (2.20) shows that if the initial solution satisfies the continuity equation (2.9), then so will the time-dependent solution. In particular, this ensures that (2.8) is satisfied.

Two approximations are in use, the high-frequency approximation, which assumes $\sigma\frac{\partial E}{\partial t} = 0$

$$\epsilon\frac{\partial^2 E}{\partial t^2} + \nabla \times \frac{1}{\mu}\nabla \times E = -\frac{\partial j_i}{\partial t}, \tag{2.22}$$

and the low-frequency approximation, which assumes $\epsilon\frac{\partial^2 E}{\partial t^2} = 0$

$$\sigma\frac{\partial E}{\partial t} + \nabla \times \frac{1}{\mu}\nabla \times E = -\frac{\partial j_i}{\partial t}. \tag{2.23}$$

For the purpose of this work in microwave applications, mostly the full system (2.21) is relevant, but in some models, the high-frequency approximation (2.22) is used.

2.1.7 Time-Harmonic Maxwell's Equations

In a time-harmonic analysis, assume the electromagnetic fields to be of the form

$$u(x,t) = \mathbf{Re}\{\widehat{u}(x)e^{\imath\omega t}\}, \tag{2.24}$$

where **Re** denotes the real part of the complex quantity $\widehat{u}(x)e^{\imath\omega t}$ and ω denotes the angular frequency. With the Laplace transformation, the time derivative turns into a multiplication with $\imath\omega$ and the unknown field $\widehat{u}(x)$ is now complex-valued. Note that $\imath = \sqrt{-1}$. To simplify notation, the time-harmonic equations will be set using E instead of $\widehat{E}$. See [Har04] for more details on the derivation.

The equation (2.21) thus transforms into

$$-\epsilon\omega^2 E + \imath\omega\sigma E + \nabla \times \frac{1}{\mu}\nabla \times E = -\imath\omega j_i. \tag{2.25}$$

As in the time-dependent case, two approximations to (2.25) are in use, the high-frequency approximation

$$-\epsilon\omega^2 E + \nabla \times \frac{1}{\mu}\nabla \times E = -\imath\omega j_i, \tag{2.26}$$

and the low frequency approximation

$$\imath\omega\sigma E + \nabla \times \frac{1}{\mu}\nabla \times E = -\imath\omega j_i. \tag{2.27}$$

2.2 Functional Analysis

The functional analytic background for computational electromagnetics is briefly stated. For more detailed information and related proofs, see [Hip02], [Mon03], [Jin11] or [RIB13] amongst many others.

Definition 2.2.1 (Hilbert Spaces)**.** A Hilbert space H is an inner product space over $\mathbb{R}$ or $\mathbb{C}$ that is complete w.r.t. the norm induced by the inner product.

Definition 2.2.2 (Lebesque Spaces)**.** A Lebesque space $L^p(\Omega)$ for $p \geq 1$ over a domain Ω is the set of functions u which satisfy

$$\|u\|_{L^p}^p = \int_\Omega |u|^p dx < \infty \quad \text{for } p < \infty, \tag{2.28}$$

$$\|u\|_{L^\infty} = \text{ess sup}\,|u| < \infty \quad \text{for } p = \infty. \tag{2.29}$$

The space $L^2(\Omega)$ is a Hilbert space with inner product

$$(u, v)_{L^2} = \int_\Omega u\bar{v}dx, \tag{2.30}$$

Definition 2.2.3 (Sobolev Spaces)**.** The Sobolev spaces $\mathcal{H}^s(\Omega)$ are Hilbert spaces. The space $\mathcal{H}^s(\Omega)$ consists of functions in L^2 with weak derivatives up to order s which are also in L^2. The inner product is defined as

$$(u, v)_{\mathcal{H}^s} = \sum_{i=0}^{s} (D^i u, D^i v)_{L^2}, \tag{2.31}$$

where D^i denotes the weak differential of i-th order.

Definition 2.2.4 (H(curl; Ω) Spaces)**.** The space H(curl; Ω) is the natural space for the electric field as a solution to Maxwell's equations in the domain Ω. It is a vector valued Sobolev space and also a Hilbert space, defined as

$$\mathrm{H}(\mathrm{curl};\,\Omega) \;:= \{u \in \left[L^2(\Omega)\right]^3 \,|\nabla \times u \in \left[L^2(\Omega)\right]^3\}, \tag{2.32}$$

and equipped with the inner product

$$(u,v)_{\mathrm{H}(\mathrm{curl};\,\Omega)} \;:= (u,v)_{L^2} + \int_\Omega \nabla \times u \cdot \overline{\nabla \times v} dx. \tag{2.33}$$

Consider the variational problem

$$a(u,v) = f(v) \quad \forall v \in X, \tag{2.34}$$

posed over a Hilbert space X with bounded and coercive sesquilinear form $a(\cdot,\cdot)$ and $f \in X'$. Given a Hilbert space X over $\mathbb{R}$, define the dual space X' as the space of continuous linear functionals $\phi : X \to \mathbb{R}$.

In particular, consider the mapping $\Phi : X \to X' : x \mapsto \phi_x(\cdot) := (\cdot, x)$. According to the Riesz representation theorem, the spaces X and X' are isometrically isomorph, i.e. for each $\phi \in X'$ there exists a unique $v \in X$ such that $\phi(\cdot) = (v,\cdot)_X$ and $\|\phi\|_{X'} = \|v\|_X$.

Definition 2.2.5 (Dual Norm)**.** The dual norm is defined as

$$\|\phi\|_{X'} = \sup_{v \in X} \frac{|\phi(v)|}{\|v\|_X}. \tag{2.35}$$

If X is a Hilbert space over $\mathbb{C}$, then X and X' are isometrically anti-isomorphic.

Theorem 2.2.6 (Lax-Milgram Theorem)**.** *Suppose $a : X \times X \mapsto \mathbb{C}$ is a bounded and coercive sesquilinear form, where X is a Hilbert space. Then for each $f \in X'$ there exists a unique solution $u \in X$ to (2.34) and it holds*

$$\|u\|_X \leq \frac{C}{\alpha} \|f\|_{X'}, \tag{2.36}$$

with C the boundedness and α the coercivity constant of $a(\cdot,\cdot)$.

In computational electromagnetics the resulting sesquilinear forms are often not coercive but only satisfy the less strict Babuška-Brezzi or inf-sup condition, i.e., there is a constant β such that

$$\inf_{u \in X} \sup_{v \in X} \frac{|a(u,v)|}{\|u\|_X \|v\|_X} := \beta > 0. \tag{2.37}$$

When the test function space differs from the trial function space, s.t. $u \in X$ and $v \in Y$ with X and Y Hilbert spaces, consider $a : X \times Y \mapsto \mathbb{C}$ to be a bounded and inf-sup stable sesquilinear form, i.e.,

$$\inf_{u \in X} \sup_{v \in Y} \frac{|a(u,v)|}{\|u\|_X \|v\|_Y} := \beta > 0. \tag{2.38}$$

see [Mon03] for instance.

Theorem 2.2.7 (Generalized Lax-Milgram theorem)**.** *Assume $a : X \times Y \mapsto \mathbb{C}$ to be a bounded and inf-sup stable sesquilinear form, then for each $f \in Y'$ there exists a unique solution $u \in X$ such that*

$$a(u,v) = f(v) \quad \forall v \in Y, \tag{2.39}$$

and it holds

$$\|u\|_X \leq \frac{C}{\beta} \|f\|_{Y'}. \tag{2.40}$$

2.3 Finite Element Method

There exist various discretisation methods for the Maxwell's equations to enable numerical computation. Frequently used discretisation methods, which work with the differential form of Maxwell's equations, are finite elements [Hip02], [Zag06], finite differences [RIB13], discontinuous Galerkin [HW08] or finite integration techniques [Wei77]. The method of moments (also boundary element method or fast multipole method [Har93]) uses the integral form of Maxwell's equations as starting point. Here, the finite element method is employed and briefly reviewed in the following.

Typically, an abstract notation for the variational form is chosen, where $u^e \in X^e$ is sought, such that

$$a^e(u^e, v^e) = f^e(v^e) \quad \forall v^e \in X^e. \tag{2.41}$$

The superscript ^{e} denotes the infinite dimensional, "exact" problem. As the electric field as solution u^e with PEC boundary conditions on Γ_{PEC} is sought, the correct space is

$$X^e = \{E \in \mathrm{H}(\mathrm{curl};\, \Omega) \;|E \times n = 0 \text{ on } \Gamma_{\mathrm{PEC}}\}, \tag{2.42}$$

in the computational domain Ω, with bilinear or sesquilinear form $a^e(\cdot,\cdot)$ and anti-linear form $f^e(\cdot)$.

Using a conforming discretization space $X \subset X^e$, the infinite dimensional problem is reformulated over the finite dimensional space X, as find $u \in X$, such that

$$a(u,v) = f(v) \quad \forall v \in X. \tag{2.43}$$

The superscript ^{e} has been dropped, since this formulation is using only discretized, finite dimensional quantities. In the Reduced Basis Method, this formulation is referred to as the "truth" formulation, since approximation errors will be measured with respect to (2.43) and the error between the solutions to (2.43) and (2.41) is assumed to be negligible, see [RHP08].

Taking the time-harmonic Maxwell's equation (2.25) as an equation in X, multiplying with the complex conjugate of a test function $v \in X$ and integrating over the computational domain Ω, leads to

$$\begin{aligned} -\epsilon\omega^2(E,v)_{L^2(\Omega)} + \imath\omega\sigma(E,v)_{L^2(\Omega)} + \frac{1}{\mu}(\nabla\times E, \nabla\times v)_{L^2(\Omega)} = \\ -\imath\omega(j_i,v)_{L^2(\Omega)}, \end{aligned} \tag{2.44}$$

where

$$\int_\Omega \frac{1}{\mu}\left(\nabla\times\nabla\times E\right)\cdot\overline{v}d\Omega = \int_\Omega \left(\frac{1}{\mu}\nabla\times E\right)\cdot\left(\nabla\times\overline{v}\right)d\Omega + \int_{\partial\Omega}\frac{1}{\mu}\left(n\times\nabla\times E\right)\cdot\overline{v}dA$$

was used and the term $\int_{\partial\Omega}\frac{1}{\mu}\left(n\times\nabla\times E\right)\cdot\overline{v}dA$ vanishes due to the assumption of PEC and PMC boundary conditions. In particular, PEC boundary conditions are enforced by setting the appropriate degrees of freedom to zero and are already explicit in the space $X \subset X^e$. PMC boundary conditions are treated as natural boundaries and are therefore implicit in the weak formulation (2.44) of the problem. Although there are also other variational formulations of Maxwell's equations, (2.44) is commonly used as the outset for finite element treatment, see [Mon03].

The sesquilinear form and linear form are then defined as

$$a_{\mathbb{C}}(E,v) = -\epsilon\omega^2(E,v)_{L^2(\Omega)} + \imath\omega\sigma(E,v)_{L^2(\Omega)} + \frac{1}{\mu}(\nabla\times E,\nabla\times v)_{L^2(\Omega)}, \tag{2.45}$$

$$f_{\mathbb{C}}(v) = -\imath\omega(j_i,v)_{L^2(\Omega)}, \tag{2.46}$$

where the subscript $_{\mathbb{C}}$ denotes that these are complex forms. Note that the sesquilinear form $a_{\mathbb{C}}(\cdot,\cdot)$ is not hermitian.

The discretization enables solving (2.44) by solving a sparse linear system

$$Ax = b, \tag{2.47}$$

for the state vector $x \in \mathbb{C}^{\mathcal{N}}$ of large dimension $\mathcal{N}$, which represents the discrete electric field solution E. Given a basis $\{\varphi_i | i = 1,\ldots,\mathcal{N}\}$ of X, the matrix and vector entries are assembled as

$$\begin{aligned} A_{kl} &= a_{\mathbb{C}}(\varphi_k, \varphi_l), \\ b_k &= f_{\mathbb{C}}(\varphi_k). \end{aligned} \tag{2.48}$$

2.3.1 Nédélec Finite Elements

This subsection introduces the Nédélec finite element [Ned80], which allows a H(curl; Ω) conforming discretisation, see also [Zag06], [Mon03] and [Sch03] for proofs and further details.

The construction of the finite element space X is required to satisfy the following prerequisites:

- The computational domain is covered by a triangulation, i.e., a union of nonoverlapping elements K. For instance, triangles (2D) or tetrahedra (3D) are used.
- The basis functions $\varphi_i, i = 1 \ldots \mathcal{N}$ are piecewise polynomial.
- The basis functions have local support, i.e., a support which extends over only a few elements.

Consider the Nédélec element of first kind of order 1. This lowest order edge element defines the local space $N_0(K)$ on a triangle or tetrahedron K as

$$\begin{cases} N_0(K) = \{a + b \begin{bmatrix} y \\ -x \end{bmatrix} | a \in \mathbb{R}^2, b \in \mathbb{R}\} & \text{for } d = 2 \text{ and with } \dim(N_0(K)) = 3, \\ N_0(K) = \{a + b \times \begin{bmatrix} x \\ y \\ z \end{bmatrix} | a, b \in \mathbb{R}^3\} & \text{for } d = 3 \text{ and with } \dim(N_0(K)) = 6, \end{cases} \tag{2.49}$$

and the edge based degrees of freedom

$$N_\alpha^{N_0} : v \mapsto \int_{E_\alpha} v \cdot \tau dx \tag{2.50}$$

defined for all edges E_α, where the α index enumerates over all edges.

In 3 dimensions, the local space $N_0(K)$ lies between the polynomial spaces $\left(P^0(K)\right)^3$ and $\left(P^1(K)\right)^3$.

The nodal basis is formed with the edge-based shape functions (this is the 1-form Whitney element), as

$$\varphi_\alpha = \nabla\lambda_{\alpha_1}\lambda_{\alpha_2} - \lambda_{\alpha_1}\nabla\lambda_{\alpha_2}, \tag{2.51}$$

for each edge $E_\alpha = [V_{\alpha_1}, V_{\alpha_2}]$. The barycentric coordinate λ_{α_1} corresponding to the vertex V_{α_1} is the unique linear polynomial which satisfies $\lambda_{\alpha_1}(V_{\alpha_2}) = \delta_{\alpha_1\alpha_2}$. The shape functions have constant tangential trace on the edges of K,

$$\varphi_\alpha \cdot \tau_{E_\beta} = \frac{1}{|E_\beta|}\delta_{\alpha\beta}, \tag{2.52}$$

for edges E_α, E_β and it holds

$$N_\beta(\phi_\alpha) = \int_{E_\beta} \varphi_\alpha \cdot \tau dx = \delta_{\alpha\beta}. \tag{2.53}$$

Given a continuously differentiable, invertible and surjective mapping from the reference element to an actual element $\Phi_K : \widehat{K} \to K$ and $\widehat{u} \in H(\mathrm{curl}, \widehat{K})$, the H(curl)-conforming transformation, also called Piola transformation [Sch03], is given by

$$u = F_K^{-T}\widehat{u} \circ \Phi_K^{-1}, \tag{2.54}$$

which implies $u \in H(\mathrm{curl}, K)$, with

- in 2D: $\nabla \times u = J_K^{-1}\widehat{\nabla} \times \widehat{u} \circ \Phi_K^{-1}$, (2.55)
- in 3D: $\nabla \times u = J_K^{-1}F_K\widehat{\nabla} \times \widehat{u} \circ \Phi_K^{-1}$. (2.56)

The Jacobian F_K and its determinant J_K are defined by

$$F_K(\widehat{x}) = \left(\frac{\partial\Phi_{K,i}}{\partial\widehat{x}_j}(\widehat{x}_j)\right)_{1\le i,j\le d}, \tag{2.57}$$

$$J_K(\widehat{x}) = \det\left(F_K(\widehat{x})\right). \tag{2.58}$$

Given a shape function $\widehat{\varphi}_\alpha$ on the reference element $\widehat{K}$, the shape function φ_α on the actual element K is derived as

$$\varphi_\alpha(x) = F_K^{-T}(\widehat{x})\widehat{\varphi}_\alpha(\widehat{x}), \tag{2.59}$$

using the mapping $x = \Phi(\widehat{x})$.

The finite element space X is then obtained by identifying the degrees of freedom with the edges of the mesh E_α, i.e,

$$X = \bigoplus_{E_\alpha} \mathrm{span}\{\varphi_\alpha\}. \tag{2.60}$$

Due to the identification of the edges with the degrees of freedom, the Nédélec elements are also termed edge elements. Characteristic of the H(curl; Ω)-conforming elements is the tangential continuity across element interfaces. Summarizing, it holds that

$$X = \{v \in \mathrm{H}(\mathrm{curl};\, \Omega) \mid v_K \in N_0(K) \quad \forall K\}, \tag{2.61}$$

for the elements K in the triangulation.

2.3.2 Finite Element Assembly

As stated in (2.48), the entries of the system matrix are computed as $A_{kl} = a_{\mathbb{C}}(\varphi_k, \varphi_l)$. A computationally efficient assembly computes element matrices A_{kl}^K for all elements K. This is done by integration on the reference element $\widehat{K}$, taking into account the element transformations. The essential parts are in 3 dimensions:

$$(\varphi_k, \varphi_l)_{L^2(K)} = \int_{\widehat{K}} (F_K^{-T}\widehat{\varphi}_k)(F_K^{-T}\widehat{\varphi}_k) J d\widehat{x}, \tag{2.62}$$

$$(\nabla \times \varphi_k, \nabla \times \varphi_l)_{L^2(K)} = \int_{\widehat{K}} J^{-1}(F_K \nabla \times \widehat{\varphi}_k)(F_K \nabla \times \widehat{\varphi}_k) d\widehat{x}, \tag{2.63}$$

$$(j_i, \varphi_l)_{L^2(K)} = \int_{\widehat{K}} j_i (F_K^{-T}\widehat{\varphi}_l) J d\widehat{x}, \tag{2.64}$$

and in 2 dimensions:

$$(\varphi_k, \varphi_l)_{L^2(K)} = \int_{\widehat{K}} (F_K^{-T}\widehat{\varphi}_k)(F_K^{-T}\widehat{\varphi}_k) J d\widehat{x}, \tag{2.65}$$

$$(\nabla \times \varphi_k, \nabla \times \varphi_l)_{L^2(K)} = \int_{\widehat{K}} J^{-1}(\nabla \times \widehat{\varphi}_k)(\nabla \times \widehat{\varphi}_k) d\widehat{x}, \tag{2.66}$$

$$(j_i, \varphi_l)_{L^2(K)} = \int_{\widehat{K}} j_i (F_K^{-T}\widehat{\varphi}_l) J d\widehat{x}. \tag{2.67}$$

This leads to a sparse system matrix A and a source vector b. Solving the equation $Ax = b$ for the state $x = (x_1, ..., x_{\mathcal{N}}) \in \mathbb{C}^{\mathcal{N}}$ gives the coordinate representation of the electric field E in the finite element basis, as

$$E = \sum_{i=1}^{\mathcal{N}} x_i \varphi_i. \tag{2.68}$$

2.3.3 Example

This example shows the procedure for deriving numerical solutions to the Maxwell's equations using a discretization with 1012 degrees of freedom, which will be rewritten to real symmetric form with 2024 degrees of freedom.

Consider the second order time-harmonic formulation of Maxwell's equations for the electric field E

$$\nabla \times \mu^{-1} \nabla \times E + \imath\omega\sigma E - \omega^2 \epsilon E = \imath\omega j_i, \tag{2.69}$$

in $\Omega \subset \mathbb{R}^d$ $(d = 2, 3)$ with source term j_i, permeability μ, conductivity σ, permittivity ϵ and subject to zero electric (PEC) and magnetic (PMC) boundary conditions

$$\begin{aligned} E \times n &= 0 \quad \text{on } \Gamma_{\text{PEC}}, & (2.70)\\ \nabla \times E \times n &= 0 \quad \text{on } \Gamma_{\text{PMC}}, & (2.71) \end{aligned}$$

such that $\partial\Omega = \Gamma_{\text{PEC}} \cup \Gamma_{\text{PMC}}$.

By multiplying (2.69) with a test function v, the variational or weak formulation is established, as

$$\begin{aligned} \left(\mu^{-1} \nabla \times E, \nabla \times v\right) &+ \imath\omega \left(\sigma E, v\right) - \omega^2 \left(\epsilon E, v\right) \\ &= \imath\omega \left(j_i, v\right), \end{aligned} \tag{2.72}$$

where $(\cdot, \cdot)$ denotes the complex L^2 inner product over the computational domain Ω.

To evaluate the transfer behavior over a certain frequency range (i.e. $\nu = \omega$), the matrix A is affinely decomposed into parameter-independent matrices as

$$A = A^\mu + \imath\omega A^\sigma - \omega^2 A^\epsilon, \tag{2.73}$$

where the matrices A^μ, A^σ and A^ϵ are discretizations of the respective parts of the weak form, defined element-wise by

$$\begin{aligned} A^\mu_{ij} &= \left(\mu^{-1} \nabla \times \varphi_i, \nabla \times \varphi_j\right), & (2.74)\\ A^\sigma_{ij} &= (\sigma\varphi_i, \varphi_j) = \sigma M, & (2.75)\\ A^\epsilon_{ij} &= (\epsilon\varphi_i, \varphi_j) = \epsilon M, & (2.76)\\ M_{ij} &= (\nabla \times \varphi_i, \nabla \times \varphi_j) + (\varphi_i, \varphi_j), & (2.77) \end{aligned}$$

with H(curl; Ω) inner product matrix M and right-hand-side vector b, defined as

$$b_i = (j_i, \phi_i). \tag{2.78}$$

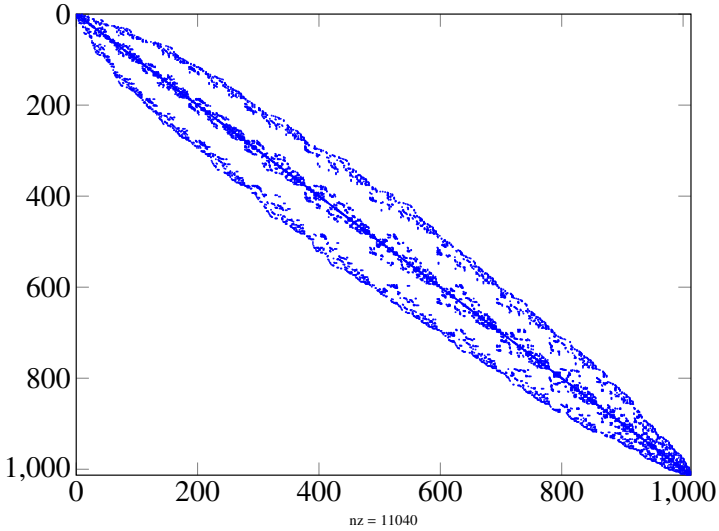

Figure 2.1: Sparsity pattern of the matrix A^σ.

PEC boundary conditions are incorporated by setting the appropriate degrees of freedom to zero and PMC boundary conditions are treated as natural boundaries.

The rows and colums corresponding to zero boundary conditions are eliminated from the assembled matrices. The sparsity pattern for this small example with 1012 degrees of freedom is shown in Fig. 2.1. The sparsity pattern is the same for all matrices. For this example the, eigenvalues of the matrices A^σ and A^ϵ range from $1{\times}10^4$ to $7{\times}10^7$. The matrix A^μ is singular with a largest eigenvalue of $4{\times}10^{10}$. This is established for matrices with typical values for the material parameters already included in the assembly.

Splitting the state vector x into real and complex parts $x = x_{real} + \imath x_{imag}$ and using (2.73), the complex linear system can be rewritten as an equivalent system of twice the dimension over the real numbers

$$\begin{bmatrix} A^\mu - \omega^2 A^\epsilon & -\omega A^\sigma \\ -\omega A^\sigma & -A^\mu + \omega^2 A^\epsilon \end{bmatrix} \begin{bmatrix} x_{real} \\ x_{imag} \end{bmatrix} = \begin{bmatrix} 0 \\ -b \end{bmatrix}. \tag{2.79}$$

This leads to a real and symmetric system matrix, thus its spectrum is real, which is advantageous for the computation of eigenvalues required in the error estimation process.

Let u denote the solution vector of (2.79) and consider the real bilinear form $a(\cdot,\cdot;\nu)$ defined over the $H(\mathrm{curl})$ conforming finite element space X by the system matrix A^ν from (2.79) as

$$a(u, v; \nu) = u^T A^\nu v = u^T \begin{bmatrix} A^\mu - \omega^2 A^\epsilon & -\omega A^\sigma \\ -\omega A^\sigma & -A^\mu + \omega^2 A^\epsilon \end{bmatrix} v.$$

Remark

The example section 2.3.3 shows that the non-hermitian complex form can be recast into a real symmetric problem of twice the dimension. In subsequent examples, this form will be adopted, since the real symmetric system matrix A has a real spectrum, which is advantageous for the computation of eigenvalues required in the error estimation process, see section 3.2.2.

Except at an eigenfrequency ω_i, the system matrix is nonsingular and indefinite. At an eigenfrequency, the system matrix is singular and the field solution does not depend continuously on the parameter ω. While discontinuities are not captured in the reduced basis MOR paradigm, section 4.2 shows numerical results of a 2-parameter example with several resonance configurations. Note that when a p-dimensional parameter space is considered, the resonance configurations form manifolds of dimension $p - 1$ in the parameter space.

2.4 Dispersive Materials

Simulating the propagation of an electromagnetic pulse through certain media like water and fog or systems like a dielectric waveguide are typical problems of electromagnetics. A particular application in medicine is the noninvasive interrogation of the interior of tissues by electromagnetic waves to give data for medical imaging. The Maxwell's equations presented in section 2.1 are altered by taking a relaxation polarization into account, which changes the permittivity ϵ to a time-dependent quantity, depending on the history of the electric field strength. This is termed a dispersive medium for the wave propagation.

Such media are characterized by polar molecules with a permanent dipole moment and will be modeled here as linear, temporally dispersive media. Considering liquid or solid dielectrics with polar molecules, the molecules reply to the applied external field by rotating, i.e., rotating such that the dipole moment is in sync with the external field. This causes friction, which in turn leads to an exponential damping of the electromagnetic pulse [Oug06], [BF08], [BBG09]. As a concrete example, one can think of the water molecule H_2O, where the hydrogen atoms are attached at a certain angle with the oxygen atom. While the molecule as a whole is neutrally charged, there is a permanent dipole moment due to the particular angle, see Fig. 2.2.

The modeling sets out from the high-frequency approximation (2.22)

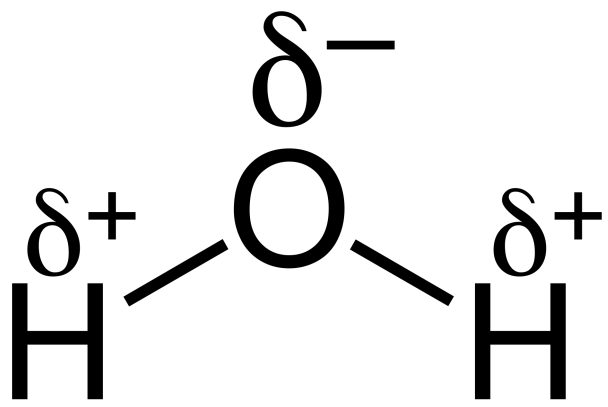

Figure 2.2: Permanant dipole moment in water.

$$\nabla \times \left(\frac{1}{\mu_0 \mu_r} \nabla \times E \right) + \epsilon_0 \epsilon_r \partial_t^2 E = f, \tag{2.80}$$

with a broadband input source f. To achieve the broadband source, the curl of a Gaussian pulse is used in space and the derivative of a Gaussian pulse in time.

The dispersive property is incorporated by replacing $\epsilon_0 \epsilon_r E(t, \mathbf{x})$ with

$$\epsilon_0 \epsilon_\infty E(t, \mathbf{x}) + \epsilon_0 \int_{-\infty}^{t} E(t - \tau, \mathbf{x}) \chi(\tau) d\tau \tag{2.81}$$

with susceptibility χ. Here, a single pole expansion of the susceptibility in frequency domain is assumed with relative permittivity at low-frequency limit ϵ_s, relative permittivity at high-frequency limit ϵ_∞ and relaxation time τ

$$\chi(\omega, \mathbf{x}) = \frac{(\epsilon_s - \epsilon_\infty)}{\imath \omega \tau + 1}.$$

The two terms in (2.81) are the instantaneous polarization $\epsilon_0 \epsilon_\infty E(t, \mathbf{x})$ and the relaxation polarization

$$\epsilon_0 \int_{-\infty}^{t} E(t - \tau, \mathbf{x}) \chi(\tau) d\tau. \tag{2.82}$$

Hence, a non-dispersive medium only exhibits instantaneous polarization, but no relaxation polarization. It is possible to compute with the convolution integral efficiently, see [Jin11], but here the approach is to derive an auxiliary differential equation for the polarization [Jin11], [CG14], which avoids computation of the convolution integral. Define $P(t, \mathbf{x})$ as the relaxation polarization

$$P(t, \mathbf{x}) = \epsilon_0 \int_{-\infty}^{t} E(t - \tau, \mathbf{x}) \chi(\tau, \mathbf{x}) d\tau, \tag{2.83}$$

which writes in frequency domain, where the convolution turns into a multiplication

$$P(\omega, \mathbf{x}) = \epsilon_0 \chi(\omega, \mathbf{x}) E(\omega, \mathbf{x}). \tag{2.84}$$

Using the single-pole expansion for χ, (2.82), it follows

$$(\imath\omega\tau + 1) P(\omega, \mathbf{x}) = \epsilon_0 (\epsilon_s - \epsilon_\infty) E(\omega, \mathbf{x}), \tag{2.85}$$

which leads to

$$\tau \partial_t P + P = \epsilon_0 (\epsilon_s - \epsilon_\infty) E, \tag{2.86}$$

such that the coupled system of E and P, or Maxwell-Debye model for short, is given as

$$\nabla \times \left(\frac{1}{\mu_0} \nabla \times E \right) + \epsilon_0 \epsilon_\infty \partial_t^2 E = f - \partial_t^2 P \tag{2.87}$$

$$\partial_t P + \frac{1}{\tau} P = \frac{\epsilon_0 (\epsilon_s - \epsilon_\infty)}{\tau} E, \tag{2.88}$$

with polarization P and a broadband input source f.

Some typical material parameter values are:

$$\begin{aligned} \text{water:} \quad & \epsilon_\infty = 1.80, \epsilon_s = 81.00, \tau = 9.400 \times 10^{-12} \text{ s}, \\ \text{foam:} \quad & \epsilon_\infty = 1.01, \epsilon_s = 1.16, \tau = 6.497 \times 10^{-10} \text{ s}. \end{aligned}$$

3 Certified Reduced Basis Method

The Reduced Basis Method (RBM) is a parametric model order reduction (PMOR) method. It is termed Certified Reduced Basis Method, when the approximation quality is certified by rigorous error estimators. The RBM has been developed to apply to a wide range of parametrized partial differential equations, see [Roz09] for an introduction and [RHP08] for a comprehensive overview.

In parameter optimization or inverse problems, it is often required to evaluate a large-scale, high-fidelity model, which is parametrized with parameter vector ν in a parameter domain $\mathcal{D}$, for many parameter configurations. This can become computationally infeasible, such that a PMOR method is required. The RBM replaces the large-scale model (also called truth model) with, say, $\mathcal{N} > 10.000$ degrees of freedom by a reduced model with typically $N < 100$ degrees of freedom. Given a reasonable amount of accuracy, the reduced model can then be applied in parameter optimization, for instance.

The aim of the RBM is to determine a low order space X_N of dimension N. Typically, a Lagrange Reduced Basis is employed, which is composed of snapshot solutions $X_N = \text{span}\{u(\nu_1), ..., u(\nu_N)\}$, with $u(\nu)$ the field variable at parameter location ν. The underlying assumption is that the parametric manifold

$$M^\nu = \{u(\nu) | \nu \in \mathcal{D}\}$$

can be well approximated by a subspace spanned by the well-chosen snapshot solutions.

This chapter will provide the main technical ingredients of the RBM and in particular give details of the RBM for Maxwell's equations. In the following sections, for a general introduction to the RBM, the field variable will be denoted as u, but in an example, the field variable E is used to emphasize that the electric field solution to the Maxwell's equations is sought.

3.1 Technical Preliminaries

Given a parametrized PDE in variational form with bilinear or sesquilinear form $a(.,.;\nu)$, defined for all $\nu \in \mathcal{D}$ and continuous linear forms $\ell(.;\nu)$ and $f(.;\nu)$. Consider the truth problem:

$$\begin{cases} \text{For } \nu \in \mathcal{D} \subset \mathbb{R}^P, \text{ evaluate} \\ s(\nu) = \ell(u(\nu); \nu), \\ \text{where } u(\nu) \in X(\Omega) \text{ satisfies} \\ a(u(\nu), v; \nu) = f(v; \nu), \forall v \in X. \end{cases} \tag{3.1}$$

The high-dimensional finite element space is denoted by X. Of particular importance is the transfer function H, which is the mapping of a parameter to the output $H : D \to \mathbb{C} : \nu \mapsto s(\nu)$. When only the transfer function is the desired quantity, methods directly interpolating H such as rational interpolation or Kriging can be employed. In the section on numerical results, a comparison of interpolation methods and reduced basis model reduction will be shown.

Given an RB space $X_N \subset X$, the truth problem is projected onto the reduced space:

$$\begin{cases} \text{For } \nu \in \mathcal{D} \subset \mathbb{R}^P, \text{ evaluate} \\ s(\nu) = \ell(u_N(\nu); \nu), \\ \text{where } u_N(\nu) \in X_N(\Omega) \text{ satisfies} \\ a(u_N(\nu), v_N; \nu) = f(v_N; \nu), \forall v_N \in X_N. \end{cases} \tag{3.2}$$

Since the reduced space is composed of snapshot solutions $X_N = \text{span}\{u(\nu_1), ..., u(\nu_N)\}$ at iteratively chosen parameter configurations $S_N = \{\nu_1, ..., \nu_N\}$, the reduced spaces are hierarchical

$$X_1 \subset X_2 \subset \ldots \subset X_N. \tag{3.3}$$

The RBM shows exponential convergence rates and generates a low order model with usually $N < 100$ [BCD+11]. Given a desired approximation tolerance, the approximation quality of the reduced order model can be certified using rigorous error estimators.

Different parameters including frequency, geometric and material parameters can be simultaneously treated by the RBM and the reduced-order model meets the accuracy requirement for all possible variations of all the parameters in the parameter space D.

3.1.1 Basic Definitions

The Exact Model

The starting point of the RBM is the variational or weak form of a PDE, e.g.

$$a^e(u^e, v^e; \nu) = f^e(v^e; \nu), \quad \forall v^e \in X^e,$$

with field solution u^e, test functions v^e and parameter vector $\nu \in D$. The superscript e denotes the "exact", infinite dimensional formulation.

The High-Fidelity Model

After discretisation and Galerkin projection, the problem is turned into a discrete formulation of typically large dimension $\mathcal{N}$

$$a(u, v; \nu) = f(v; \nu), \quad \forall v \in X. \tag{3.4}$$

The Reduced-Order Model

Using solution snapshots at certain parameter values ν to span a low-dimensional space X_N, one can perform another Galerkin projection onto the space of snapshots as

$$a(u_N, v_N; \nu) = f(v_N; \nu), \quad \forall v_N \in X_N \subset X. \tag{3.5}$$

For a well-chosen reduced basis space X_N, the solution to the low-dimensional problem (3.5) approximates the solution to the large-dimensional problem (3.4) in the sense that the error $\|u - u_N\|_X$ is small, and thus also the error in the output $\|\ell(u(\nu); \nu) - \ell(u_N(\nu); \nu)\|_X = \|\ell(u(\nu) - u_N(\nu); \nu)\|_X$.

In the formulation of Maxwell's equations, the discrete variational form (3.4) is posed over the function space $X = H(\mathrm{curl})$ with appropriate Dirichlet boundary conditions.

The Inf-Sup Stability Constant

The inf-sup stability constant $\beta(\nu)$ is defined as

$$\beta(\nu) = \inf_{u \in X} \sup_{v \in X} \frac{|a(u, v; \nu)|}{\|u\|_X \|v\|_X} \tag{3.6}$$

$$= \inf_{u \in X} \frac{\|a(u, \cdot; \nu)\|_{X'}}{\|u\|_X}. \tag{3.7}$$

The linear system corresponding to (3.4) is uniquely solvable when the discrete inf-sup constant satisfies $\beta(\nu) > 0$, the case of $\beta(\nu) = 0$ corresponds to a resonance configuration.

Further define the supremizing operator $T^\nu : X \to X$ by

$$(T^\nu u, \cdot)_X = a(u, \cdot; \nu), \tag{3.8}$$

such that $T^\nu u$ is the Riesz representer of $a(u, \cdot; \nu)$, which allows to write the stability constant as

$$\beta(\nu) = \inf_{u \in X} \frac{\|T^\nu u\|_X}{\|u\|_X}. \tag{3.9}$$

The stability constant can thus be computed by solving the eigenvalue problem

$$T^\nu u = \lambda_{\min} u \tag{3.10}$$

for the eigenvalue with minimal magnitude $\lambda_{\min}$.

Introduce the discrete inner product for the real symmetric form

$$(u, v)_X = u^T M v \quad \forall u, v \in X \tag{3.11}$$

with elements $M_{ij} = (\varphi_i, \varphi_j)_{L^2}$ and the notation A^ν to denote the matrix representation of $a(\cdot, \cdot; \nu)$. Note that while on the left hand side of (3.11), u and v are functions in X, on the right hand side, the coordinate representation in the finite element basis of u and v is used. Eq. (3.8) writes as

$$(T^\nu u)^T M v = u^T A^\nu v, \quad \forall u, v \in X, \tag{3.12}$$

which can only be fulfilled for $T^\nu = M^{-1} A^\nu$. Generally, the matrix representing the operator T^ν is dense, so that the equivalent generalized eigenvalue problem

$$A^\nu u = \lambda_{\min} M u, \tag{3.13}$$

is solved instead, to obtain $\beta(\nu)$.

Lower bound estimates $\beta_{LB}(\nu) \leq \beta(\nu)$ are usually constructed with a Successive Constraint Method (SCM) ([HRSP07]) and will be looked upon in more detail in chapter 5.

3.1.2 Affine Decomposition

The RBM requires to have a fast assembly of the reduced linear system as well as fast evaluations of the error estimator in the sense that the complexity is independent of the large discretisation size of the full model. This is also termed Offline-Online decomposition, since an expensive offline phase computes the $\mathcal{N}$-dependent parts, while the online phase evaluates the reduced solution and error estimates independent of $\mathcal{N}$.

The necessary requirement is an affine decomposition of the bilinear and linear forms as

$$a(u(\nu), v; \nu) = \sum_{q=1}^{Q_a} \Theta_a^q(\nu) a^q(u(\nu), v), \tag{3.14}$$

$$f(v; \nu) = \sum_{q=1}^{Q_f} \Theta_f^q(\nu) f^q(v), \tag{3.15}$$

where $\Theta_a^q(\nu)$ and $\Theta_f^q(\nu)$ are scalar coefficient functions of the parameter and $a^q(u(\nu), v)$ and $f^q(v)$ are parameter-independent bilinear and linear forms.

In the case of only having the frequency ω as parameter, the affine form is readily established, by expanding (2.73) in the frequency. Material parameters also readily allow an affine expansion, as the weak form (2.45) already is affine in μ, σ and ϵ. An affine decomposition (3.14) enables fast (i.e. $\mathcal{N}$-independent) evaluations of the input-output behavior of the reduced model as well as the error estimator. In case of a nonaffine parameter dependence, an affine form can be approximated by using the empirical interpolation method (EIM, [GMNP07]) or one of the methods building on the EIM (e.g., [PBWB14] or [CQR14b]). This however shall not be a concern in this work, since all parameter dependencies considered here are affine in the analytical sense.

The reduced basis is orthonormalized by a modified Gram-Schmidt process giving orthonormal basis functions ζ_i, such that the reduced order solution is represented as

$$u_N(\nu) = \sum_{n=1}^{N} \alpha_n(\nu) \zeta_n, \tag{3.16}$$

for some coefficients α_n.

Assuming a reduced basis has been computed as $X_N = \{\zeta_1, \ldots, \zeta_N\}$, solving system (3.5) amounts to solving the linear system

$$\sum_{n=1}^{N} a(\zeta_n, \zeta_m; \nu) \alpha_n(\nu) = f(\zeta_m), \quad 1 \leq m \leq N \tag{3.17}$$

Using (3.14), the coefficient matrix in (3.17) can be expressed as

$$\sum_{n=1}^{N} \left(\sum_{q=1}^{Q_a} \Theta^q(\nu) a^q(\zeta_n, \zeta_m) \right). \tag{3.18}$$

As the terms $a^q(\zeta_n, \zeta_m)$ are parameter-independent, they can be precomputed during the offline phase and only small $N \times N$ matrices need to be stored. During the online phase, the reduced system matrix is formed according to (3.18) for each parameter configuration and only an $N \times N$ linear system needs to be solved.

Denote the reduced parameter-dependent system matrix by $A_N^\nu = \sum_{q=1}^{Q_a} \Theta^q(\nu) A_N^q$ and the reduced right hand side by b_N^ν and write (3.17) as

$$A_N^\nu u_N(\nu) = b_N^\nu. \tag{3.19}$$

The terms $a^q(\zeta_n, \zeta_m)$ correspond to the matrices A_N^q, and are parameter-independent, so they can be precomputed during the offline-phase. The online phase only assembles the reduced order system matrix according to (3.18).

3.2 Parameter Domain Sampling

3.2.1 Greedy selection

In the RBM, the reduced basis space X_N onto which the system is projected is composed of "snapshot" solutions, i.e. field solution vectors $u(\nu_i)$ at particular parameter locations $S_N = \{\nu_1, ..., \nu_N\}$. To get good approximation properties, while keeping the size N of the reduced space low, it is essential to choose the snapshot locations S_N carefully.

Algorithm 1: Greedy Sampling Strategy

INPUT: sample set Ξ, tolerance ϵ
OUTPUT: reduced basis sample set S_N, projection space X_N

Choose $\nu_1 \in \Xi$ arbitrarily
Solve (3.4) for $u(\nu_1)$
Set $S_1 = \{\nu_1\}$
Set $X_1 = [u(\nu_1)]$
Set $N = 1$
while $\max_{\nu \in \Xi} \Delta_N(\nu) \geq \epsilon$ **do**
    Set $\nu_{N+1} = \arg\max_{\nu \in \Xi} \Delta_N(\nu)$
    Solve (3.4) for $u(\nu_{N+1})$
    Set $S_{N+1} = S_N \cup \nu_{N+1}$
    Set $X_{N+1} = [X_N \quad u(\nu_{N+1})]$
    Orthonormalize X_{N+1}
    Set $N = N + 1$
end while

This can be achieved in an offline greedy process [RHP08], which iteratively chooses snapshot locations based on evaluating an error estimator $\Delta_N(\nu)$ and choosing in each

iteration only the snapshot, which is currently least well approximated. Let Ξ denote a sufficiently fine, discrete sample of the parameter domain D and ϵ be a prespecified approximation tolerance, the sampling is shown in pseudocode in algorithm 1.

The greedy sampling terminates once the approximation tolerance ϵ is certified by the error estimator. This results in the reduced basis space X_N, which allows the fast online evaluations. Under the assumption that the grid Ξ is sufficiently fine, a low approximation error holds for all $\nu \in D$.

3.2.2 Error Estimator

The error estimator $\Delta_N(\nu)$ fulfills two roles. It is used in the offline phase to choose the snapshot locations and also in the online phase to measure the accuracy of the approximation with respect to the truth solution.

Let u_N denote the reduced order field solution, obtained after projecting the weak form onto X_N as

$$a(u_N(\nu), v_N; \nu) = f(v_N; \nu), \quad \forall v_N \in X_N. \tag{3.20}$$

Introducing the error $e(\nu)$ and the residual $r(\cdot;\nu)$ as

$$\begin{aligned} e(\nu) &= u(\nu) - u_N(\nu), \\ r(\cdot;\nu) &= f(\cdot;\nu) - a(u_N(\nu), \cdot;\nu), \end{aligned}$$

it holds

$$a(e(\nu), \cdot;\nu) = r(\cdot;\nu).$$

Let $\widehat{e}(\nu)$ denote the Riesz representer of the residual

$$(\widehat{e}(\nu), \cdot)_X = r(\cdot;\nu),$$

then it follows

$$a(e(\nu), \cdot;\nu) = (\widehat{e}(\nu), \cdot)_X, \tag{3.21}$$

$$(\widehat{e}(\nu), \cdot)_X = (T^\nu e(\nu), \cdot)_X, \tag{3.22}$$

$$\|r(\cdot;\nu)\|_{X'} = \|\widehat{e}(\nu)\|_X, \tag{3.23}$$

which means that $\widehat{e}(\nu) = T^\nu e(\nu)$ and $\|r(\cdot;\nu)\|_{X'} = \|T^\nu e(\nu)\|_X$.

The error estimator in the field is given by Lemma 3.2.1.

Lemma 3.2.1 (Error Estimator in the Electric Field)**.** *A rigorous error estimator in the electric field for the time-harmonic Maxwell's equations is given by*

$$\Delta_N(\nu) = \frac{\|r(\cdot;\nu)\|_{X'}}{\beta_{LB}(\nu)}, \tag{3.24}$$

with $\|r(\cdot;\nu)\|_{X'}$ the dual norm of the residual with respect to the truth solution, and $\beta_{LB}(\nu)$ is a lower bound to the discrete inf-sup stability constant $\beta(\nu)$.

The rigorous error estimator $\Delta_N(\nu)$ for the reduced basis approximation of order N satisfies

$$\|u(\nu) - u_N(\nu)\|_X \leq \Delta_N(\nu), \tag{3.25}$$

since it holds

$$\|e(\nu)\|_X = \|e(\nu)\|_X \frac{\|r(\cdot;\nu)\|_{X'}}{\|T^\nu e(\nu)\|_X} = \frac{\|r(\cdot;\nu)\|_{X'}}{\frac{\|T^\nu e(\nu)\|_X}{\|e(\nu)\|_X}} \leq \frac{\|r(\cdot;\nu)\|_{X'}}{\inf_{w\in X} \frac{\|T^\nu w\|_X}{\|w\|_X}} = \frac{\|r(\cdot;\nu)\|_{X'}}{\beta(\nu)}. \tag{3.26}$$

Often one is interested in an output quantity of interest, which can be expressed as a linear functional of the field solution $\ell(u(\nu))$, and thus the error in the output is expressed as

$$|\ell(u(\nu)) - \ell(u_N(\nu))| = |\ell(u(\nu) - u_N(\nu))|. \tag{3.27}$$

A trivial bound is given by

$$|\ell(u(\nu) - u_N(\nu))| \leq \|\ell(\cdot)\|_{X'} \|u(\nu) - u_N(\nu)\|_X, \tag{3.28}$$

which usually is not very sharp. Good a posteriori error bounds on the output quantity can be derived by considering a primal-dual setup, see the subsection 3.3.5 or the section on noncompliant problems in [RHP08].

In the special case of a compliant output, where the input functional f and the output functional ℓ are identical, i.e., $\ell = f$, it holds [RHP08], [Sen07]

$$|\ell(u(\nu)) - \ell(u_N(\nu))| = \frac{\|r(\cdot;\nu)\|^2_{X'}}{\beta_{LB}(\nu)}. \tag{3.29}$$

Several examples of compliant problems are given in [RHP08]. For instance an elastic block problem is shown, where the input functional is the normal stress on

a boundary, which also corresponds to the output functional, namely the integrated displacement functional.

The computation of $\beta(\nu)$ for (3.24) requires the solution of a large-scale eigenvalue problem, which is not feasible in an offline-online context. Therefore, a successive constraint method is used to obtain lower bounds $\beta_{LB}(\nu)$ to the stability constant $\beta(\nu)$. For technical details see [HRSP07] and chapter 5. For Maxwell's equations, the SCM has proven to be the computational "bottleneck" of the offline phase ([CHMR09]) as it requires to solve a large number of eigenvalue and linear optimization problems. The SCM for the generation of lower bounds to the stability constant is given in chapter 5. An advanced technique, which is more computationally involved is the natural norm SCM [HKC+10]. The natural norm SCM reduces the complexity from $O(Q_a^2)$ to $O(Q_a)$. To ensure online efficiency, $\mathcal{N}$-independent computations of the dual norm of the residual as well as $\beta_{LB}(\nu)$ are required.

Besides the absolute error, the relative error is a meaningful measure of the approximation quality. An estimate of the relative error with respect to the reduced solution is given by

$$\frac{\|u(\nu) - u_N(\nu)\|_X}{\|u_N(\nu)\|_X} \leq \frac{\Delta_N(\nu)}{\|u_N(\nu)\|_X}, \tag{3.30}$$

while an estimate of the relative error with respect to the full solution is derived using the triangle inequality as in chapter 5 of [Yue12] from

$$\frac{\|u(\nu) - u_N(\nu)\|_X}{\|u(\nu)\|_X} \leq \frac{\frac{\|u(\nu)-u_N(\nu)\|_X}{\|u_N(\nu)\|_X}}{\left|1 - \frac{\|u(\nu)-u_N(\nu)\|_X}{\|u_N(\nu)\|_X}\right|}, \tag{3.31}$$

which under the assumption of $1 - \frac{\|u(\nu)-u_N(\nu)\|_X}{\|u_N(\nu)\|_X} > 0$ and $\frac{\Delta_N(\nu)}{\|u_N(\nu)\|_X} < 1$ gives the relative error estimator in the electric field, Lemma 3.2.2.

Lemma 3.2.2 (Relative Error Estimator in the Electric Field)**.** *The relative error in the electric field of the time-harmonic Maxwell's equations w.r.t. the full order solution is given by*

$$\frac{\|u(\nu) - u_N(\nu)\|_X}{\|u(\nu)\|_X} \leq \frac{\frac{\Delta_N(\nu)}{\|u_N(\nu)\|_X}}{1 - \frac{\Delta_N(\nu)}{\|u_N(\nu)\|_X}}. \tag{3.32}$$

3.2.3 Dual Norm of the Residual

To compute the dual norm of the residual efficiently, the affine expansion (3.14) is used:

$$
\begin{aligned}
r(v;\nu) &= f(v) - a(u_N(\nu), v; \nu) \\
&= f(v) - a(\sum_{n=1}^{N} \alpha_n(\nu)\zeta_n, v; \nu) \\
&= f(v) - \sum_{n=1}^{N} \alpha_n(\nu) a(\zeta_n, v; \nu) \\
&= f(v) - \sum_{n=1}^{N} \alpha_n(\nu) \sum_{q=1}^{Q_a} \Theta_a^q(\nu) a^q(\zeta_n, v). \qquad (3.33)
\end{aligned}
$$

It holds

$$
(\widehat{e}(\nu), v)_X = f(v) - \sum_{q=1}^{Q_a} \sum_{n=1}^{N} \Theta_a^q(\nu)\alpha_n(\nu) a^q(\zeta_n, v), \qquad (3.34)
$$

$$
\widehat{e}(\nu) = C + \sum_{q=1}^{Q_a} \sum_{n=1}^{N} \Theta_a^q(\nu)\alpha_n(\nu)\mathcal{L}_n^q, \qquad (3.35)
$$

where C and $\mathcal{L}_n^q$ are solutions to the associated symmetric, positive definite systems, sometimes referred to as "FE Poisson" problems in the RB literature,

$$
(C, v)_X = f(v) \quad \forall v \in X, \qquad (3.36)
$$

$$
(\mathcal{L}_n^q, v)_X = -a^q(\zeta_n, v), \quad \forall v \in X. \qquad (3.37)
$$

This results in

$$
\begin{aligned}
\|\widehat{e}(\nu)\|_X^2 &= (C + \sum_{q=1}^{Q_a} \sum_{n=1}^{N} \Theta_a^q(\nu)\alpha_n(\nu)\mathcal{L}_n^q, \\
&\quad C + \sum_{q=1}^{Q_a} \sum_{n=1}^{N} \Theta_a^q(\nu)\alpha_n(\nu)\mathcal{L}_n^q)_X \\
&= (C, C)_X + \sum_{q=1}^{Q_a} \sum_{n=1}^{N} \Theta_a^q(\nu)\alpha_n(\nu) \times \\
&\quad \left\{ 2(C, \mathcal{L}_n^q)_X + \sum_{q'=1}^{Q_a} \sum_{n'=1}^{N} \Theta^{q'}(\nu)\alpha_{n'}(\nu)(\mathcal{L}_n^q, \mathcal{L}_{n'}^{q'})_X \right\}. \qquad (3.38)
\end{aligned}
$$

In particular, the full order solution is not required to compute the dual norm of the residual once C and $\mathcal{L}_n^q$ are computed. The complexity of the a posteriori error estimation scales with $O(Q_a^2 N^2)$, Lemma 3.2.3. To achieve a numerically stable implementation, see [BEOR14].

Lemma 3.2.3 (Complexity of the Residual Norm Computation)**.** *The complexity of the residual computation of the time-harmonic Maxwell's equations* (3.38) *scales with* $O(Q_a^2 N^2)$.

3.2.4 Example

Consider a coplanar waveguide model, governed by the time-harmonic Maxwell's equations as

$$-\epsilon\omega^2 E + \imath\omega\sigma E + \nabla \times \frac{1}{\mu}\nabla \times E = -\imath\omega j_i \quad \text{in } \Omega, \tag{3.39}$$

subject to zero boundary conditions

$$E \times n = 0 \quad \text{on } \Gamma_{\text{PEC}},$$

where $\Gamma_{\text{PEC}} = \partial\Omega$.

This example is concerned with a frequency sweep, i.e., the evaluation of the transfer function over a certain frequency range $[\omega_{\min}, \omega_{\max}]$. Considered input and output ports represent an impressed current and an output voltage, respectively. This model is investigated in more detail in section 4.1 and a related model is discussed in [BH12]. The quantity of interest is the modulus of the transmission coefficient or impedance, i.e., the ratio between the output and the input. Applying a normalized input, the quantity of interest is essentially the output voltage.

The output voltage u is given as the integral of the field solution over a one-dimensional filament Γ_{out} in the three-dimensional computational domain

$$u = \ell(E) = \int_{\Gamma_{\text{out}}} E dx. \tag{3.40}$$

Note that $\ell(\cdot)$ does not depend explicitly on the parameter ω, but implicitly through $E = E(\omega)$. Fig. 3.1 shows the transfer function $\|H(i\omega)\| = |u(\omega)|$ in dB against the frequency range. Fig. 3.2 shows the results of evaluating the reduced models of sizes 10, 20 and 30. The maximum and mean relative errors of the transfer function of the reduced model are shown in Table 3.1. For the sampled frequency range Ξ with 400 equally spaced samples, the maximum relative error is computed as $\max_{\omega\in\Xi} \left| \frac{u(\omega)-u_N(\omega)}{u(\omega)} \right|$ and the mean relative error is computed as

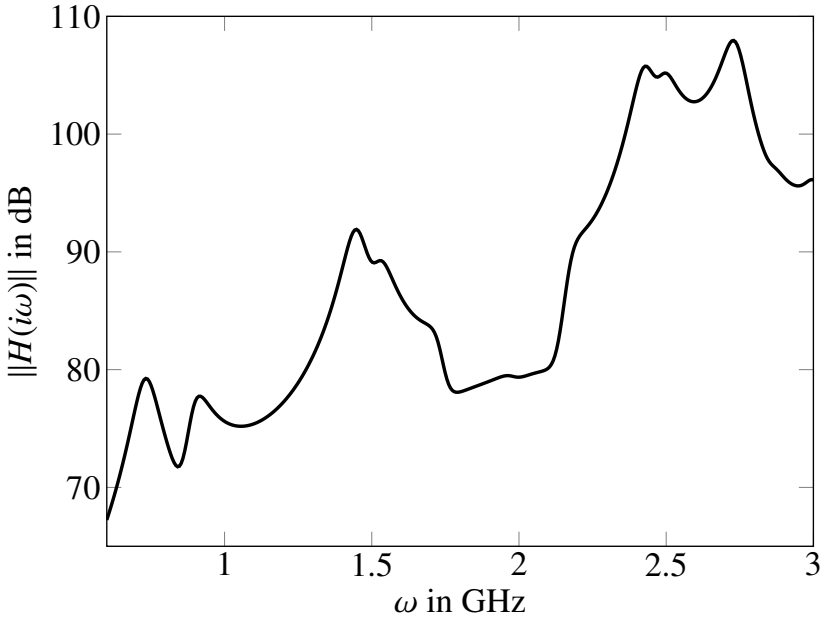

Figure 3.1: Frequency response of the coplanar waveguide model in $[0.6, 3.0]$ GHz.

$\frac{1}{|\Xi|}\sum_{\omega\in\Xi}\left|\frac{u(\omega)-u_N(\omega)}{u(\omega)}\right|$. In Table 3.2 the same error quantities are computed for 400 randomly selected samples. It becomes obvious, that a reduced model size of 30 might lead to a worse approximation than a reduced model size of 10. The comparable results of Table 3.1 and Table 3.2 verify, that this behavior does extend over the whole frequency range and not only the parameter samples used in the RBM.

Although the reduced model sizes increase, the approximation quality can degrade. In particular the reduced model can introduce resonances when no resonances are found in the full order model. In [BH12], the error decay in the median relative error is shown, which does not make the unwanted resonances visible.

Since the stability constant $\beta_N(\omega)$ of the reduced model is given by

$$\beta_N(\omega) = \inf_{w\in X_N}\sup_{v\in X_N}\frac{|a(w,v;\omega)|}{\|w\|_X\|v\|_X},$$

the case $\beta_N(\omega) = 0$, while $\beta(\omega) > 0$, is frequently observed. This problem can be overcome by using a two-sided, or Petrov-Galerkin projection, which guarantees $\beta_N(\omega) > \beta(\omega)$, and thus stability. This is the topic of the next section.

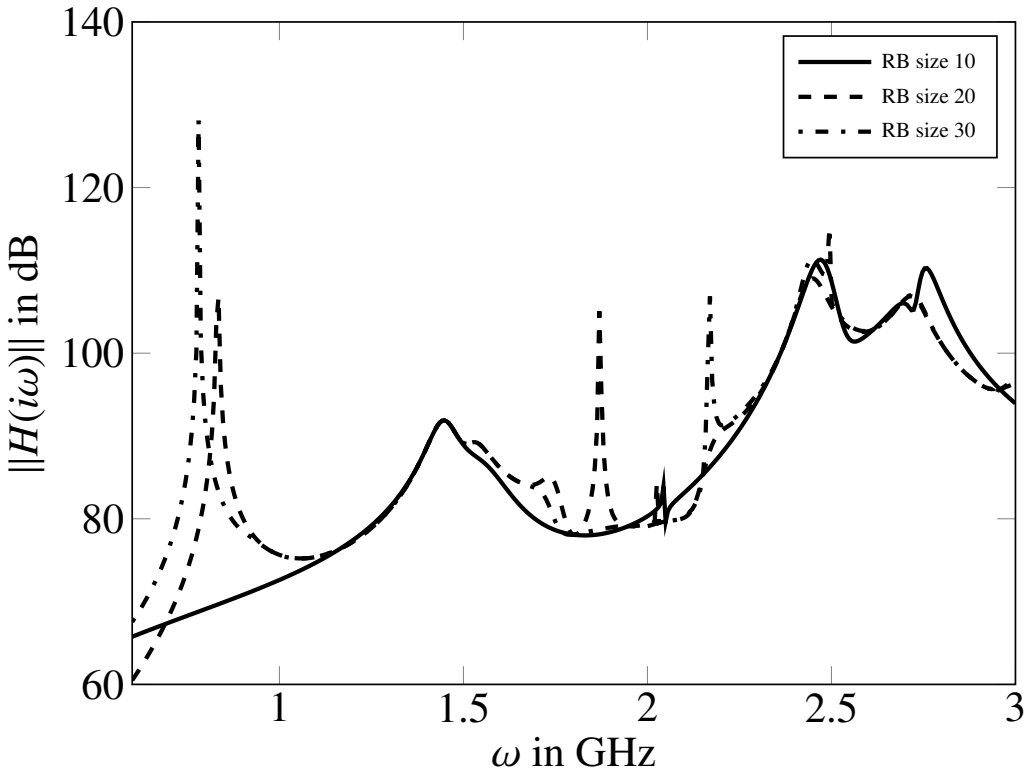

Figure 3.2: Frequency responses of the reduced models for the coplanar waveguide model in $[0.6, 3.0]$ GHz.

Table 3.1: Maximum and mean relative error in the transfer function evaluated at the sample locations used in the RB model reduction.

RB size	**maximum relative error**	**mean relative error**
10	1.102	0.230
15	118.7	1.350
20	54.39	0.587
25	49.45	0.540
30	399.5	1.324
50	0.060	0.001

Table 3.2: Maximum and mean relative error in the transfer function evaluated at randomly generated the sample locations.

RB size	**maximum relative error**	**mean relative error**
10	1.103	0.215
15	117.1	1.304
20	381.9	1.411
25	209.7	0.967
30	169.9	0.694
50	0.042	0.001

3.3 Reduced Basis Method in Electromagnetics

While the RBM is applicable to parametrized PDEs in general, this section does introduce more detail of some technical aspects of the RBM, which have turned out as useful in electromagnetic applications. In particular the Petrov-Galerkin projection, also termed two-sided projection, is presented and the transformation of geometric parameters to a reference configuration. Note that the mathematical tools applied for the geometric parameters are the same as used in the finite element assembly, see section 2.3.2. Additionally, details on Taylor reduced basis spaces, advanced error estimation procedures and reduction of time-dependent Maxwell's equations are given.

3.3.1 Petrov-Galerkin Reduced Basis

To preserve stability, it is required that $\beta_N(\nu) \geq \beta(\nu)$, where $\beta_N(\nu)$ is the stability constant of the reduced order system for a parameter vector ν. This is not necessarily satisfied when using Ritz-Galerkin RB-approximations. However, a Petrov-Galerkin approximation can achieve stability preservation, when chosen appropriately [MPR02].

Define the supremizing operator $T^\nu : X \to X$ by

$$(T^\nu u, \cdot) = a(u, \cdot; \nu), \tag{3.41}$$

and define the test space $\widetilde{X}_N^\nu = \text{span}\{T^\nu \zeta_i | i = 1, ..., N\}$ for a given trial space $X_N = \text{span}\{\zeta_i | i = 1, ..., N\}$. The term supremizing operator arises from the fact that with definition (3.8), T^ν is the Riesz representor of the linear form, obtained from the second argument of the bilinear form $a(\cdot, \cdot; \nu)$ and satisfies

$$\|T^\nu u\|_{X'} = \max_{v \in X} \frac{a(u, v; \nu)}{\|v\|_X}, \tag{3.42}$$

and the maximum is attained by $v = T^\nu u$.

With the linear operators $T^q : X \to X$ defined by

$$(T^q u, \cdot) = a^q(u, \cdot; \nu), \quad \forall q = 1, \ldots, Q_a, \tag{3.43}$$

the supremizing operator satisfies the same affine expansion as the bilinear form (3.14)

$$T^\nu u = \sum_{q=1}^{Q_a} \Theta_a^q(\nu) T^q u. \tag{3.44}$$

Given a reduced basis trial space $X_N = \text{span}\{\zeta_1, \ldots, \zeta_N\}$, a parameter-dependent test space is defined as $\widetilde{X}_N^\nu = T^\nu X_N$. From (3.6)-(3.9), the following relation holds between the stability constant $\beta_N(\nu)$ of the reduced model using a two-sided projection and the full model stability constant $\beta(\nu)$:

Lemma 3.3.1 (Stability of Petrov-Galerkin Projection)**.** *The projection with trial space X_N and test space $\widetilde{X}_N^\nu$ achieves stability preservation for the time-harmonic Maxwell's equations, i.e.,*

$$\beta_N(\nu) \geq \beta(\nu). \tag{3.45}$$

Proof:

$$\begin{aligned}
\beta_N(\nu) &= \inf_{u \in X_N} \sup_{v \in \widetilde{X}_N^\nu} \frac{a(u, v; \nu)}{\|u\|_X \|v\|_X} \\
&= \inf_{u \in X_N} \frac{a(u, T^\nu u; \nu)}{\|u\|_X \|T^\nu u\|_X} \\
&= \inf_{u \in X_N} \frac{(T^\nu u, T^\nu u)_X}{\|u\|_X \|T^\nu u\|_X} \\
&= \inf_{u \in X_N} \frac{\|T^\nu u\|_X}{\|u\|_X} \\
&\geq \inf_{u \in X} \frac{\|T^\nu u\|_X}{\|u\|_X} \\
&= \beta(\nu).
\end{aligned}$$

The parameter-dependent test space V_N^ν introduces another affine expansion in the offline-online decomposition, as each trial function ζ_i has a corresponding test function $T^\nu \zeta_i$, which can be expanded as

$$T^\nu \zeta_i = \sum_{q=1}^{Q_a} \Theta_a^q(\nu) T^q \zeta_i. \tag{3.46}$$

Using a two-sided approximation, the system (3.17) becomes

$$\begin{aligned} \sum_{n=1}^{N} a(\zeta_n, \sum_{q=1}^{Q_a} \Theta_a^q(\nu) T^q \zeta_m; \nu) \alpha_n(\nu) \\ = \sum_{q=1}^{Q_a} \Theta_a^q(\nu) f(T^q \zeta_m), \qquad 1 \leq m \leq N, \end{aligned} \tag{3.47}$$

where the left-hand-side can be expanded into

$$\sum_{n=1}^{N} \left(\sum_{q=1}^{Q_a} \sum_{q'=1}^{Q_a} \Theta_a^q(\nu) \Theta_a^{q'}(\nu) a^q(\zeta_n, T^{q'} \zeta_m) \right) \alpha_n(\nu). \tag{3.48}$$

During the offline phase, the forms $a^q(\zeta_n, T^{q'}\zeta_m)$ are generated and stored as small $N \times N$ matrices and can be efficiently evaluated online.

Let $V_N \in \mathbb{R}^{\mathcal{N} \times N}$ denote the coefficient matrix associated with the reduced basis $\{\zeta_1, \ldots, \zeta_N\}$ when they are represented by the finite element basis. Since the functions ζ_i are orthonormalized, it holds $V_N^T V_N = I_N$, with I_N the $N \times N$ identity matrix. The matrix representation of the test space is $W_N^\nu = T^\nu V_N$. The operator T^ν is computed as $T^\nu = M^{-1} A^\nu$ with the inner product matrix M defined in (3.11). Since M^{-1} is a dense matrix, the computation can only be performed as an action on a vector $T^\nu u$ in large-scale computations. Instead of explicitly computing M^{-1}, N linear systems are solved to obtain $T^\nu V_N$.

3.3.2 Example

This section revisits the model setup from example 3.2.4, but a Petrov-Galerkin reduced basis defined using the supremizing operators is applied instead. In Fig. 3.3 the mean and maximum relative errors in the transfer function are plotted against the reduced basis size. Comparing with Table 3.1, the error decay is smoother and no big oscillations occur anymore.

While the assembly of the reduced system needs an additional affine expansion for the parameter-dependent test spaces, the asymptotic runtime does not increase. The evaluation of the residual already depends quadratically on Q_a, which is the same complexity as for the assembly of the reduced system with Petrov-Galerkin projection.

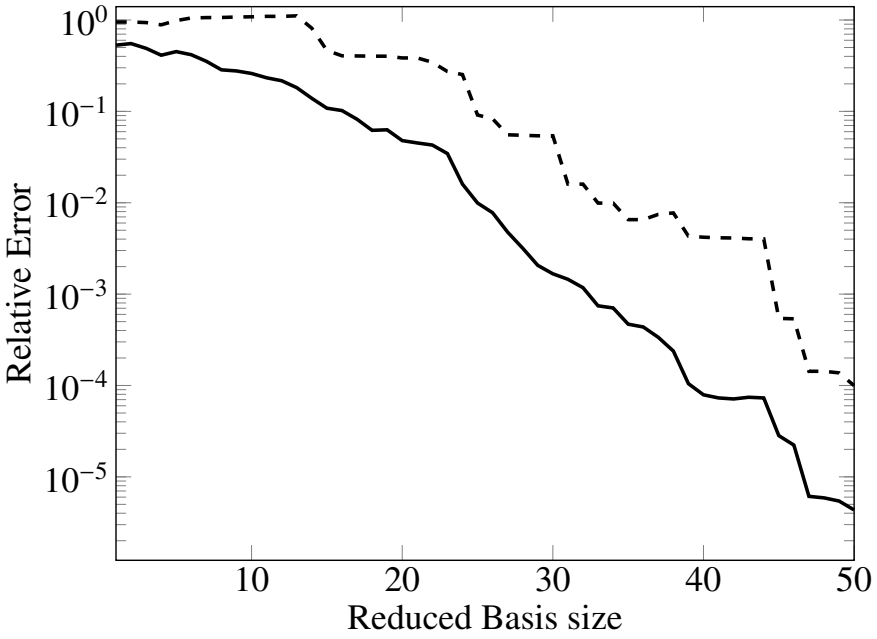

Figure 3.3: Relative errors plotted against the dimension of the reduced model, mean relative error (solid line) and maximum relative error (dashed line).

Remark

The stabilizing projection solves the normal equations known from the linear least squares procedure, in the projection space V_N w.r.t. the norm induced by M, since it solves $V_N^T A^T M^{-1} A V_N x = V_N^T A^T M^{-1} b$, dropping the parameter ν for notational convenience.

This is also related to residual minimization, since the ansatz $\min_{v \in V_N} \|b - Av\|_X$ also leads to the stabilizing projection [CFCA13].

3.3.3 Geometric Parameters

Production processes in the semiconductor industry are a complex procedure. Inaccuracies in the produced geometry are a sensitive matter, since this changes system behavior. As an example, variable widths of microstriplines will be considered in the chapters on numerical parameter studies. To incorporate geometric parameters in the reduced basis framework, a particular treatment is necessary. Due to the linear nature of Maxwell's equations, an affine dependence on geometric parameters is often given. However, the computational domain requires a division into subsections, such that a unique affine dependence holds in each subsection. The consideration of the linear combination of snapshots for different geometries, is then possible by taking

each snapshot in a reference configuration.

A geometric parameter is explicitly denoted in the computational domain as $\Omega = \Omega(\nu)$. The PDE is transformed from the parameter-dependent domain $\Omega(\nu)$ to a parameter-independent reference domain $\Omega(\overline{\nu})$. Quantities (i.e. operators and functions) defined on the reference domain are indicated by an overline to distinguish them from quantities defined on the actual domain. A reference configuration $\overline{\nu}$ is defined such that there exist affine mappings from an actual domain $\Omega(\nu)$ to $\Omega(\overline{\nu})$.

First the computational domain $\Omega(\nu)$ is partitioned into disjoint regions $\Omega^k(\nu)$, such that there exist affine mappings T^k from the respective regions of the reference configuration to the real configuration

$$\begin{aligned} T_k : \Omega^k(\overline{\nu}) \to \Omega^k(\nu) : \\ \overline{x} \mapsto x = G^k(\nu)\overline{x} + D^k(\nu), \quad \text{with} \\ G^k(\nu) \in \mathbb{R}^{3\times 3}, \quad D^k(\nu) \in \mathbb{R}^3. \end{aligned} \tag{3.49}$$

Many geometric variations allow such a decomposition. In section 4.1 a geometric variation in a coplanar waveguide is shown. The affine mappings are piecewise bijective and collectively continuous, so that a global mapping T can be defined by

$$T : \Omega(\overline{\nu}) \to \Omega(\nu) : \overline{x} \mapsto x = T_k(\overline{x}) \quad \forall \overline{x} \in \Omega^k(\overline{\nu}). \tag{3.50}$$

Using the Piola transformation for H(curl; Ω)-conforming integral transforms in three spatial dimensions, it holds

$$\begin{aligned} \nabla \times v &= |\mathrm{det}G(\nu)| G(\nu)(\overline{\nabla} \times \overline{v}) \circ T^{-1}, \\ v &= (G^{-T}(\nu)\overline{v}) \circ T^{-1}. \end{aligned}$$

The time-harmonic Maxwell's equations are mapped to the reference domain using standard Finite Element transformations of H(curl; Ω) as stated in Lemma 3.3.2.

Lemma 3.3.2. *Geometry Transformation*
Given an affine transformation $T : \Omega(\overline{\nu}) \to \Omega(\nu)$, it holds

$$\begin{aligned} &\int_{T(\Omega(\overline{\nu}))} \mu^{-1}(\nabla \times E, \nabla \times v) + \imath\omega\sigma(E, v) - \omega^2\epsilon(E, v)\, dx \\ &= \int_{\Omega(\overline{\nu})} \mu^{-1} G^{-1}(\nu)(\nabla \times E, \nabla \times v) G^{-T}(\nu) |detG(\nu)| \\ &+ G^T(\nu) \left(\imath\omega\sigma(E, v) - \omega^2\epsilon(E, v)\right) G(\nu) \frac{1}{|detG(\nu)|}\, d\overline{x}. \end{aligned} \tag{3.51}$$

This allows an affine decomposition (3.14) and also rewriting the system into a real symmetric form (2.80).

3.3.4 Taylor Reduced Basis

In contrast to the Lagrange Reduced Basis space, which uses only snapshot solutions as $X_N = \{u(\nu_1), ..., u(\nu_N)\}$, the Taylor Reduced Basis space additionally takes derivatives w.r.t. the parameter into account [RHP08].

Thus, the RB space X_N is defined as

$$X_N = \{u(\nu_1), \partial_{\nu(1)}u(\nu_1), , \ldots, \partial_{\nu(p)}u(\nu_1), \ldots, u(\nu_N), \partial_{\nu(1)}u(\nu_N), , \ldots, \partial_{\nu(p)}u(\nu_N)\},$$

where $\partial_{\nu(i)}$ denotes partial derivatives with respect to the i-th component of the parameter vector ν. The Taylor RB space X_N is orthonormalized, as is the Lagrange RB space, to allow for a reasonable comparison of the size of the reduced spaces.

Two variants of the Taylor Reduced Basis are considered in chapter 4. With a Ritz-Galerkin projection, the space X_N is used for the ansatz space as well as test space, while the Petrov-Galerkin projection achieves stability preservation by using supremizing operators as explained in the subsection on Petrov-Galerkin Reduced Basis 3.3.1. The linear system to be solved for a snapshot location ν is

$$A^\nu u(\nu) = b,$$

with parameter-dependent system matrix A^ν and right hand side b. This allows to compute the derivative $\partial_{\nu(i)}u(\nu)$ by

$$\begin{aligned} \partial_{\nu(i)}(A^\nu u(\nu)) &= \partial_{\nu(i)}(b) \\ (\partial_{\nu(i)}A^\nu)u(\nu) + A^\nu(\partial_{\nu(i)}u(\nu)) &= 0 \end{aligned}$$

leading to the linear system

$$A^\nu(\partial_{\nu(i)}u(\nu)) = -(\partial_{\nu(i)}A^\nu)u(\nu).$$

3.3.5 Primal-Dual Error Estimation

As stated in (3.28), a bound on an output functional $\ell(\cdot)$ is given by

$$|\ell(u(\nu) - u_N(\nu))| \leq \|\ell(\cdot)\|_{X'}\|u(\nu) - u_N(\nu)\|_X \leq \|\ell(\cdot)\|_{X'}\Delta_N(\nu), \tag{3.52}$$

which is typically not very sharp. This can be improved upon using a primal-dual error estimation framework [GS02] and solving the adjoint equation, find $\psi \in X$, such that

$$a(\phi, \psi; \nu) = \ell(\phi; \nu), \quad \forall \phi \in X. \tag{3.53}$$

Through the adjoint equation, the dual residual $r^{du}(\cdot; \nu)$ is obtained, such that in combination with the primal residual $r^{pr}(\cdot; \nu)$

$$\Delta_N^s(\nu) = \frac{\|r^{pr}(\cdot; \nu)\|_{X'} \|r^{du}(\cdot; \nu)\|_{X'}}{\beta_{LB}(\nu)} \tag{3.54}$$

gives sharper, yet rigorous bounds in the output error. This setup can also be applied in the complex case, see [CHMR10]. Since the applications here seek the modulus of the output voltage, no linear functional can be given. It is instead possible to obtain a quadratic output after Maxwell's equations are cast into real form. This is outlined in the next subsection.

3.3.6 Quadratic Outputs

As was discussed in example 3.2.4, the output quantity of interest is the modulus of the output voltage, it holds

$$s(\nu) = |\ell(u)|, \tag{3.55}$$

where $\ell(\cdot)$ is a linear functional mapping to $\mathbb{C}$. As discussed in example 2.3.3, it is advantageous to equivalently transform the Maxwell's equation into the real form (2.80). Hence, the output should be reformulated accordingly by two functionals as

$$s(\nu) = \sqrt{\ell_1(u)^2 + \ell_2(u)^2}, \tag{3.56}$$

where $\ell_1(\cdot)$ and $\ell_2(\cdot)$ are identical except that one acts on the real part and one on the imaginary part of the solution. Let l_1 and l_2 be the two vectors of coefficients for $\ell_1(\cdot)$ and $\ell_2(\cdot)$. Define a quadratic form $Q(\cdot, \cdot)$ by the matrix $l_1 l_1^T + l_2 l_2^T$, then it holds

$$s^2(\nu) = Q(u(\nu), u(\nu)). \tag{3.57}$$

Following [Sen07], an expanded formulation can be derived, which leads to a compliant system. Compliant systems typically show very fast convergence of the reduced model output to the full model output under basis enrichment, see [RHP08].

Expanded Formulation

Define an expanded formulation

$$\mathcal{A}^\nu x = \mathcal{F} \tag{3.58}$$

by

$$\mathcal{A}^\nu = \begin{bmatrix} 2A^\nu - Q & -Q \\ -Q & -2A^\nu - Q \end{bmatrix}, \tag{3.59}$$

$$\mathcal{F} = \begin{bmatrix} b \\ -b \end{bmatrix}, \tag{3.60}$$

which is simplified from [Sen07], since A^ν is real symmetric.

Lemma 3.3.3 (Compliant Expanded System)**.** *For the parametric problem $\mathcal{A}^\nu x = \mathcal{F}$, it holds*

$$s^2(\nu) = \mathcal{F}^T x, \tag{3.61}$$

i.e., the output of interest is equivalent to the input of the expanded formulation.

To see this, let for some arbitrary, fixed ν be $x_1 + x_2$ the solution of the standard size system and $x_1 - x_2$ be such that it solves

$$A^\nu(x_1 + x_2) = b, \tag{3.62}$$

$$A^\nu(x_1 - x_2) = Q(x_1 + x_2). \tag{3.63}$$

Since A^ν is symmetric, it also holds

$$(x_1 + x_2)^T A^\nu = b^T. \tag{3.64}$$

The solution of the expanded system $\mathcal{A}^\nu x = \mathcal{F}$ is then given by $\begin{bmatrix} x_1 \\ x_2 \end{bmatrix}$, as

$$
\begin{aligned}
\mathcal{A}^\nu \begin{bmatrix} x_1 \\ x_2 \end{bmatrix} &= \mathcal{F} \\
&\iff \begin{cases} 2A^\nu x_1 - Qx_1 - Qx_2 = b \\ -Qx_1 - 2A^\nu x_2 - Qx_2 = -b \end{cases} \\
&\iff \begin{cases} 2A^\nu x_1 - Q(x_1 + x_2) = b \\ -2A^\nu x_2 - Q(x_1 + x_2) = -b \end{cases} \\
&\iff \begin{cases} 2A^\nu x_1 - A^\nu(x_1 - x_2) = b \\ -2A^\nu x_2 - A^\nu(x_1 - x_2) = -b \end{cases} \\
&\iff \begin{cases} A^\nu(x_1 + x_2) = b \\ -A^\nu(x_1 + x_2) = -b. \end{cases}
\end{aligned} \tag{3.65}
$$

For the output of the expanded system, it thus holds

$$
\begin{aligned}
\mathcal{F}^T \begin{bmatrix} x_1 \\ x_2 \end{bmatrix} &= b^T x_1 - b^T x_2 \\
&= b^T (x_1 - x_2) \\
&= (x_1 + x_2)^T A^\nu (x_1 - x_2) \\
&= (x_1 + x_2)^T Q (x_1 + x_2) \\
&= s^2(\nu).
\end{aligned} \tag{3.66}
$$

Remark

The transformation to the expanded system maintains the resonance configurations, as is shown in section 5.5.

In the course of rewriting the original complex finite element system to real symmetric form and by further applying the expanded formulation, the system size has quadrupled. The offline phase will thus become much slower, and make this approach only applicable when the original system sizes are small to moderate. The compliancy will however allow for sharper error estimates, see [Sen07].

To avoid numerical cancellation, the scaling of Q and A^ν must be observed. It is possible to rescale Q by a factor α, which will then carry over to the output, as in $(\alpha s(\nu))^2 = \mathcal{F}x$.

3.3.7 Time-Dependent Problems

A time-dependent formulation is typically treated with a POD-Greedy approach [Haa13], [HO08] or [HRS15] and even nonlinear problems are subjected to this technique, see [NRP09].

A single trajectory is condensed with a Proper Orthogonal Decomposition (POD), while a greedy sampling is used in the parameter domain. Given a time-stepping from $t_1, \ldots, t_{n_T}$ with corresponding solution trajectory $u(t_i, ; \nu)$, where $i = 1, \ldots, n_T$ for a parameter vector ν. A reduced trajectory is obtained by projection and denoted by $u_N(t_i, ; \nu)$

An error estimator $\Delta(\nu)$ over all time steps is defined by

$$\|u(t_n, \nu) - u_N(t_n, \nu)\| \leq \sum_{k=1}^{n} a^k b_{n-k} = \Delta(\nu), \tag{3.67}$$

where b_n is the residual at timestep n, and a is the inverse Lipschitz constant,

$$a = \sup_{n \in \{1,\ldots,n_T\}} \sup_{w \neq y} \frac{\|w - y\|}{\|f(w, t_n; \nu) - f(y, t_n; \nu)\|}. \tag{3.68}$$

Rigorous error estimation requires an upper bound on the inverse Lipschitz constant. This is neglected here due to large computational effort, and it is simply set as $a = 1$. This choice is used in the computations in chapter 7, such that (3.67) works as an error indicator.

Given a sampled parameter domain Ξ and a tolerance ϵ, the algorithm works as follows [Haa14]

Algorithm 2: POD-Greedy Algorithm

INPUT: sampled parameter domain Ξ, tolerance ϵ
OUTPUT: POD-Greedy samples S_N, projection space X_N

Choose $\nu_1 \in \Xi$ arbitrarily
Solve for $u(t_i; \nu_1)$, where $i = 1, \ldots, n_T$
Set $S_1 = \{\nu_1\}$
POD of trajectory gives initial projection basis X_N
Set $k = 1$
while $\max_\Xi \Delta(\nu) > \epsilon$ **do**
    Set $k = k + 1$;
    Set $\nu_k = \arg\max_\Xi \Delta(\nu)$
    Set $S_k = S_{k-1} \cup \{\nu_1\}$
    Solve model for $u(t_i; \nu_k)$

11: $e(t_i) = u(t_i; \nu_k) - \Pi_{X_N} u(t_i; \nu_k)$, where $i = 1, \ldots, n_T$
12: POD of trajectory and append modes to X_N
13: **end while**

The POD performs a singular value decomposition (SVD) on the orthogonal complement of the newly computed trajectory with respect to the current projection basis X_N. The projection onto the space X_N is denoted by the operator Π_{X_N} in the POD-Greedy algorithm. The modes corresponding to the largest singular values are then appended to the projection basis. This ensures that the most important information on the trajectory is appended due to the best approximation property of the SVD.

When the time trajectory is large, the POD can become infeasible to compute. A compression of the trajectory is thus useful and can be achieved by an adaptive snapshot selection [ZFLB15]. Successively removing vectors from the trajectory, when the angle to the last chosen vector is below a threshold angle, can significantly reduce the size of the trajectory, without impacting the approximation accuracy. A variation of this is looking at the angle between the current vector and the whole subspace, which has already been chosen.

4 Parameter Studies with the Reduced Basis Method

This chapter examines the application of the RBM to three example models, a coplanar waveguide, a branchline coupler[1] and a printed circuit board. These are 3-dimensional stripline models used in microwave engineering. Their input-output behavior is characterized by the complex transmission coefficient, i.e., the modulus of the ratio of the output voltage to an input current. In all these simulations, a normalized input is considered. This is a simplification from modeling the pattern of an incoming wave. The discrete ports, where input and output are defined, are 1-dimensional filaments in the 3-dimensional computational domain. As input, the value 1 is assumed over the 1-dimensional filament as a coarse approximation of an incoming wave. The correctness of the modeling and simulation of the transmission line models was established by comparing them with simulations obtained by the commercial EM-software 'CST Studio Suite'[2]. To obtain the transfer function over a certain frequency range requires many solves of the underlying electromagnetic model. When introducing further parameters, such as geometric and material parameters, this becomes unfeasible. Thus, the aim of this chapter is the assessment of the strengths and weaknesses of the reduced basis model reduction in this setting. It will be shown that, for a moderate number of parameters, the RBM is computationally beneficial.

A detailed model description is provided and the affine transformations (3.14) are shown. For the reference configuration, the parameter-independent matrices of the affine expansion can be found at the Model Reduction Wiki. Several results are given on the approximation quality the RBM computes. Assuming a predefined approximation tolerance, the aim is a small size of the reduced models. Some numerical aspects are emphasized, which are important to efficient and stable implementations. Additionally, the expanded form (see subsection 3.3.6) is used in a coarsely discretized model for a fast frequency sweep.

The microstrip models permit a tensor structure of the finite element mesh. First, a mesh of boxes is generated that respects the geometric features and then each box is decomposed into six tetrahedrons. The finite element package FEniCS [LMW12] pro-

[1] The coplanar waveguide and branchline coupler models are available through the Model Reduction Wiki, `www.modelreduction.org`.

[2] CST - Computer Simulation Technology, `www.cst.com`.

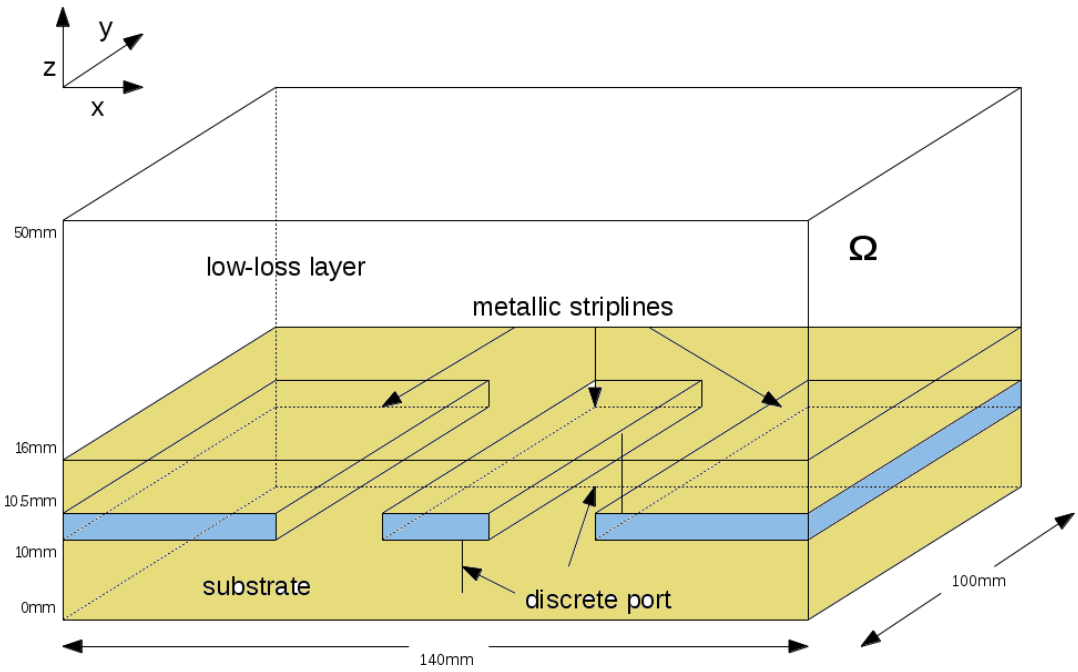

Figure 4.1: Coplanar waveguide geometry.

vides this functionality in the programming languages `Python` and `C++`. The FEniCS library assembles matrices corresponding to the affine parameter dependence (3.14), using a discretization with first order Nédélec finite elements. To perform the model reduction, these matrices are imported into the `C++` library libMesh [KPSC06] and into MATLAB®. When estimating the stability constant, the `C++` library libMesh uses the GLPK[3] which allows more complexity for solving linear optimization problems than the `linprog` command in MATLAB. The investigation of numerical aspects of the RBM is mainly implemented in MATLAB.

4.1 Coplanar Waveguide

The geometry of the coplanar waveguide model is shown in Fig. 4.1. It is a transmission line shielded by two layers of a multilayer board within a dielectric substrate overlay.

[3]GLPK - GNU Linear Programming Kit `www.gnu.org/software/glpk/`.

4.1.1 Model Description

The computational domain is bounded by a shielded box of dimension 140 mm by 100 mm by 50 mm. On all boundaries a PEC condition is enforced. The striplines are metallic, so that PEC conditions hold there as well. Thus, the interiors of the metallic striplines are not part of the computational domain. The substrate extends in the z-direction from 0 mm to 16 mm and the upper part is a low-loss layer. The discrete ports are defined as 1-dimensional filaments. Assuming the origin at the lower left and front corner in Fig. 4.1, the input port is located at x = 70 mm, y = 5 mm and extends in the z-direction from 0 mm to 10 mm, while the output port is located at x = 70 mm, y = 95 mm and extends in the z-direction from 0 mm to 10 mm.

The model is governed by the full time-harmonic Maxwell's equations and as a microwave device, it operates at frequencies of a few GHz.

Coplanar Waveguide Model

Define a bounding box $B_\Omega = [0, 140]$ mm $\times [0, 100]$ mm $\times [0, 50]$ mm.

Define the three striplines

$S_1 = [0, 62]$ mm $\times [0, 100]$ mm $\times [10, 10.5]$ mm,

$S_2 = [67, 73]$ mm $\times [0, 100]$ mm $\times [10, 10.5]$ mm,

$S_3 = [78, 140]$ mm $\times [0, 100]$ mm $\times [10, 10.5]$ mm.

The computational domain is given by $\Omega = B_\Omega \setminus (S_1 \cup S_2 \cup S_3)$.

It holds (2.25) in Ω, i.e., $-\epsilon\omega^2 E + \imath\omega\sigma E + \nabla \times \frac{1}{\mu}\nabla \times E = -\imath\omega j_i$,

subject to PEC boundary conditions on $\partial\Omega$, i.e., $E \times n = 0$.

The material coefficients in the substrate (z $\leq$ 16 mm) are given by

$\epsilon = 4.4\epsilon_0, \quad \mu = \mu_0, \quad \sigma = 0.02\frac{S}{m}$.

The material coefficients in the low-loss layer (z $>$ 16 mm) are given by

$\epsilon = 1.07\epsilon_0, \quad \mu = \mu_0, \quad \sigma = 0.01\frac{S}{m}$.

The input port is $\Gamma_{in} = 70$ mm $\times 5$ mm $\times [0, 10]$ mm.

The output port is $\Gamma_{out} = 70$ mm $\times 95$ mm $\times [0, 10]$ mm.

The source term is $j_i = 1$ on $\Gamma_{in}, \quad j_i = 0$ else.

The output is $l(E) = \int_{\Gamma_{out}} E dz$.

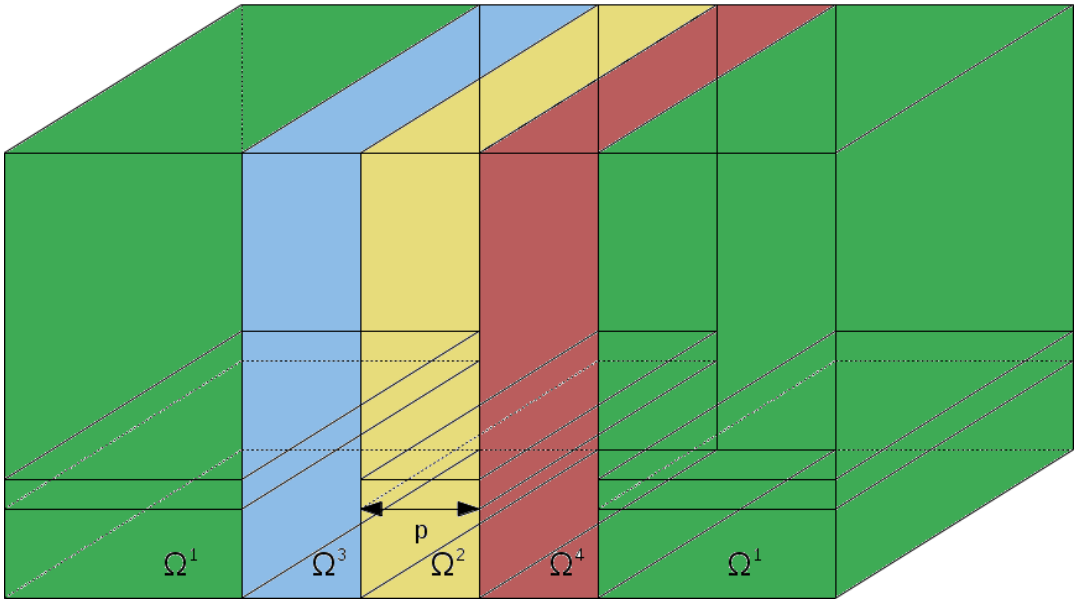

Figure 4.2: Coplanar waveguide subdomains used in the definition of the affine transformations.

This model description defines the reference configuration. Considered parameters are the frequency ω and the width of the middle stripline p.

4.1.2 Affine Transformation

To consider the linear combination of snapshots for different geometries and to work with the geometric parameter in an efficient way, an affine transformation to the reference geometry is established. The model is decomposed into subdomains $\Omega^1, \Omega^2, \Omega^3$ and Ω^4 as seen in Fig. 4.2. Note that this choice is not unique.

Quantities (i.e. operators and functions) defined on the reference domain are indicated by an overline to distinguish them from quantities defined on the actual domain.

When the width of the middle stripline changes from the reference value $\overline{p} = 6$ mm, there exist affine mappings T_k from the respective regions of the reference configuration to the actual configuration according to (3.49).

The subdomains are transformed according to T_1, T_2, T_3 and T_4 as

$$
\begin{aligned}
T_1 &: \Omega^1(\overline{p}) \to \Omega^1(p) : (x,y,z) \mapsto (x,y,z),\\
T_2 &: \Omega^2(\overline{p}) \to \Omega^2(p) : (x,y,z) \mapsto (p\frac{x-70}{6}+70,y,z),\\
T_3 &: \Omega^3(\overline{p}) \to \Omega^3(p) : (x,y,z) \mapsto ((x-62)\frac{16-p}{10}+62,y,z),\\
T_4 &: \Omega^4(\overline{p}) \to \Omega^4(p) : (x,y,z) \mapsto ((x-73)\frac{16-p}{10}+70+\frac{p}{2},y,z),
\end{aligned}
$$

which leads to the Jacobians

$$
G^1 = \begin{pmatrix} 1 & 0 & 0 \\ 0 & 1 & 0 \\ 0 & 0 & 1 \end{pmatrix}, \quad G^2 = \begin{pmatrix} \frac{p}{6} & 0 & 0 \\ 0 & 1 & 0 \\ 0 & 0 & 1 \end{pmatrix}, \quad G^3 = G^4 = \begin{pmatrix} \frac{16-p}{10} & 0 & 0 \\ 0 & 1 & 0 \\ 0 & 0 & 1 \end{pmatrix}.
$$

The affine mappings T^k are piecewise bijective and collectively continuous, so that a global mapping T can be defined by

$$
T : \Omega(\overline{\nu}) \to \Omega(\nu) : \overline{x} \mapsto x = T_k(\overline{x}), \quad \forall x \in \Omega^k(\overline{\nu}).
$$

The PDE is transformed from the parameter-dependent domain $\Omega(p)$ to a parameter-independent reference domain $\Omega(\overline{p})$.

The Piola transformation for H(curl; Ω)-conforming integral transforms is used to map differential quantities from the actual domain, see subsection 2.3.1. Thus, the PDE can be transformed to the reference domain, using standard FE-transformations of $H(\mathrm{curl})$ with the Piola transformation and the substitution rule

$$
\begin{aligned}
&\int\limits_{\Omega(\nu)=T(\Omega(\overline{\nu}))} \mu^{-1}(\nabla\times E,\nabla\times v) + \imath\omega\sigma(E,v) - \omega^2\epsilon(E,v)\,dx\\
&= \int_{\Omega(\overline{\nu})} \mu^{-1}G(\nu)(\overline{\nabla}\times\overline{E},\overline{\nabla}\times\overline{v})G^T(\nu)\frac{1}{|\mathrm{det}G(\nu)|}\\
&+ G^{-T}(\nu)\left(\imath\omega\sigma(\overline{E},\overline{v}) - \omega^2\epsilon(\overline{E},\overline{v})\right)G^{-1}(\nu)|\mathrm{det}G(\nu)|\,dx, \qquad (4.1)
\end{aligned}
$$

which allows an affine decomposition (3.14) and also to rewrite the system into a real symmetric form (2.80). In particular, this section takes $\omega \in [1.3, 1.6]$ GHz and $p \in [2, 14]$ mm into account. This is a substantial geometric variation, as the distance between the outer striplines is just 16 mm.

The affine expansion (3.14) contains $Q_a = 5$ terms when expanded in the geometric parameter only and $Q_a = 15$ terms when expanded in the frequency and the geometric

parameter, such that $\nu = [\omega, p]$. Since Ω^1 is not affected by the geometric parameter, it holds

$$\int\limits_{\Omega^1(\nu)} \mu^{-1}(\nabla \times E, \nabla \times v) + \imath\omega\sigma(E, v) - \omega^2\epsilon(E, v)\, dx$$
$$= \int\limits_{\Omega^1(\overline{\nu})} \mu^{-1}(\overline{\nabla} \times \overline{E}, \overline{\nabla} \times \overline{v}) + \imath\omega\sigma(\overline{E}, \overline{v}) - \omega^2\epsilon(\overline{E}, \overline{v})\, dx,$$

which gives three terms in the affine expansion with $\Theta_a^1(\nu) = 1$, $\Theta_a^2(\nu) = \omega$ and $\Theta_a^3(\nu) = -\omega^2$. The subdomain Ω^2 expands with p in the x-direction, such that it holds

$$\int\limits_{\Omega^2(\nu)} \mu^{-1}(\nabla \times E, \nabla \times v) + \imath\omega\sigma(E, v) - \omega^2\epsilon(E, v)\, dx$$
$$= \int_{\Omega^2(\overline{\nu})} \mu^{-1} G^2(\nu)(\overline{\nabla} \times \overline{E}, \overline{\nabla} \times \overline{v})(G^2)^T(\nu) \frac{1}{|\mathrm{det} G^2(\nu)|}$$
$$+ (G^2)^{-T}(\nu) \left(\imath\omega\sigma(\overline{E}, \overline{v}) - \omega^2\epsilon(\overline{E}, \overline{v})\right) (G^2)^{-1}(\nu) |\mathrm{det} G^2(\nu)|\, dx, \tag{4.2}$$

which gives six terms in the affine expansion, namely three terms in the x-coordinates, $\Theta_a^4(\nu) = \frac{p}{6}$, $\Theta_a^5(\nu) = \frac{6}{p}\omega$ and $\Theta_a^6(\nu) = -\frac{6}{p}\omega^2$ and three terms in the y and z-coordinates, $\Theta_a^7(\nu) = \frac{6}{p}$, $\Theta_a^8(\nu) = \frac{p}{6}\omega$ and $\Theta_a^9(\nu) = -\frac{p}{6}\omega^2$. In the same way, there are six affine terms originating from transforming $\Omega^3 \cup \Omega^4$, which have the same Jacobians $G^3 = G^4$

$$\int\limits_{\Omega^3(\nu)\cup\Omega^4(\nu)} \mu^{-1}(\nabla \times E, \nabla \times v) + \imath\omega\sigma(E, v) - \omega^2\epsilon(E, v)\, dx$$
$$= \int_{\Omega^3(\overline{\nu})\cup\Omega^4(\overline{\nu})} \mu^{-1} G^3(\nu)(\overline{\nabla} \times \overline{E}, \overline{\nabla} \times \overline{v})(G^3)^T(\nu) \frac{1}{|\mathrm{det} G^3(\nu)|}$$
$$+ (G^3)^{-T}(\nu) \left(\imath\omega\sigma(\overline{E}, \overline{v}) - \omega^2\epsilon(\overline{E}, \overline{v})\right) (G^3)^{-1}(\nu) |\mathrm{det} G^3(\nu)|\, dx, \tag{4.3}$$

such that $\Theta^1 0_a(\nu) = \frac{16-\nu}{10}$, $\Theta^1 1_a(\nu) = \frac{10\omega}{16-\nu}$ and $\Theta^1 2_a(\nu) = -\frac{10\omega^2}{16-\nu}$ acting on the x-coordinates and $\Theta^1 3_a(\nu) = \frac{10}{16-\nu}$, $\Theta^1 4_a(\nu) = \frac{16-\nu}{10}\omega$ and $\Theta^1 5_a(\nu) = -\frac{16-\nu}{10}\omega^2$ acting on the y and z-coordinates.

Due to the technical nature of this transformation, errors can happen when this form is established with pen and paper. It is helpful to assemble the system for

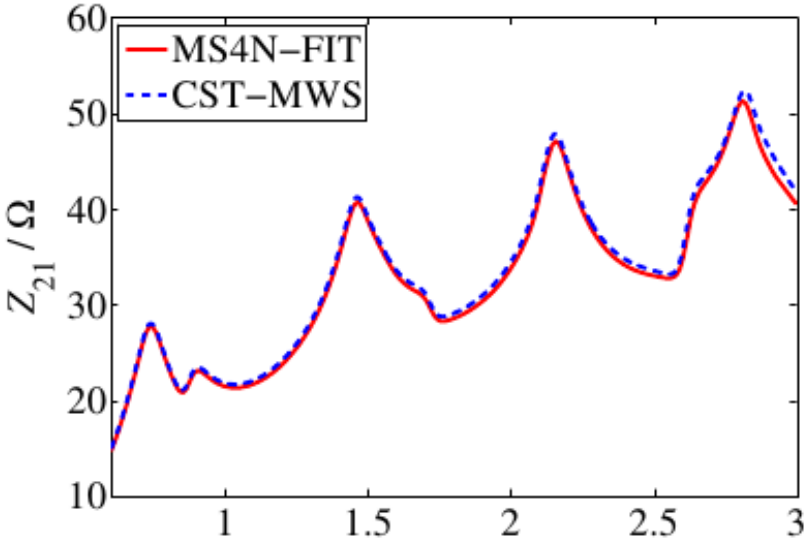

Figure 4.3: Coplanar waveguide: Frequency response over $[0.6, 3.0]$ GHz obtained through finite integration solvers.

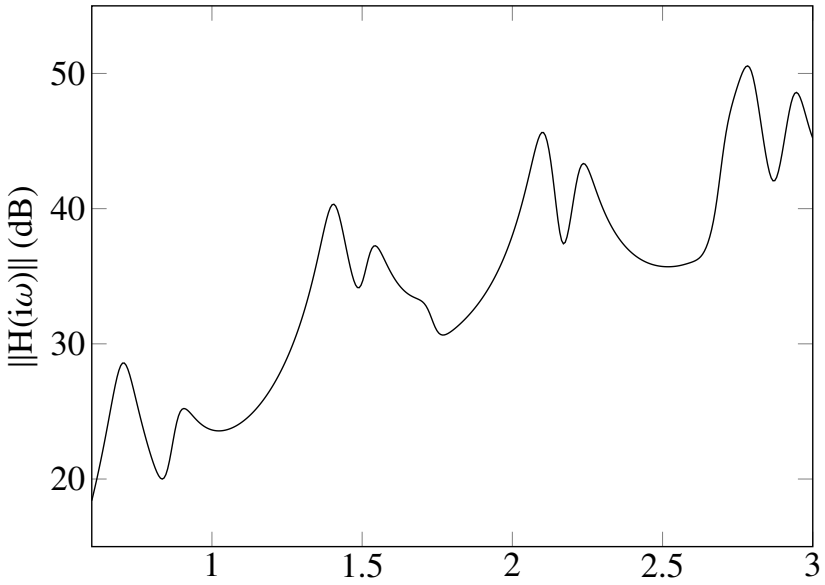

Figure 4.4: Coplanar waveguide: Frequency response over $[0.6, 3.0]$ GHz obtained through finite element solvers.

a different geometry configuration and check whether it matches with the result obtained through the affine transformation.

The assembly of the full order system has been performed with the finite element package FEniCS using a discretization with first order Nédélec finite elements. The full model of the coplanar waveguide contains 52,134 degrees of freedom in the real symmetric form (2.80). The discrete port shown in Fig. 4.2 serves as the input port, the output port is placed at the far side of the waveguide. To establish the correctness of our simulation, the results were compared with results obtained by the commercial EM-software 'CST Studio Suite'. In the course of the collaborative project MoreSim4Nano the frequency response shown in Fig. 4.3 was given for the coplanar waveguide. This is obtained through solvers using the finite integration technique. The results of this work do not match perfectly to these results as can be seen by comparing the results to Fig. 4.4. Since the accurate simulation of devices with various discretization techniques is beyond the scope of the current work, this is not further investigated.

4.1.3 Numerical Results

Fig. 4.5 shows the transfer function of the coplanar waveguide in the considered parameter domain $\omega \in [1.3, 1.6]$ GHz and $p \in [2, 14]$ mm. For comparison, the transfer function of the reduced order model of dimension $N = 45$ is shown in Fig. 4.6. For $N = 85$, the error between full order and reduced order model is plotted in Fig. 4.7. The chosen snapshot locations are visible, since the error is close to double precision at these locations.

The relative error $\frac{\|u(\nu)-u_N(\nu)\|_X}{\|u(\nu)\|_X}$ and the error estimator for the relative error $\frac{\Delta_N}{\|u_N(\nu)\|_X}$ are plotted in Fig. 4.8 over the reduced basis dimension N. The maximum and the arithmetic mean are computed over all $\nu \in \Xi$ for each RB-dimension N. An exponential convergence of the reduced basis solutions to the full order solutions can be observed. The RB space is computed over a uniformly sampled parameter space of 30 by 30 samples.

Due to the large number of affine terms ($Q_a = 15$), an approximation to the lower bound of the stability constant is used. In particular, only the upper bounds are computed, see chapter 5, by using a coarse uniform 10×30 grid, and the resulting upper bounds are scaled by a factor of 0.5 to achieve lower bounds. Numerical tests showed that the SCM generates sharp upper bounds [CHMR09], so that this approach is justified.

The mean of the estimator for the relative error $\frac{\|E^{\mathcal{N}}(\nu)-E_N(\nu)\|_{X^{\mathcal{N}}}}{\|E_N(\nu)\|_{X^{\mathcal{N}}}}$ is plotted in Fig. 4.9 for the Petrov-Galerkin Lagrange RB space, Galerkin Taylor RB space and Petrov-Galerkin Taylor RB space. Note that the Taylor RB spaces add three basis functions at each parameter location instead of one basis function as is the case

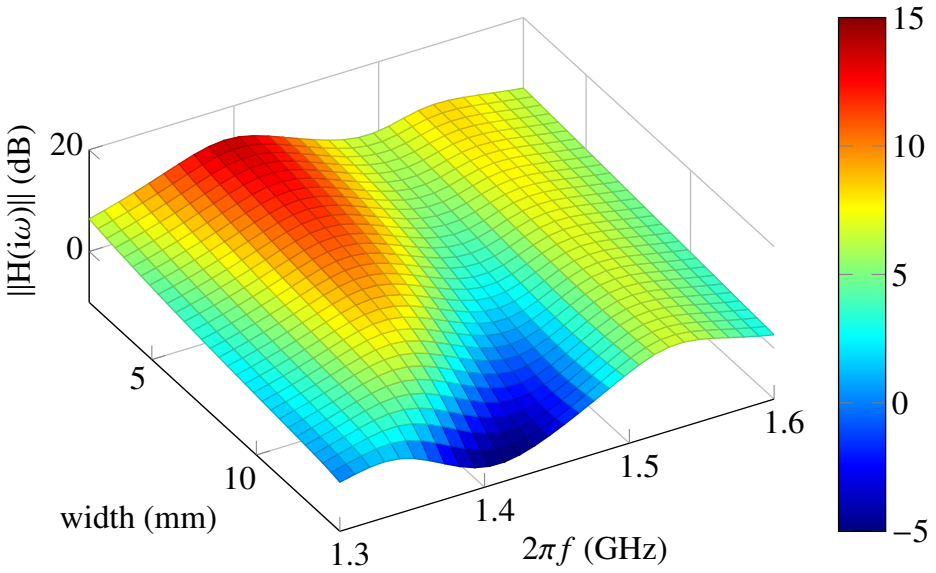

Figure 4.5: Coplanar waveguide: transfer function of full order model.

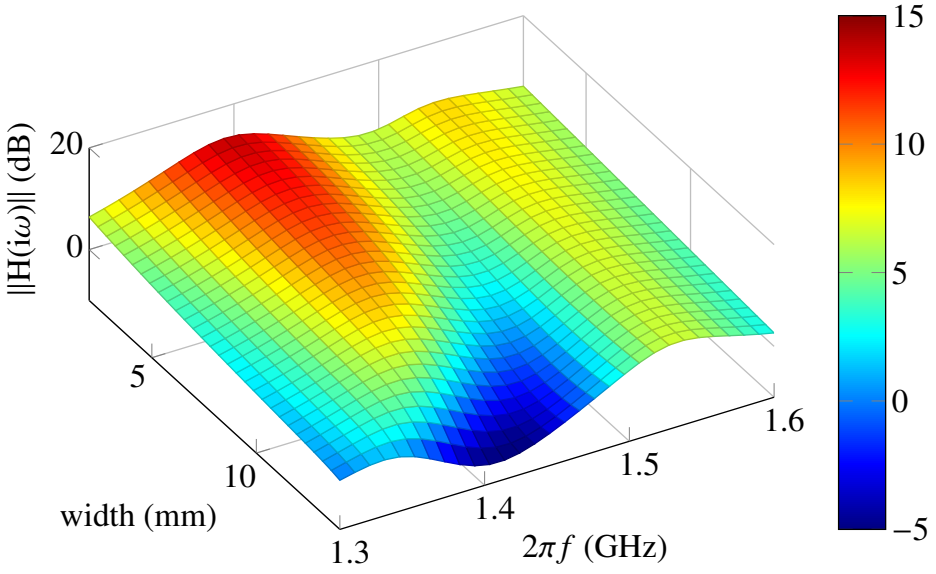

Figure 4.6: Coplanar waveguide: transfer function of the reduced order model of dimension $N = 45$.

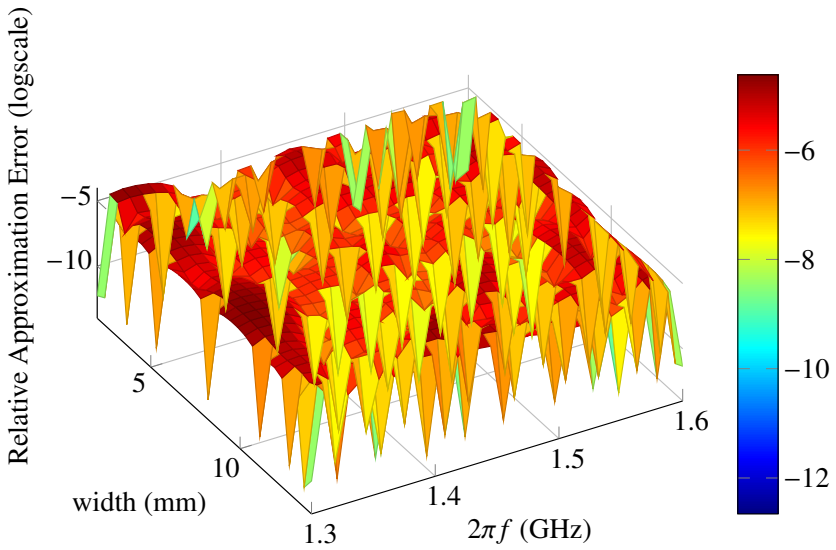

Figure 4.7: Coplanar waveguide: error between full order and reduced order model for $N = 85$.

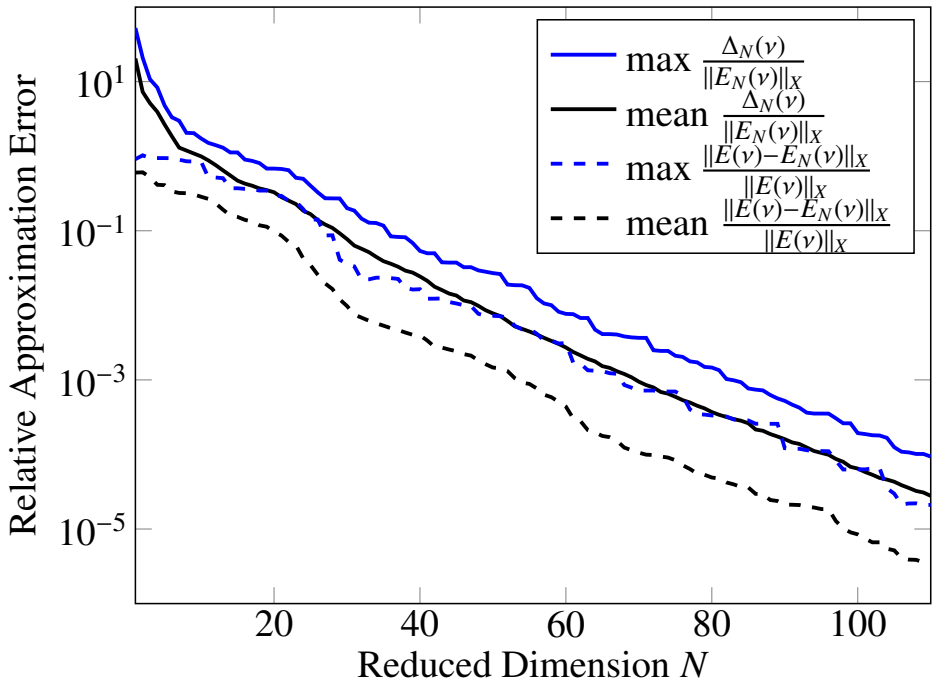

Figure 4.8: Relative error in the field solution plotted over the reduced basis dimension N for the coplanar waveguide.

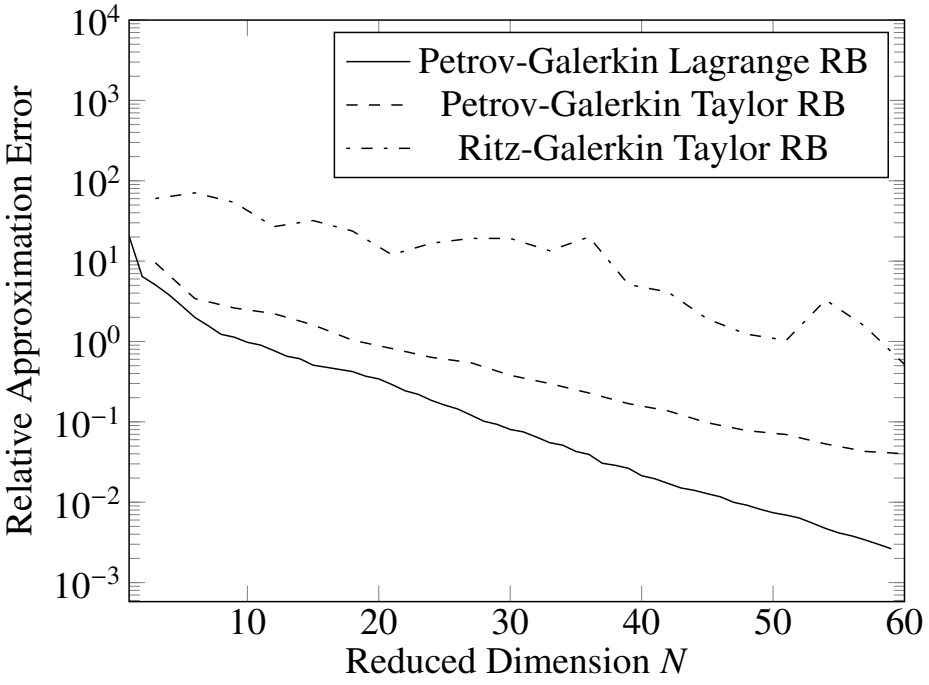

Figure 4.9: Coplanar waveguide: Taylor space mean relative error estimator $\frac{\Delta}{E_N}$.

for Lagrange RB spaces. The greedy algorithm ran until $N = 60$ basis functions. Fig. 4.9 shows that the Lagrange RB space performs significantly better in terms of required model order. All Petrov-Galerkin approximations show an exponential convergence speed. The mean of the actual absolute error $\|E^{\mathcal{N}}(\nu) - E_N(\nu)\|_X$ is plotted in Fig. 4.10 for the Petrov-Galerkin Lagrange RB space, Galerkin Taylor RB space and Petrov-Galerkin Taylor RB space. It also shows that the Lagrange RB space performs significantly better than the Taylor-RB spaces. In the actual relative error however, the Galerkin Taylor RB space and Petrov-Galerkin Taylor RB space show similar behavior.

4.1.4 Practical and Numerical Aspects

The timing to obtain the transfer behavior using the full order model is in the range of several hours, while it can be evaluated with the reduced order model in a few seconds, see also Table 4.1. However, the offline phase can also take up to several hours. This strongly depends on what level of accuracy in the stability constant estimation is desired. To put it in terms of practical applicability: When the offline timing is not a concern, or is performed on a supercomputer, a rigorous error estimation procedure is possible. When the offline timing is important and is only performed

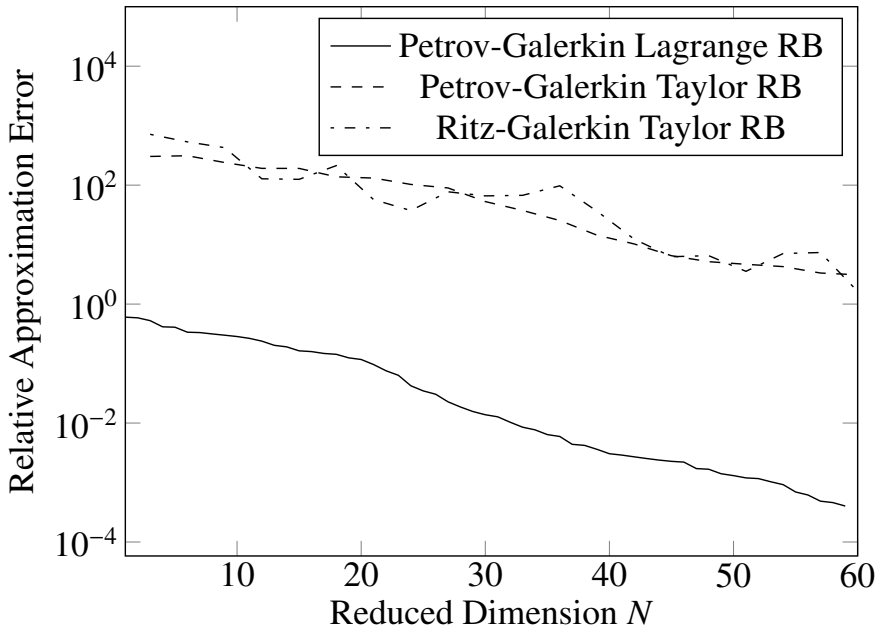

Figure 4.10: Coplanar waveguide: Taylor space mean actual absolute error in the H(curl; Ω) norm.

on a desktop machine, a non-rigorous error estimation is favorable. See chapter 5 for more details. When the offline timing is crucial, the stability constant estimation can also be neglected altogether, and the residual serves as an error indicator. This approach is used in chapter 6, where high-dimensional stochastic parameter spaces are of concern.

The greedy algorithm can either use the error estimator for the absolute error Δ or the relative error $\frac{\Delta}{\|E_N\|_X}$. Numerical experiments have shown, that the greedy tends to stall more easily when using the error estimator Δ. I.e., due to numerical inaccuracies in higher greedy iteration numbers, a parameter location gets chosen twice. This either leads to a singular projection matrix, or, when using orthonormalization, creates an infinite loop. This typically happens when the tolerance of the greedy is set below the numerical accuracy which can be expected. The numerical accuracy which can be expected depends mostly on the accuracy with which the high-dimensional linear system is solved.

The error estimator overestimates the actual error by a factor of about ten. Since the estimator is still strongly correlated with the actual error, this overestimation does not pose a problem here. After a few greedy iterations, the correlation coefficient between error estimator and actual error climbs to between 0.7 and 0.85.

The usage of Petrov-Galerkin projections requires multiple solves with the inner

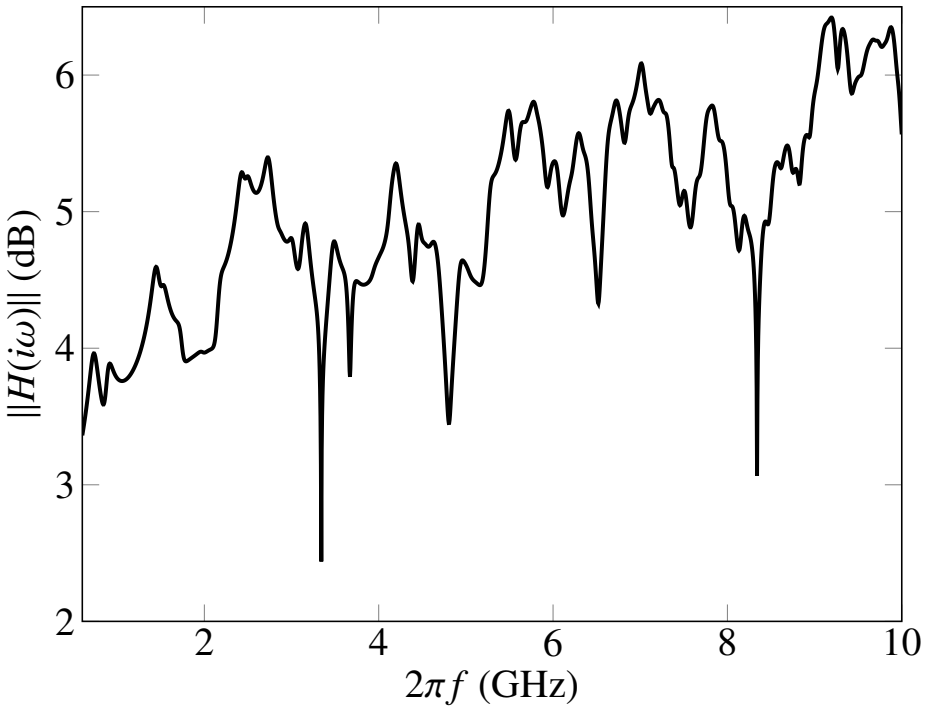

Figure 4.11: Coplanar waveguide: Transfer function over $[0.6, 10]$ GHz.

product matrix in each greedy iteration. An LU-decomposition of this matrix is thus computed a-priori.

Output Estimation Using the Expanded Formulation

The expanded formulation introduced in subsection 3.3.6 and derived from [Sen07] is used in a single parameter example, namely a fast frequency sweep. Consider the coplanar waveguide in an extended frequency range of $[0.6, 10]$ GHz. The transfer function is shown in Fig. 4.11.

Since the expanded formulation doubles the system size, a more coarse discretization is chosen. The real symmetric system contains $2'024$ degrees of freedom, after elimination of zero boundary conditions, such that the expanded form contains $4'048$ degrees of freedom. This is still very small, but using the full-sized system would have taken several weeks on the machine in use[4]. The error in the output is typically estimated using primal-dual methods. Since the transmission coefficient (or Z-parameter) is a quadratic output, a primal-dual estimation is not directly appli-

[4]The computations were done in MATLAB2012b on a Ubuntu 12.04 operating system with an Intel(R) Core(TM)2 Quad CPU Q6700 @ 2.66GHz with 8GB RAM.

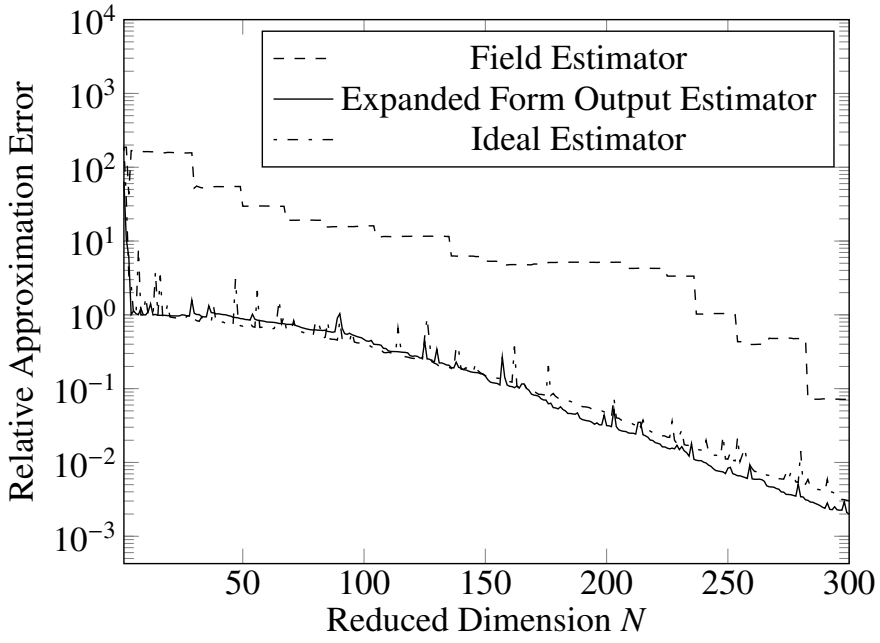

Figure 4.12: Coplanar waveguide: Maximum relative error in the output.

cable. Thus, the following comparison uses the field estimator for the non-expanded form. The expanded form is compliant, such that the field estimator is also the output estimator. Additionally, the comparison includes a so-called 'Ideal Greedy', which uses the exact errors in each greedy iteration. These data are not available in a practical setting.

As can be observed from the mean and maximum relative error in the output (Fig. 4.12 and Fig. 4.13), the ideal greedy sampling in the output is superior to the field estimator by about one order of magnitude. It can also be observed, that the expanded formulation leads to an accuracy, comparable to the ideal greedy. Concludingly, when the additional offline cost is affordable, the expanded form can generate very compact reduced order models.

Since the eigenvalues of the system matrix of the expanded formulation change, the stability constant estimation has to be done again. For this numerical experiment, the stability constant has been set to one in all estimators. It can however be expected, that with a better stability constant estimation, the methods perform even better compared to the ideal greedy.

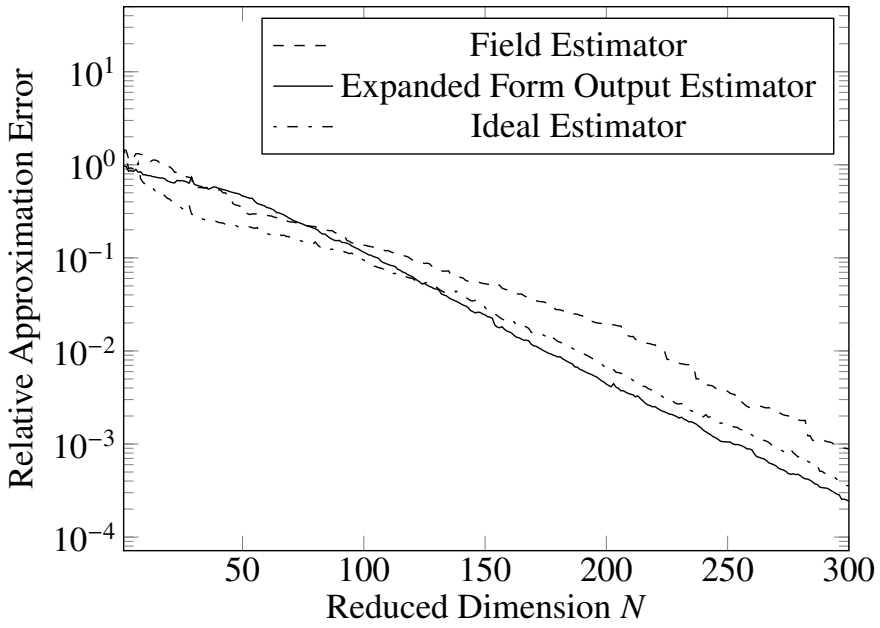

Figure 4.13: Coplanar waveguide: Mean relative error in the output.

4.2 Branchline Coupler

In Fig. 4.14, a branchline coupler model is shown. The striplines, coupled by two transversal bridges are placed on top of a substrate.

4.2.1 Model Description

The full model of the branchline coupler (Fig. 4.14) contains $27'679$ degrees of freedom. In the upper part of the model, the relative permittivity is $\epsilon_r = 1$ while in the lower part, the relative permittivity is $\epsilon_r = 2.2$. The conductivity is zero in the entire domain. The dimensions of the shielded box are 23.6 mm by 22 mm by 7 mm.

Considered parameters are the frequency in $[1.0, 10.0]$ GHz and the relative permeability which varies within $[0.5, 2.0]$, so that the affine expansion contains $Q_a = 2$ terms.

Branchline Coupler Model

Define a bounding box $B_\Omega = [0, 23.6]$ mm $\times [0, 22]$ mm $\times [0, 7]$ mm.
Define the metallic parts
$M_1 = [5.7185, 8.1315]$ mm $\times [0, 22]$ mm $\times [0.744, 0.794]$ mm,
$M_2 = [15.4685, 17.8815]$ mm $\times [0, 22]$ mm $\times [0.744, 0.794]$ mm,
$M_3 = [5.7185, 17.8815]$ mm $\times [5, 7]$ mm $\times [0.744, 0.794]$ mm,
$M_4 = [5.7185, 17.8815]$ mm $\times [15, 17]$ mm $\times [0.744, 0.794]$ mm,
The computational domain is given by $\Omega = B_\Omega \setminus (M_1 \cup M_2 \cup M_3 \cup M_4)$.
It holds (2.26) in Ω, i.e., $-\epsilon\omega^2 E + \nabla \times \frac{1}{\mu} \nabla \times E = -\imath\omega j_i$,
subject to PEC boundary conditions on the metallic parts and the ground plate $E \times n = 0$,
and subject to PMC boundary conditions on the other boundaries $\nabla \times E \times n = 0$.
The material coefficients in the substrate (z $\leq$ 0.744 mm) are given by
$\epsilon = 2.2\epsilon_0, \quad \mu = \mu_0$.
The material coefficients for z $>$ 0.744 mm are given by
$\epsilon = \epsilon_0, \quad \mu = \mu_0$.
The input port is $\Gamma_{in} = 6.925$ mm $\times 1$ mm $\times [0, 0.744]$ mm.
The output port is $\Gamma_{out} = 16.675$ mm $\times 21$ mm $\times [0, 0.744]$ mm.
The source term is $j_i = 1$ on $\Gamma_{in}, \quad j_i = 0$ else.
The output is $l(E) = \int_{\Gamma_{out}} E dz$.

The computational domain is bounded by a shielded box of dimension 23.6 mm by 22 mm by 7 mm. On all boundaries a PEC condition is enforced. The striplines are metallic, so that PEC conditions hold there as well. Thus, the interiors of the metallic striplines are not part of the computational domain. The model is governed by the full time-harmonic Maxwell's equations and as a microwave device, it operates at frequencies of a few GHz.

4.2.2 Numerical Results

Since the branchline coupler model has zero conductivity ($\sigma = 0$) in the entire computational domain, the following computations are performed in real arithmetics. The system matrices are real symmetric for all parameters under consideration, so the transformation (2.80) is not applied. The forcing term $-\imath\omega j_i$ actually leads to purely

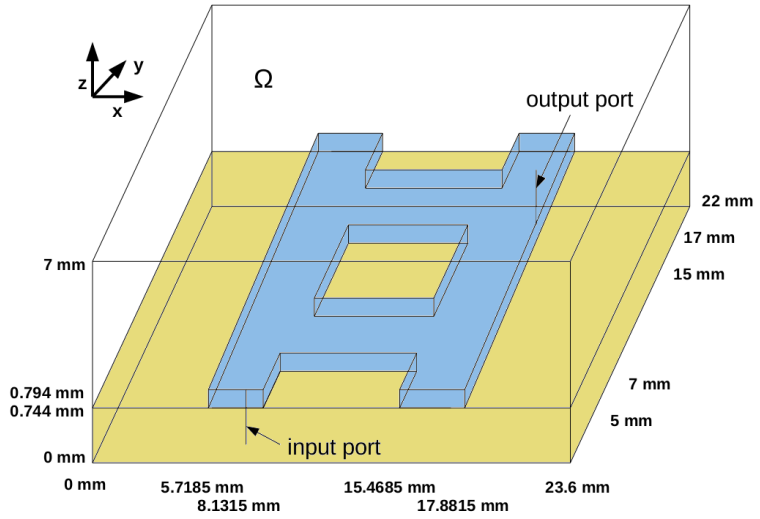

Figure 4.14: Branchline coupler geometry.

imaginary time-harmonic field solutions, but the algorithms produce the same results, whether a real or purely imaginary formulation is used. To simplify implementation, the real field solutions are used.

The transfer functions plotted over the parametric domain for the full order and reduced order model of dimension $N = 25$ are shown in Fig. 4.15 and Fig. 4.16. The relative approximation error between these two transfer functions is shown in Fig. 4.17.

The relative error $\frac{\|E(\nu)-E_N(\nu)\|_X}{\|E(\nu)\|_X}$ and the error estimator for the relative error $\frac{\Delta_N}{\|E_N(\nu)\|_X}$ are plotted in Fig. 4.18 over the reduced basis dimension N. The maximum and the arithmetic mean are computed over all $\nu \in \Xi$ for each RB-dimension N. The sample space Ξ is uniform in both parameters and contains 70 samples in the frequency range $[1.0, 10.0]$ GHz and 80 samples in the material parameter range $[0.5, 2.0]$.

As the branchline coupler model includes several resonances, the error estimator Δ_N might strongly overestimate the absolute error $\|E(\nu) - E_N(\nu)\|_X$ at parameter locations close to resonances. It can thus happen that the greedy algorithm chooses a snapshot location twice, which leads to a 'breakdown' of the offline phase. This can be overcome by either using an estimator for the relative error $\frac{\Delta_N(\nu)}{\|E_N(\nu)\|_X}$ in the greedy sampling or by performing the maximization over $\Xi \backslash S_N$.

Due to the difficulty of properly resolving the resonances, the chosen snapshot

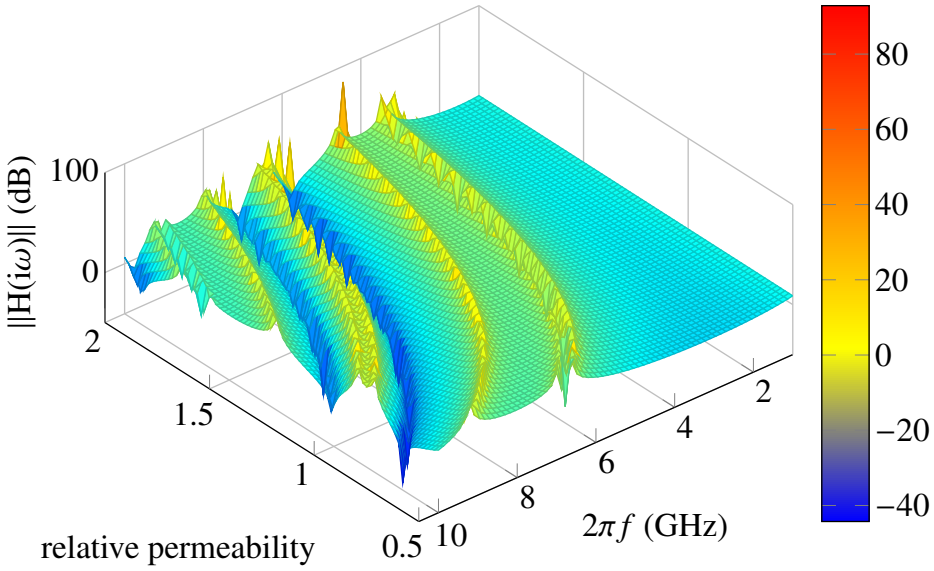

Figure 4.15: Branchline coupler: transfer function of full order model.

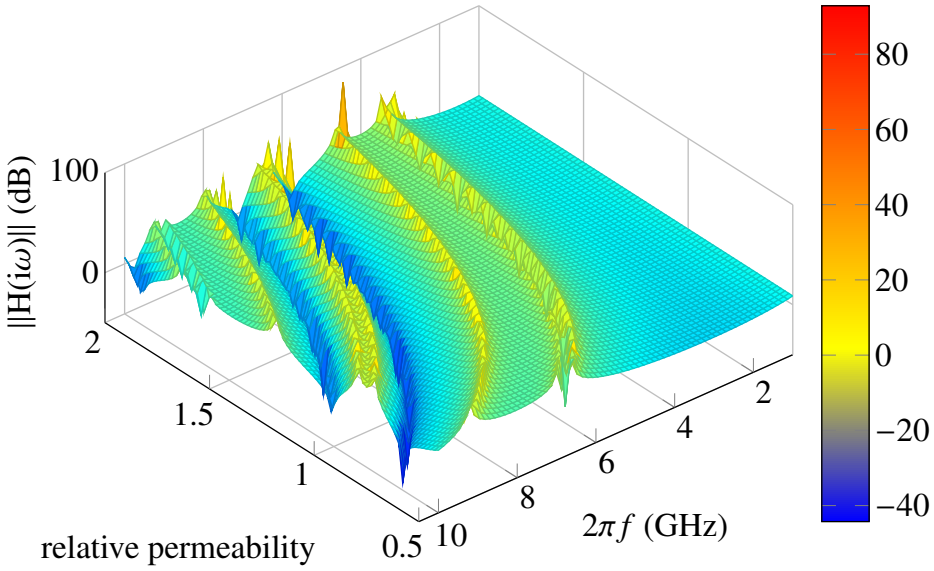

Figure 4.16: Branchline coupler: transfer function of reduced order model of dimension $N = 25$.

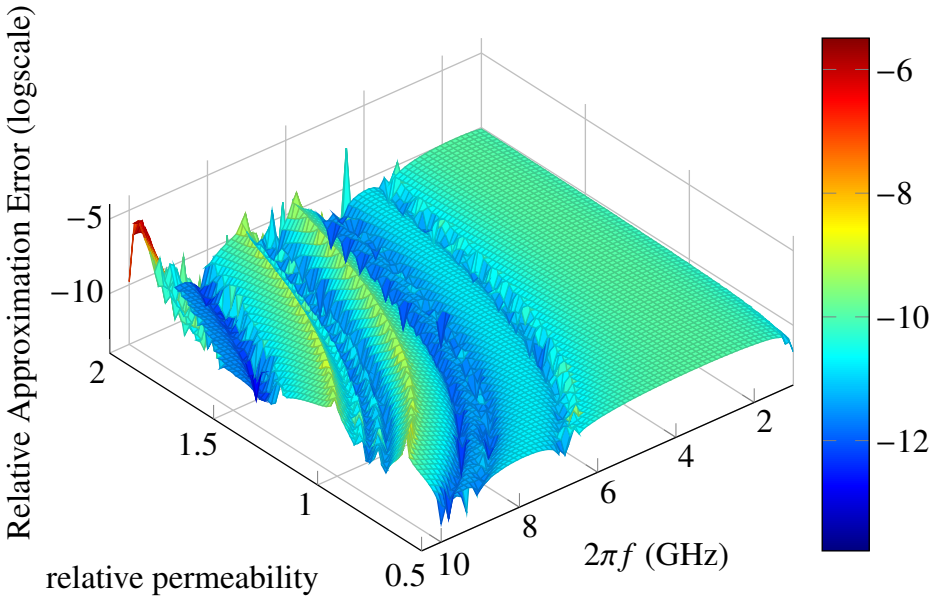

Figure 4.17: Branchline coupler: error between full order and reduced order model for $N = 25$.

locations follow the resonance configurations (Fig. 4.19), as in [CHMR09].

4.2.3 Numerical Aspects Arising from Resonances

As can be observed from Fig. 4.19, the snapshot locations are close to the resonance configurations. The greedy algorithm works correctly in this setting, since the singularities create a large actual error in the vicinity of resonances. The error decay is not as smooth anymore, as can be observed by comparing Fig. 4.8 and Fig. 4.18. Thus, it might be possible, that there exist better reduced order models, which the greedy routine is not able to find.

In particular, an optimization routine within the greedy algorithm to find the maximum would not work in a model with resonances. The optimization routine would come arbitrarily close to a singularity and the greedy algorithm ultimately chooses a parameter location, where the system matrix is singular.

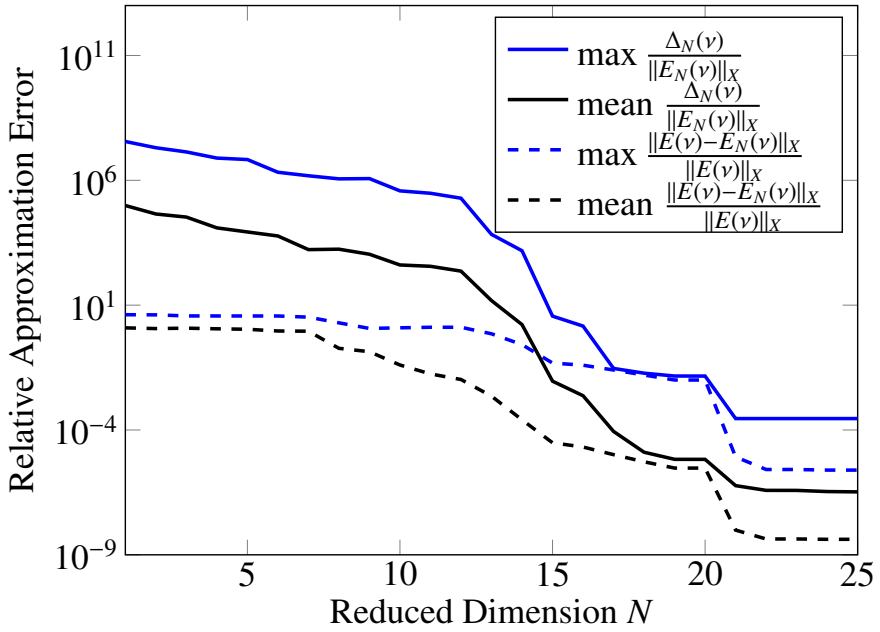

Figure 4.18: Relative error in the field solution plotted over the reduced basis dimension N for the branchline coupler.

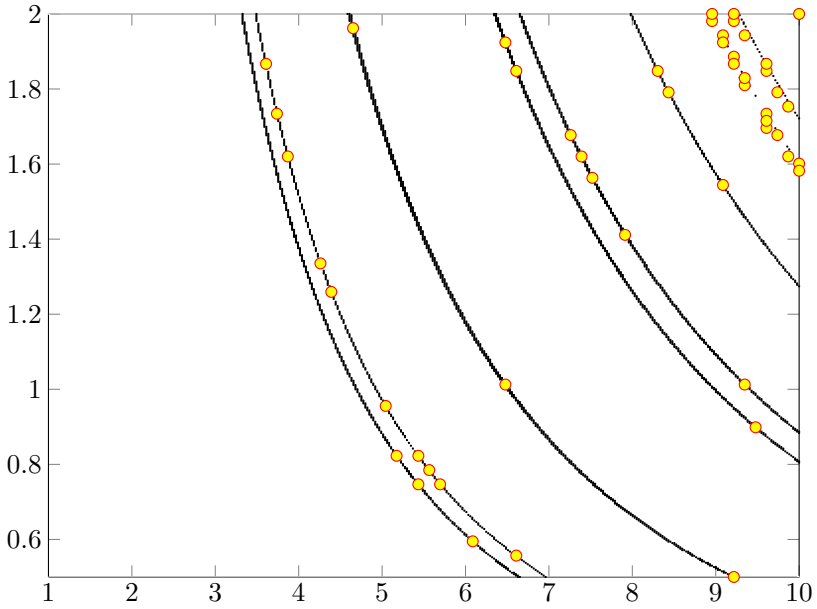

Figure 4.19: Chosen snapshot locations (yellow/red) follow the resonance configurations (black). Shown for $N = 50$.

4.3 Comparison to Surrogate Modeling Techniques

To compare the performance of the RBM with output interpolation techniques, the algorithms contained in the SUrrogate MOdeling Toolbox (SUMO)[5] are run on the same models. For the coplanar waveguide example, the RBM reaches a relative error tolerance of 1% in the transfer function with a model order of 29, the Kriging method provided in the SUMO toolbox requires a model complexity of 55 and the rational interpolation method a model complexity of 63. A more strict error tolerance of 0.1% is reached by the RBM with 41 basis functions, but the output interpolation methods were not able to reach this degree of accuracy up to a model complexity of 200. The branchline coupler example is even more difficult as it contains several resonance configurations. The output interpolation methods were not able to resolve these features.

4.4 Summary of Numerical Experiments

The computational results are summarized in Table 4.1. Using the error estimator, a relative error of less than 1% can be guaranteed at a reduced order of $N = 59$ for the coplanar waveguide, while actually this error is satisfied at an even lower order $N = 47$. Similar findings hold for an error tolerance of 0.1%. For the branchline coupler, these error criteria are satisfied at a reduced order of $N = 21$. The error estimators show a median effectivity of 10 and 7 respectively, i.e. in the median the estimators will overestimate the actual error by these factors. At resonance configurations and at snapshot locations, the error estimator often strongly overestimates the actual error, so that there is a significant difference between the median and arithmetic mean effectivity. The applicability of the RBM might be limited by large offline computation times, as can be seen in the coplanar waveguide example. The larger number of affine terms Q_a leads to the increase in offline computational time for the coplanar waveguide.

The RBM is able to generate low-order models for systems of Maxwell's equations under parametric variation of geometry and frequency with exponential convergence speed. The comparison of Lagrange-RB and Taylor-RB spaces showed that the Lagrange-RB spaces achieve overall better approximation properties. The expanded form leads to a compliant system, which exhibits rapid convergence in the error of the reduced system, comparable to an 'Ideal Greedy'.

[5] The SUMO toolbox[GCC+10] can be obtained from `http://www.sumowiki.intec.ugent.be/index.php/Main_Page`.

Table 4.1: Summary of RBM Performance

	waveguide	**coupler**
Full Model Order	52,134	27,679
$\mathbf{min}\{N \mid \max \frac{\Delta_N(\nu)}{\|E_N(\nu)\|_X} \leq 1\%\}$	59	21
$\mathbf{min}\{N \mid \max \frac{\Delta_N(\nu)}{\|E_N(\nu)\|_X} \leq 0.1\%\}$	83	21
$\mathbf{min}\{N \mid \max \frac{\|E(\nu)-E_N(\nu)\|_X}{\|E(\nu)\|_X} \leq 1\%\}$	47	21
$\mathbf{min}\{N \mid \max \frac{\|E(\nu)-E_N(\nu)\|_X}{\|E(\nu)\|_X} \leq 0.1\%\}$	68	21
Timing Offline Phase	15,809 s	2,275 s
Timing Full Simulation (all $\nu \in \Xi$)	7,930 s	8,644 s
Timing Reduced Simulation (all $\nu \in \Xi$)	10 s (N=85)	1 s (N=25)
Mean Effectivity	11	1537
Median Effectivity	7	10

4.5 Printed Circuit Board

A third example is given by a printed circuit board (Fig. 4.20), discretized with the finite integration technique. While designed as a multi-input, multi-output (MIMO) model, this work only takes a single input and a single output into account to show the capabilities of the reduced basis method. The inputs and outputs are realized as ports, which are single degrees of freedom in the model.

The model makes use of the saddle point form of Maxwell's equations and includes $233'060$ degrees of freedom[6]. Since the modeling and discretization was not part of the work at hand, the model is only briefly summarized in the following. See [Wei77] for an introduction to the finite integration discretization technique.

The saddle point form uses a discretized time-dependent state variable as $x(t) = [E^T(t), H^T(t)]^T$ with discretized electric field $E(t)$ and magnetic field $H(t)$. Discretization of Maxwell's equations leads to a linear time-invariant (LTI) system as

$$\begin{pmatrix} M_\epsilon & 0 \\ 0 & M_\mu \end{pmatrix} \dot{x}(t) = \begin{pmatrix} -M_\sigma & C_H \\ -C_E & 0 \end{pmatrix} x(t) + \mathcal{B}u(t), \tag{4.4}$$

$$y(t) = \mathcal{C}x(t), \tag{4.5}$$

[6]This model was provided through the department of electrical engineering of the Technical University Darmstadt, Germany.

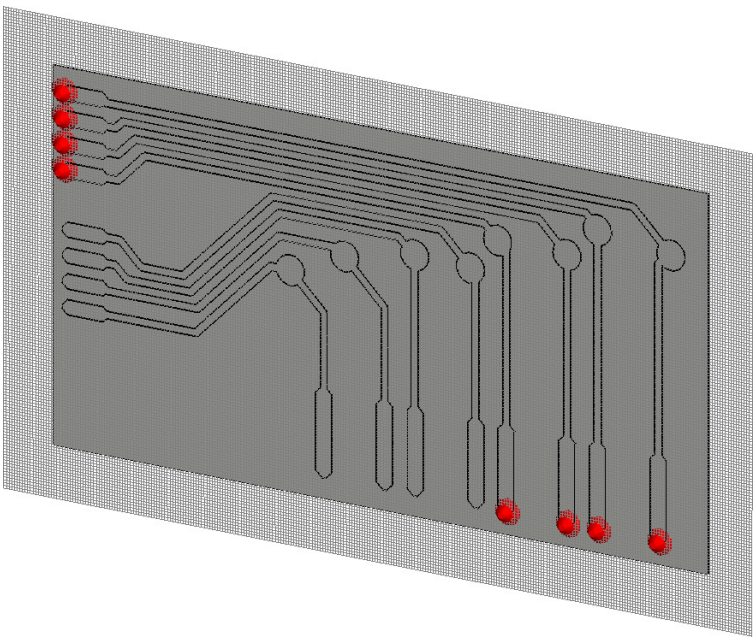

Figure 4.20: Printed circuit board MIMO model.

where M_ϵ, M_μ and M_σ are mass matrices from the discretization of the the material parameters permittivity, permeability and conductivity, respectively. With the finite integration technique, these matrices are diagonal. The matrices C_E and C_H are discrete curl operators for the electric and magnetic field, $u(t)$ is the input and $y(t)$ the output. Further introducing the matrices

$$\mathcal{E} = \begin{pmatrix} M_\epsilon & 0 \\ 0 & M_\mu \end{pmatrix}, \tag{4.6}$$

$$\mathcal{A} = \begin{pmatrix} -M_\sigma & C_H \\ -C_E & 0 \end{pmatrix}, \tag{4.7}$$

and moving to frequency domain leads to

$$\imath\omega\mathcal{E}x = \mathcal{A}x + \mathcal{B}u, \tag{4.8}$$

$$y = \mathcal{C}x. \tag{4.9}$$

In terms of the reduced basis notation, the system matrix depends on the frequency ω as the only parameter as $A^\omega = i\omega\mathcal{E} - \mathcal{A}$. The input functional is $f = \mathcal{B}u$ and the output functional is $s(\omega) = \ell(\omega) = \mathcal{C}x(\omega)$.

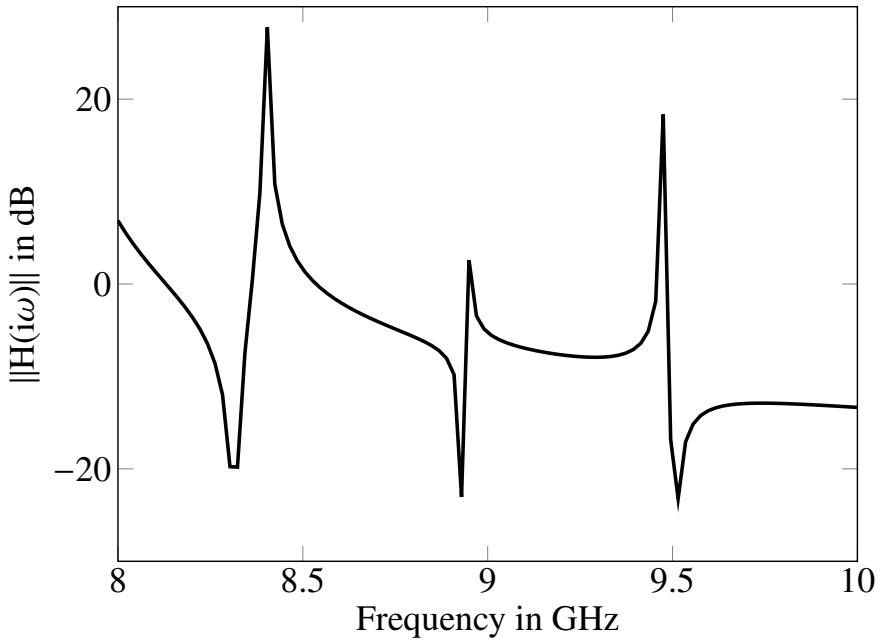

Figure 4.21: Printed circuit board transfer function in $f \in [8, 10]$ GHz with $\omega = 2\pi f$.

The printed circuit board is a lossless model, i.e., $M_\sigma = 0$. As a consequence, the electric field is purely imaginary and the magnetic field is real. Since the output port is associated to a single degree of freedom, no quadratic form arises from the modulus of complex numbers.

Due to the large system size of $233'060$ degrees of freedom, the system is kept in complex form and no transformation to real form such as (2.80) is applied. The estimation of the stability constant is also not applied due to the large system size. Thus, only the residual serves as an error indicator, see [CHMR10] for the efficient implementation in the complex case.

The frequency range $f \in [8, 10]$ GHz with $\omega = 2\pi f$ is sampled with 100 equidistant frequency samples. The corresponding transfer function is shown in Fig. 4.21. The relative error in the output is shown in Fig. 4.22 for three different reduced basis sizes, namely $N = 5, N = 10$ and $N = 15$. The maximum and arithmetic mean of the relative approximation error in the field is shown in Fig. 4.23 and in the output in Fig. 4.24 over each reduced basis dimension. The maximum relative error in the output drops below 1×10^{-3} at a reduced basis dimension of $N = 9$ and below below 1×10^{-6} at a reduced basis dimension of $N = 15$. This is a huge reduction in complexity from the original system size.

While a certified accuracy is not given through error estimators in this example, a heuristic method can still be employed. Either by computing the expensive actual

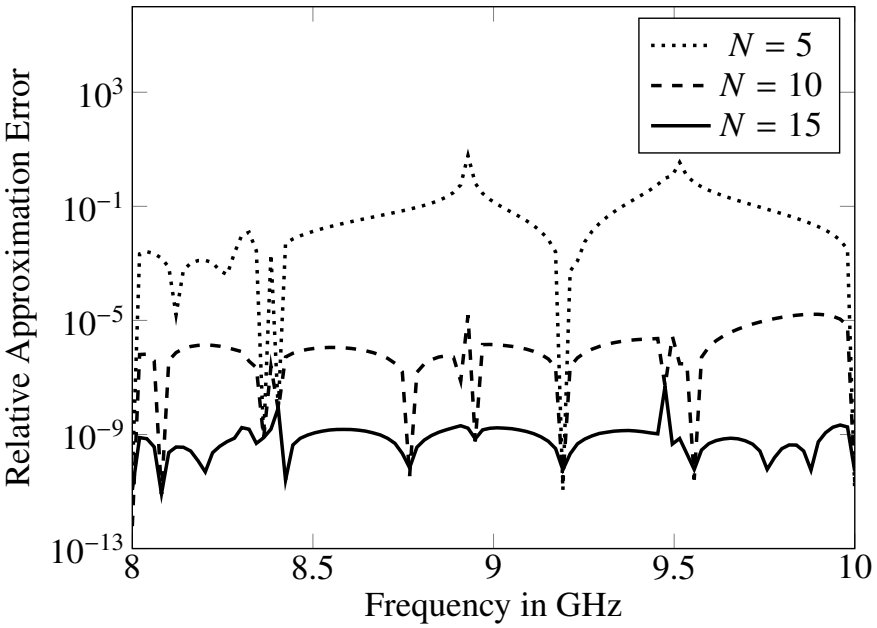

Figure 4.22: Actual relative error in the output plotted for reduced basis dimensions $N = 5, N = 10$ and $N = 15$.

errors at some locations or by solving the related eigenvalue problem to compute a rigorous bound on the error.

4.6 Comparison of Reduced Basis Method to Proper Orthogonal Decomposition and Moment Matching

The reduced basis model reduction is compared with the proper orthogonal decomposition (POD) and moment matching (MM, also known as Padé approximation or Krylov subspace-based MOR) on the printed circuit board model. As with the reduced basis method, the POD and MM are widely used for model reduction purposes, see [SC12], [HC14] concerning the POD and [SWAW09], [BF14] about MM in electromagnetic applications.

4.6.1 Proper Orthogonal Decomposition

The POD computes optimal approximation spaces in the mean-squared error. Given a set of r snapshots as $X = [x_1, \ldots, x_r]$, the POD computes the matrix V of rank N, which best approximates the snapshots in the 2-norm as a minimization over all $V \in \mathbb{R}^{\mathcal{N} \times N}$ with $V^T V = I$,

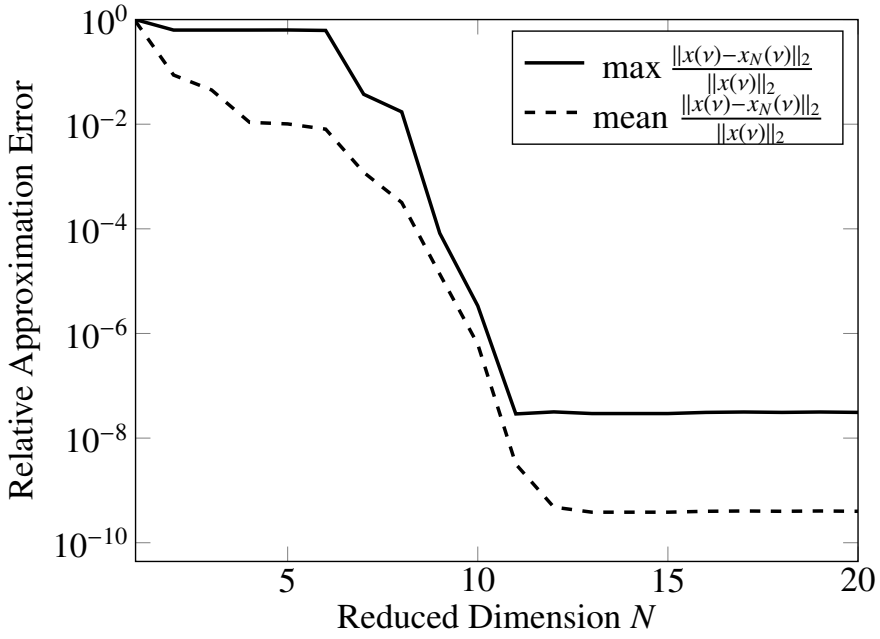

Figure 4.23: Actual relative error in the field plotted over the reduced basis dimension N for the printed circuit board.

$$POD_N(X) = \arg\min_V \frac{1}{r} \sum_{i=1}^{r} \|x_i - VV^T x_i\|_2^2. \tag{4.10}$$

The singular value decomposition (SVD) computes the matrix decomposition $V_1 S V_2^T = X$, where the N leftmost columns of V_1 give the desired matrix V. The columns of the matrix V are also called POD-modes.

In the current example, the snapshots are taken at equidistant locations in the 1-dimensional parameter domain. The matrix V is employed in a one-sided projection of the system to obtain the reduced order model.

4.6.2 Moment Matching

The approach presented here follows the numerically robust, implicit moment matching implementation from [BF14]. From (4.8) with $s = i\omega$, it follows

$$(s\mathcal{E} - \mathcal{A})x = \mathcal{B}u. \tag{4.11}$$

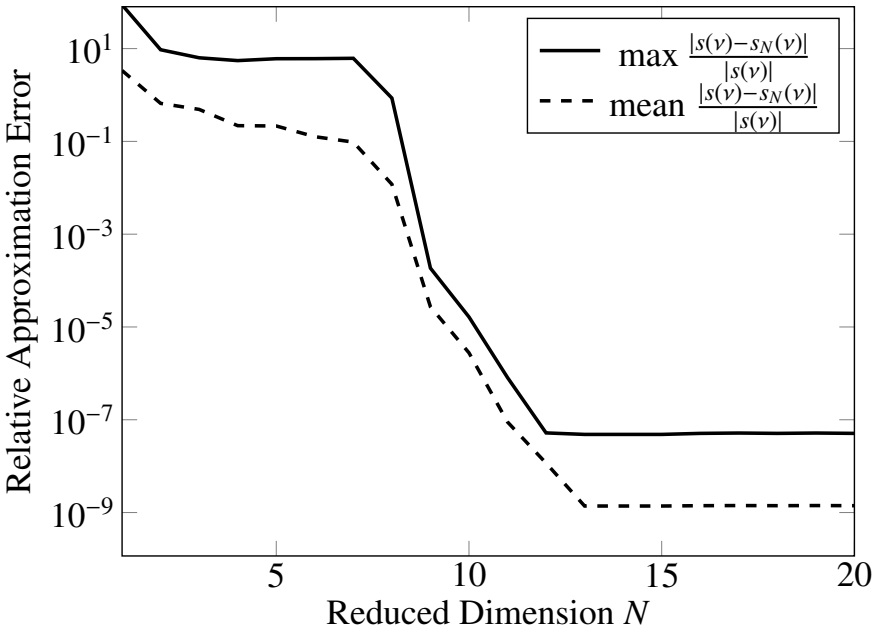

Figure 4.24: Actual relative error in the output plotted over the reduced basis dimension N for the printed circuit board.

Expanding the state around a point $\widetilde{s}_0$ leads to

$$x = (I - \sigma M)^{-1}\widetilde{E}^{-1}\mathcal{B}u \tag{4.12}$$

$$= \sum_{m=0}^{\infty}(\sigma M)^m B_M u \tag{4.13}$$

$$= B_M u + \sigma M B_M u + (\sigma M)^2 B_M u + \ldots + (\sigma M)^j B_M u + \ldots \tag{4.14}$$

with $\sigma = s - \widetilde{s}_0$, $\widetilde{E} = \widetilde{s}_0\mathcal{E} - \mathcal{A}$, $M = -\widetilde{E}^{-1}\mathcal{E}$ and $B_M = \widetilde{E}^{-1}\mathcal{B}$.

Define $R_0 = B_M$ and $R_j = MR_{j-1}, j = 1, 2, \ldots$, and consider the subspace $R = \text{span}\{R_0, \ldots, R_j, \ldots, R_m\}$. The projection space V is derived as an orthonormal basis of R, making use of the recursive relations between the R_j. See [BF14] for details.

With this choice of the one-sided projection space V, the moment matching property up to order m is achieved, i.e., the transfer function of the full and reduced order model match up to the m-th derivative at the expansion point

$$\frac{\partial^j}{\partial\widetilde{s}_0^j}y(\widetilde{s}_0) = \frac{\partial^j}{\partial\widetilde{s}_0^j}y_N(\widetilde{s}_0), \quad j = 0, \ldots, m. \tag{4.15}$$

This process is repeated for equidistantly chosen sample points in the 1-dimensional parameter domain to derive a compound projection space V. For each expansion point, the main computational effort lies in the LU-decomposition of the matrix $\widetilde{E}$, such that no further linear system solves are necessary. There is a relation to the reduced basis Taylor spaces, which also take derivatives of the snapshots with respect to parameters into account. Both projection spaces span the same space as the R_j are the derivatives of the state with respect to the parameter. However, the computational procedure is more robust in the moment matching case, when comparing numerical results with subsection 4.1.3.

4.6.3 Numerical Results

The numerical comparison uses the model setup of the printed circuit board, see section 4.5, where the reduced basis results can also be found.

The POD typically takes only a fraction of the POD-modes into account, corresponding to a certain percentage of the singular values. This truncation was not used here, on the one hand to have control on the resulting reduced model sizes, and on the other hand to show the maximum attainable accuracy from this approach. With equidistantly chosen samples for each POD-reduced model, the projection spaces are not hierarchical.

The MM also uses equidistantly chosen samples as expansion points and are thus not hierarchical. The moments were computed up to second order, so that at each expansion point, three vectors are added to the projection space.

In 4.25 and 4.26, the comparison of the methods in the mean and maximum approximation error over the reduced model order is shown. The RBM and POD have been computed up to an order of 20 and the MM uses 10 expansion points, resulting in a maximum reduced model size of 30. For this model, all three methods show essentially the same approximation quality up to order 12 or a mean error of 1×10^{-9} and maximum error of 1×10^{-7}. A difference is visible in the maximum attainable accuracy, where the POD comes to 1×10^{-11} in the mean error over the sampled grid and 1×10^{-10} in the maximum error, while the RBM stalls essentially as the residual is not resolved with the required accuracy to continue automatic basis enrichment.

In 4.27 and 4.28 the mean and maximum approximation error over the computational effort is compared. Computing the LU-decomposition for the expansion points requires approximately the same computational effort as a linear solve for this example and is thus shown on the same scale.

Put into this perspective, the MM shows a superior performance for this model. While the RB and POD require approximately the same computational effort (the SVD does not add to this, since computing the 'economical SVD' with up to 20 vectors is not expensive) for the snapshot computation, the MM saves a factor of three, which for this example directly corresponds to the choice of matching up to

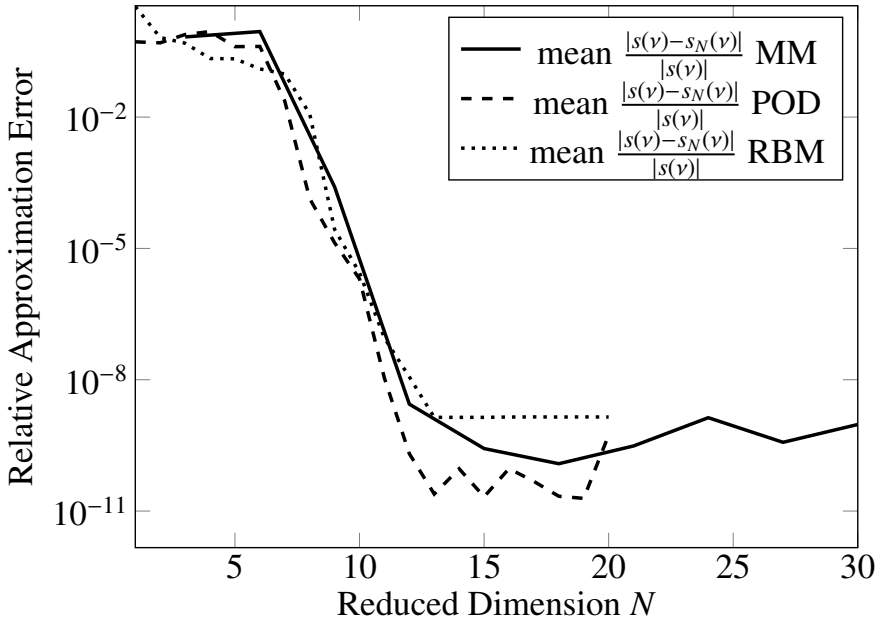

Figure 4.25: Mean relative error in the output plotted over the reduced model dimension N for the printed circuit board.

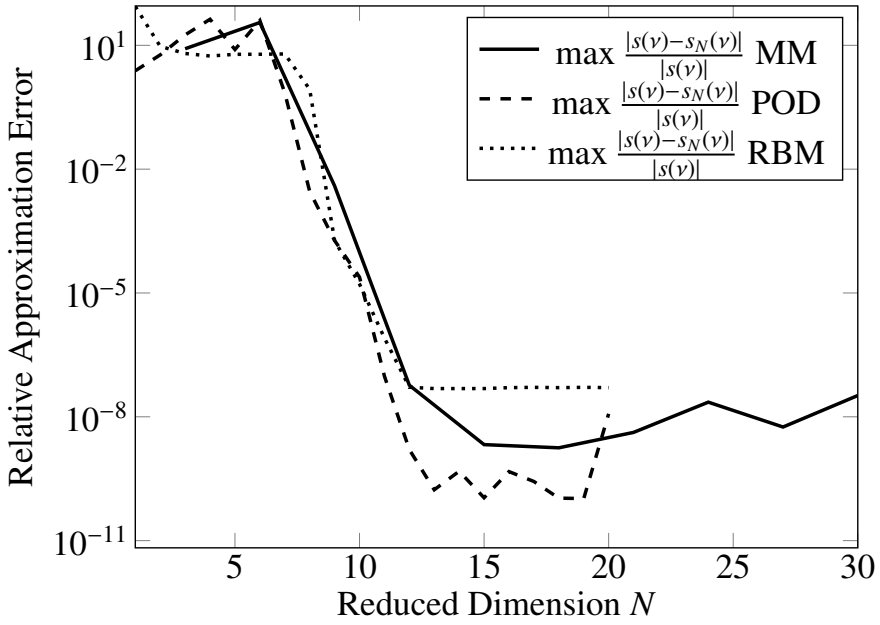

Figure 4.26: Maximum relative error in the output plotted over the reduced basis dimension N for the printed circuit board.

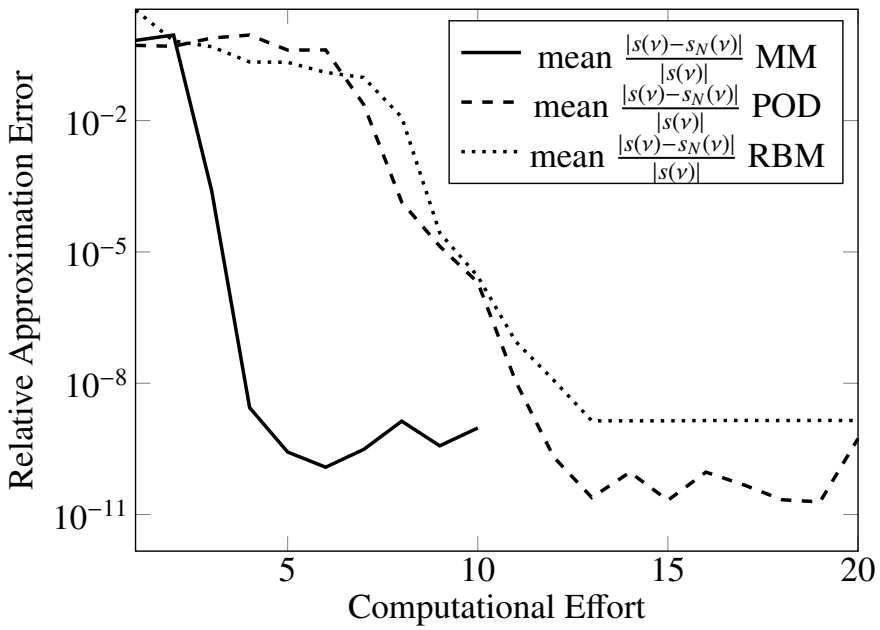

Figure 4.27: Mean relative error in the output plotted over the linear solves/LU decompositions for the printed circuit board.

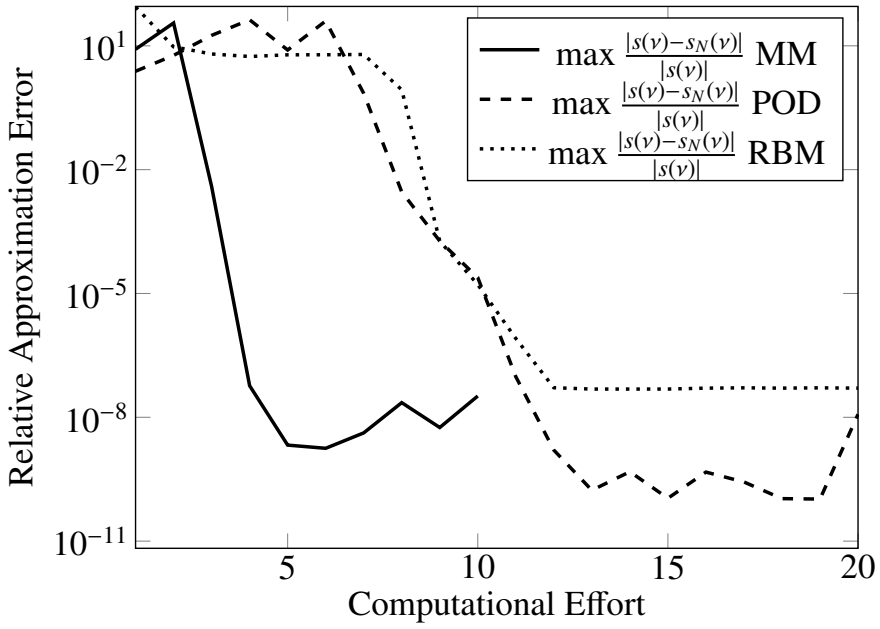

Figure 4.28: Maximum relative error in the output plotted over the linear solves/LU decompositions for the printed circuit board.

the second moment.

The reduced basis methods provides the feature of error estimates to certify the accuracy, however these estimates could in principle also be evaluated for a POD or MM projection matrix, given an affine parameter dependency.

5 Estimating the Inf-Sup Stability Constant

In chapter 4, it is shown that the RBM generates low order models of microscale semiconductor devices under variation of frequency and geometry or material parameters. Thus, the RBM enables the efficient evaluation of parametrized models in many-query and real-time contexts.

This chapter focuses on the efficient estimation of the discrete stability constant, which is a challenging problem in the context of Maxwell's equations. When reliable lower bounds are used in the Reduced Basis error estimation, it enables the generation of reduced order models with certified accuracy. Tests and comparisons of rigorous and non-rigorous techniques to compute lower bounds to the discrete stability constant are shown and compared.

The error estimator measures the accuracy between the full order and reduced order model and is defined by (3.24) as

$$\Delta_N(\nu) = \frac{\|r(\cdot;\nu)\|_{X'}}{\beta_{LB}(\nu)}, \tag{5.1}$$

which involves a lower bound $\beta_{LB}(\nu)$ to the parametrized inf-sup stability constant $\beta(\nu)$, defined by (3.6), as

$$\beta(\nu) = \inf_{u\in X} \sup_{v\in X} \frac{|a(u,v;\nu)|}{\|u\|_X \|v\|_X} \tag{5.2}$$

$$= \inf_{u\in X} \frac{\|a(u,\cdot;\nu)\|_{X'}}{\|u\|_X}. \tag{5.3}$$

Since numerical examples show that the stability constant can vary over several orders of magnitude, the reliability of the error estimator depends on an accurate lower bound. In particular in examples with resonant behavior, the stability constant can vary from zero (resonant parameter configuration) up to 1×10^6.

Of particular interest in the approximation of $\beta(\nu)$ are the stability constants of the reduced order systems for the Galerkin projection

$$\beta_N^G(\nu) = \min_{w\in X_N} \max_{v\in X_N} \frac{|a(w,v;\nu)|}{\|w\|_X \|v\|_X}, \tag{5.4}$$

and the Petrov-Galerkin projection

$$\beta_N^{PG}(\nu) = \min_{w \in X_N} \frac{\|T^\nu w\|_X}{\|w\|_X}, \tag{5.5}$$

obtained from introducing the Riesz representor, or supremizing operator T^ν defined via the relation $(T^\nu w, v)_X = a(w, v; \nu), \forall v \in X$, see the definition in equation (3.8).

5.1 Problem Description

Evaluating the stability constant $\beta(\nu)$ for a parameter configuration ν requires solving the eigenvalue problem (3.13)

$$A^\nu u = \lambda_{\min} M u, \tag{5.6}$$

with system matrix A^ν and inner product matrix M for the eigenvalue of minimum magnitude $\lambda_{\min}$. The computational effort of solving this eigenvalue problem is typically significantly larger than solving the linear system with A^ν. Implementationwise, the MATLAB command *eigs* is used or, for *C++* codes, the Jacobi-Davidson solver from the SLEPC library is used. The task to compute approximations to $\beta(\nu)$ for all $\nu \in \mathcal{D}$ requires multiple eigenvalue solves. For Maxwell's equations, this leads to very large offline timings, as pointed out in [CHMR09]. For this reason, an investigation into approximations of $\beta(\nu)$ instead of rigorous lower bounds is also undertaken in this chapter.

As in the approximation of the transfer function, the idea of using interpolation methods to get approximations of $\beta(\nu)$ seems natural. The Kriging interpolation method is also tested and compared to the estimators which take the structure of the underlying problems into account.

5.2 Successive Constraint Method

The Successive Constraint Method (SCM) outlined here, based on [HRSP07] and [CHMR09], computes lower bounds to the stability constant by solving a linear optimization problem with constraints given by exact solves at chosen parameter configurations. This formulation is possible due to the affine parameter dependence. The parameter configurations for the exact solves are chosen by evaluating lower and upper bounds on the parametrized stability constant, which indicate the currently least well approximated parameter location.

The SCM has a quadratic complexity in the number of terms in the affine expansion Q_a, which can lead to long computation times of the offline phase. A natural norm

SCM, with linear complexity in Q_a is presented in [HKC+10], which also achieves lower bounds to the stability constant, but is algorithmically more involved. A certified natural norm SCM can be found in [Che15], which computes lower and upper bounds to the parametrized stability constant.

Using (3.9), the squared inf-sup constant satisfies

$$(\beta(\nu))^2 = \min_{u \in X} \frac{(T^\nu u, T^\nu u)_X}{\|u\|_X^2}, \tag{5.7}$$

which can be expanded as

$$(\beta(\nu))^2 = \min_{u \in X} \sum_{q'=1}^{Q_a} \sum_{q''=q'}^{Q_a} (2 - \delta_{q'q''}) \Theta^{q'}(\nu) \Theta^{q''}(\nu) \frac{\left(T^{q'} u, T^{q''} u\right)_X}{\|u\|_X^2}.$$

Symmetrizing the problem using elementary properties of the scalar product and defining $Z_{q'}^{q''}(\nu)$ as $Z_{q'}^{q''}(\nu) = \Theta^{q'}(\nu)\Theta^{q''}(\nu)$, it follows

$$\begin{aligned} (\beta(\nu))^2 = \quad & \min_{u \in X} \Bigg(\sum_{q=1}^{Q_a} \left(Z_q^q(\nu) - \sum_{q'=1, q' \neq q}^{Q_a} Z_q^{q'}(\nu) \right) \frac{(T^q u, T^q u)_X}{\|u\|_X^2} \\ & + \sum_{q'=1}^{Q_a} \sum_{q''=q'+1}^{Q_a} Z_{q'}^{q''}(\nu) \frac{\left(T^{q'} u + T^{q''} u, T^{q'} u + T^{q''} u\right)_X}{\|u\|_X^2} \Bigg). \end{aligned} \tag{5.8}$$

Introducing the notation $y_{q',q''}$ for the ν-independent parts of (5.8),

$$y_{q,q}(u) = \frac{(T^q u, T^q u)_X}{\|u\|_X^2}, \tag{5.9}$$

$$y_{q',q''}(u) = \frac{\left(T^{q'} u + T^{q''} u, T^{q'} u + T^{q''} u\right)_X}{\|u\|_X^2}, \quad q'' > q', \tag{5.10}$$

and defining the set $\mathcal{Y}$ as

$$\begin{aligned} \mathcal{Y} = \quad \{ \quad & y = (y_{1,1}, ..., y_{Q_a,Q_a}) \in \mathbb{R}^{\frac{Q_a(Q_a+1)}{2}} | \\ & \exists u \in X \text{ s.t. } y_{q,q} = y_{q,q}(u), y_{q',q''} = y_{q',q''}(u) \}, \end{aligned} \tag{5.11}$$

allows to formulate the stability constant as a minimization problem over $\mathcal{Y}$

$$(\beta(\nu))^2 = \min_{y \in \mathcal{Y}} \mathcal{J}(\nu; y), \tag{5.12}$$

with the objective function

$$\mathcal{J} : \mathcal{D} \times \mathbb{R}^{\frac{Q_a(Q_a+1)}{2}} \to \mathbb{R} \tag{5.13}$$

$$\mathcal{J}(\nu; y) = \sum_{q=1}^{Q_a} \left(Z_q^q(\nu) - \sum_{q'=1, q' \neq q}^{Q_a} Z_q^{q'}(\nu) \right) y_{q,q} + \sum_{q'=1}^{Q_a} \sum_{q''=q'+1}^{Q_a} Z_{q'}^{q''}(\nu) y_{q',q''}.$$

The central idea of the SCM is to define sets $\mathcal{Y}_{LB}$ and $\mathcal{Y}_{UB}$ such that $\mathcal{Y}_{UB} \subset \mathcal{Y} \subset \mathcal{Y}_{LB}$ holds, which implies

$$\min_{y \in \mathcal{Y}_{LB}} \mathcal{J}(\nu, y) \leq \min_{y \in \mathcal{Y}} \mathcal{J}(\nu, y) \leq \min_{y \in \mathcal{Y}_{UB}} \mathcal{J}(\nu, y),$$

such that bounds on the discrete inf-sup constant are given by

$$\begin{aligned} (\beta_{LB}(\nu; C_K))^2 &= \min_{y \in \mathcal{Y}_{LB}(C_K)} \mathcal{J}(\nu, y), \\ (\beta_{UB}(\nu; C_K))^2 &= \min_{y \in \mathcal{Y}_{UB}(C_K)} \mathcal{J}(\nu, y). \end{aligned}$$

Define the continuity constraint Box $\mathcal{B}$ and the constraint sample C_K as

$$\begin{aligned} \mathcal{B} &= \prod_{q'=1}^{Q_a} \prod_{q''=q'}^{Q_a} \left[\min_{w \in X} y_{q',q''}(w), \max_{w \in X} y_{q',q''}(w) \right], \\ C_K &= \{\nu_1, ..., \nu_K\} \subset \Xi. \end{aligned}$$

The lower bound and upper bound sets are defined as

$$\begin{aligned} \mathcal{Y}_{LB}(C_K) = \{ y \in \mathcal{B} | \mathcal{J}(\nu', y) \geq \beta(\nu') \quad \forall \nu' \in C_K, \\ \mathcal{J}(\nu', y) \geq \beta_{LB}(\nu'; C_{K-1}) \quad \forall \nu' \in \Xi \backslash C_K \}, \end{aligned}$$

$$\mathcal{Y}_{UB}(C_K) = \{ y^*(\nu_k) | y^*(\nu_k) = \arg\min_{y \in \mathcal{Y}} \mathcal{J}(\nu_k; y), \nu_k \in C_K \}.$$

The lower bound set is motivated by constraining the bounding box $\mathcal{B}$. It holds $\mathcal{Y} \subset \mathcal{B}$, but the bounding box is too large to yield useful bounds. When the discrete inf-sup constant is solved at parameter locations C_K, then each condition $\mathcal{J}(\nu', y) \geq \beta(\nu')$ constrains the set $\mathcal{B}$. Geometrically, the $\frac{Q_a(Q_a+1)}{2}$-dimensional set $\mathcal{B}$ is constrained by a hyperplane which touches $\mathcal{Y}$ at the minimizer of ν'. The second condition $\mathcal{J}(\nu', y) \geq \beta_{LB}(\nu'; C_{K-1})$ is introduced to ensure monotonically increasing lower bounds with growing k. This leads to a linear program with $\frac{Q_a(Q_a+1)}{2}$ design variables and $Q_a(Q_a+1) + |\Xi|$ inequality constraints. The upper bound set is the discrete set of minimizers at parameter locations C_K.

Algorithm 3 summarizes the SCM in pseudocode. The approximation quality can be controlled by the relative error tolerance ϵ_{SCM}. Comparing to Algorithm 1 shows that the SCM is also a greedy procedure.

Algorithm 3: Successive Constraint Method

INPUT: sampled parameter domain Ξ, tolerance ϵ_{SCM}
OUTPUT: lower bounds $\beta_{LB}(\nu)$ and upper bounds $\beta_{UB}(\nu)$ for all $\nu \in \Xi$

set $K = 1$
choose $C_K = \{\nu_K\}$ arbitrarily
compute $\beta(\nu_K)$, i.e., solve (5.6)
while $\max_{\nu \in \Xi} \frac{\beta_{UB}(\nu; C_K) - \beta_{LB}(\nu; C_K)}{\beta_{UB}(\nu; C_K)} \geq \epsilon_{SCM}$ **do**
    set $\nu_{K+1} = \arg\max_{\nu \in \Xi} \frac{\beta_{UB}(\nu; C_K) - \beta_{LB}(\nu; C_K)}{\beta_{UB}(\nu; C_K)}$
    compute $\beta(\nu_{K+1})$, i.e., solve (5.6)
    set $C_{K+1} = C_K \cup \{\nu_{K+1}\}$
    set $K = K + 1$
end while

Numerical Experiments

As an example, consider the coplanar waveguide model (section 4.1) in a fast frequency sweep setting, where the parameter domain $[0.6, 3.0]$ GHz is discretized with $1'000$ uniformly chosen samples. Fig. 5.1 shows the relative approximation error to the stability constant as the maximum over the sampled parameter domain. Since a lower bound $\beta_{LB}(\nu)$ and an upper bound $\beta_{UB}(\nu)$ to the stability constant is available, the relative approximation error $e_\beta(\nu)$ can be evaluated as

$$e_\beta(\nu) = \frac{|\beta_{UB}(\nu; C_K) - \beta_{LB}(\nu; C_K)|}{|\beta_{UB}(\nu; C_K)|} \tag{5.14}$$

at each SCM iteration K. The maximum remains at 1 for many iterations, since each sample $\nu_i \in C_K$ only improves the lower bounds in a small neighborhood of ν_i. Once

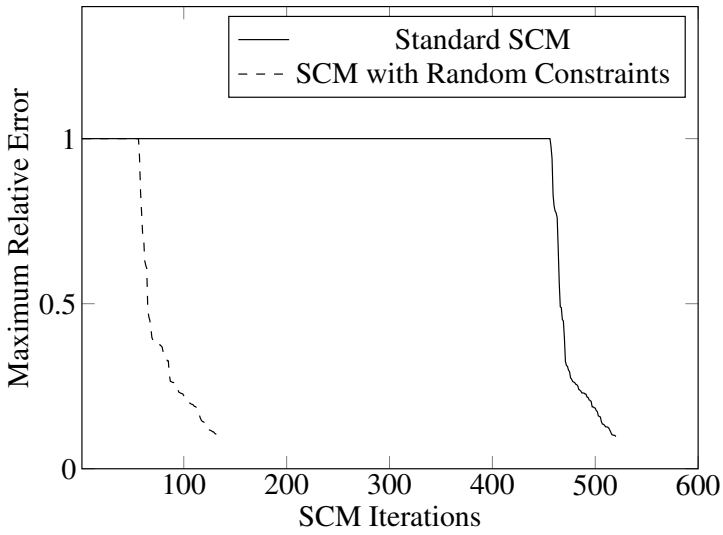

Figure 5.1: SCM relative approximation error to the stability constant. Shown is the maximum error over the sampled parameter domain versus the SCM iteration number.

the parameter domain is explored, the error quickly drops to the desired tolerance of $\epsilon_{SCM} = 0.1$.

It can be computationally beneficial to include randomized constraints in the SCM. This is the case when the main computational effort lies with the linear programs and not the eigenvalue problems. The idea is to sample the scalar coefficient functions $\Theta^q(\nu)$ randomly and independently from each other. This generates additional constraints in the linear program, which can enhance the convergence. Let r denote a vector of Q_a uniformly and independently sampled variables in $[0, 1]$. Let $r(q)$ denote the q-th entry, and define the system matrix corresponding to r as $A^r = \sum_{q=1}^{Q_a} r(q)A^q$ and the stability constant computed from this system matrix is denoted β_r. Further define the objective functional $\mathcal{J}_R(r; y)$ for the random vectors as

$$\mathcal{J}_R(r; y) = \sum_{q=1}^{Q_a} \left(r(q)r(q) - \sum_{q'=1, q' \neq q}^{Q_a} r(q)r(q') \right) y_{q,q} + \sum_{q'=1}^{Q_a} \sum_{q''=q'+1}^{Q_a} r(q')r(q'')y_{q',q''}.$$

Let R_K denote the set of the first K generated random vectors r_k and define the lower bound set

$$\begin{aligned}\mathcal{Y}_{LB}^{R}(C_K, R_K) = \{y \in \mathcal{B} | \mathcal{J}(\nu', y) \geq \beta(\nu') \quad \forall \nu' \in C_K, \\ \mathcal{J}_R(r, y) \geq \beta_r \quad \forall r \in R_K, \\ \mathcal{J}(\nu', y) \geq \beta_{LB}(\nu'; C_{K-1}) \quad \forall \nu' \in \Xi \backslash C_K\},\end{aligned}$$

and the corresponding lower bound on the discrete inf-sup constant is given by

$$(\beta_{LB}^{R}(\nu; C_K, R_K))^2 = \min_{y \in \mathcal{Y}_{LB}^{R}(C_K, R_K)} \mathcal{J}(\nu, y).$$

Then the SCM can be altered to an SCM with random constraints depicted in pseudocode in algorithm 4.

Fig. 5.1 shows this as 'SCM with Random Constraints' where only 138 instead of 520 iterations are necessary. Note however, that with the random constraints, there are two solved eigenproblems in each iteration. One eigenproblem arising from the standard SCM and one with randomized constraints.

Algorithm 4: Successive Constraint Method with Random Constraints

INPUT: sampled parameter domain Ξ, tolerance ϵ_{SCM}
OUTPUT: lower bounds $\beta_{LB}(\nu)$ and upper bounds $\beta_{UB}(\nu)$ for all $\nu \in \Xi$

set $K = 1$
choose $C_K = \{\nu_K\}$ arbitrarily
generate $R_K = \{r_K\}$ by a random number generator
compute $\beta(\nu_K)$, i.e., solve (5.6)
compute β_{r_K}, i.e., solve (5.6)
while $\max_{\nu \in \Xi} \frac{\beta_{UB}(\nu; C_K) - \beta_{LB}^{R}(\nu; C_K, R_K)}{\beta_{UB}(\nu; C_K)} \geq \epsilon_{SCM}$ **do**
    set $\nu_{K+1} = \arg\max_{\nu \in \Xi} \frac{\beta_{UB}(\nu; C_K) - \beta_{LB}^{R}(\nu; C_K, R_K)}{\beta_{UB}(\nu; C_K)}$
    generate r_{K+1} by a random number generator
    compute $\beta(\nu_{K+1})$, i.e., solve (5.6)
    compute $\beta_{r_{K+1}}$, i.e., solve (5.6)
    set $C_{K+1} = C_K \cup \{\nu_{K+1}\}$
    set $R_{K+1} = R_K \cup \{r_{K+1}\}$
    set $K = K + 1$
end while

5.2.1 Successive Constraint Method Variants

The computational time of the SCM benefits from keeping only the currently active constraints from one iteration to the next, see [VHFP11]. This does not influence the

computed bounds. The SCM can be further improved upon with the natural norm SCM (NNSCM), which reduces the complexity from $O(Q_a^2)$ to $O(Q_a)$ [HKC+10]. It is thus applicable to problems with large affine expansions. It generates a decomposition of the parameter domain, where the stability constant in each subdomain is computer with respect to a reference stability constant. The certified natural norm SCM (cNNSCM) [Che15] builds upon the NNSCM, in that it computes rigorous bounds on the stbility constant. These methods promise further computational gains, they are however not implemented in the computational examples.

5.3 Non-Rigorous Estimators

As the computational complexity of the SCM for computation of rigorous error estimators often is too high in the case of Maxwell's equations, we consider estimators $\beta_N(\nu) \approx \beta(\nu)$. In particular, this section uses the upper bounds derived from [HRSP07], and the MinRes, also called Petrov-Galerkin, and Galerkin estimators (method 1 and method 3 from [MPR02]). The Kriging method [Ste99] directly interpolates the function $\beta(\nu)$ and is also applied to the examples for comparison.

5.3.1 Successive Constraint Method Upper Bounds

While the lower bounds generated by the SCM are usually not sharp, the upper bounds are. This motivates a non-rigorous method. In short, upper bounds $\beta_N^{SCM}(\nu) = \beta_{UB}(\nu; C_K)$ are computed for all $\nu \in \Xi$, and applied with a scaling factor $0 < \sigma_{UB} < 1$, as in

$$\Delta_N(\nu) = \frac{\|r(\cdot;\nu)\|_{X'}}{\sigma_{UB}\beta_N^{SCM}(\nu)}.$$

The set C_K is obtained using typical sampling techniques. Here, we used Latin hypercubes (see [Han91]) as sample sets, but numerical examples indicate that a uniform deterministic sampling of the parameter domain yields about the same approximation quality as Latin hypercubes. A typical stopping criterion would be, that when a newly enriched sample space C_K does not significantly improve the upper bounds, the algorithm can stop. Numerical examples suggest, that a choice of σ_{UB} close to one, such as $\sigma_{UB} = 0.9$ is valid in this case.

As in section 5.2, it holds $(\beta(\nu))^2 = \min_{y\in\mathcal{Y}} \mathcal{J}(\nu; y)$ with the objective function $\mathcal{J} : \mathcal{D} \times \mathbb{R}^{\frac{Q(Q+1)}{2}} \to \mathbb{R}$

$$\mathcal{J}(\nu; y) = \sum_{q=1}^{Q} \left(Z_q^q(\nu) - \sum_{q'=1, q'\neq q}^{Q} Z_q^{q'}(\nu) \right) y_{q,q} + \sum_{q'=1}^{Q} \sum_{q''=q'+1}^{Q} Z_{q'}^{q''}(\nu) y_{q',q''}.$$

Constraining the minimization to

$$Y_{UB}(C_K) = \{y^*(\nu_k) | y^*(\nu_k) = \arg\min_{y \in \mathcal{Y}} \mathcal{J}(\nu_k; y), \nu_k \in C_K\},$$

leads to the estimator $(\beta_N^{SCM}(\nu))^2 = \min_{y \in \mathcal{Y}_{\mathcal{UB}}} \mathcal{J}(\nu; y)$, which satisfies $\beta_N^{SCM}(\nu) \geq \beta(\nu)$.

5.3.2 Galerkin Estimator

The Galerkin estimator is obtained when restricting the minimizing as well as maximizing space

$$\beta_N^G(\nu) = \min_{w \in X_N} \max_{v \in X_N} \frac{a(w, v; \nu)}{\|w\|_X \|v\|_X},$$

and is not necessarily an upper or lower bound to the discrete stability constant $\beta(\nu)$.

As the trial as well as test space is restricted, the large-scale eigenvalue problem (5.6) is projected onto X_N, i.e. solve for each parameter

$$X_N^T A^\nu X_N x = \lambda_{\min} X_N^T M X_N x \tag{5.15}$$

for the eigenvalue of minimum magnitude, which then serves as an estimate to the stability constant.

Alternatively, an estimator can be derived by solving

$$X_N^T M^{-1} A^\nu X_N x = \lambda_{\min} x \tag{5.16}$$

for the eigenvalue of minimum magnitude. In the section on numerical results, using this approximation will be briefly discussed.

Similar to the sampling of the field solution, the choice of the projection space X_N is driven by the idea, that the eigenvectors at certain parameter locations $\chi(\nu_i)$ provide a good approximation space. In [MPR02], it is shown that using the $\chi(\nu_i)$ gives arbitrarily good approximations with increasing sample size. Intuitively, this becomes clear when considering that the projected system is supposed to approximate eigenvectors $\chi(\nu)$ for $\nu \in \Xi$. Adding the field solutions $E(\nu_i)$, the space X_N^G is defined as

$$X_N^G = \{\chi(\nu_i) | i = 1, \ldots, N\} \cup \{E(\nu_i) | i = 1, \ldots, N\}, \tag{5.17}$$

and X_N is set as a rectangular matrix of an orthonormalized basis of the space X_N^G.

The parameter domain is sampled using Latin hypercubes (see [Han91]) with samples ν_i, from which X_N^G is derived. The estimator $\beta_N^G(\nu)$ is then evaluated for all parameters of interest.

5.3.3 MinRes Estimator

An upper bound estimator can be derived by restricting the minimizing space to a subset $X_N \subset X$ and define the MinRes estimator $\beta_N^{PG}(\nu)$

$$\beta_N^{PG}(\nu) := \min_{w \in X_N} \frac{\|T^\nu w\|_X}{\|w\|_X} \geq \min_{w \in X} \frac{\|T^\nu w\|_X}{\|w\|_X} = \beta(\nu). \tag{5.18}$$

This estimator is termed MinRes estimator in [MPR02]. In particular, this ansatz corresponds to the stability constant of the reduced Petrov-Galerkin system, introduced in section 3.3.1. As in (5.17), choose

$$X_N^{PG} = \{\chi(\nu_i) | i = 1 \dots N\} \cup \{E(\nu_i) | i = 1 \dots N\}, \tag{5.19}$$

where $\chi(\nu_i)$ is the eigenvector corresponding to $\beta(\nu_i)$. Let X_N denote a rectangular matrix of an orthonormalized basis of the space X_N^{PG} and solve the generalized eigenvalue problem

$$X_N^T (A^\nu)^T M^{-1} A^\nu X_N x = \lambda_{\min} X_N^T M X_N x, \tag{5.20}$$

for the eigenvalue of minimum magnitude. This is a dense, generalized eigenvalue problem but only of small size, since the large and sparse matrices are projected. Taking the squared stability constant shows

$$\begin{aligned} \left(\beta_N^{PG}(\nu)\right)^2 &= \min_{w \in X_N} \frac{(T^\nu w, T^\nu w)_X}{(w, w)_X} \\ &= \min_{w \in X_N} \frac{w^T (T^\nu)^T M T^\nu w}{w^T M w} \\ &= \min_{w \in X_N} \frac{w^T (A^\nu)^T M^{-1} A^\nu w}{w^T M w}, \end{aligned}$$

using $T^\nu = M^{-1} A^\nu$. Thus, the solution of (5.20) solves the minimization problem.

As $\beta_N^{PG}(\nu)$ is an upper bound to the discrete stability constant, it can be applied as in

$$\Delta_N(\nu) = \frac{\|r(\cdot;\nu)\|_{X'}}{\sigma_{UB}\beta_N^{PG}(\nu)}, \tag{5.21}$$

with $0 < \sigma_{UB} < 1$. However, numerical results indicate that the upper bounds of the MinRes estimator are tight and allow for a choice of σ_{UB} close to one.

5.3.4 Kriging Interpolation Method

As a technique for interpolating functions depending on several parameters Kriging is often used. Even though it was originally used to approximate functions that have a non-deterministic character, it has become popular in computational science and engineering applications in general, to create metamodels of black box functions, that are expensive to evaluate. It typically gives better results than polynomial approximation. This subsection describes the basic idea, see [LNS02] or [Ste99] for a more detailed analysis.

Assume given parameter locations $\nu_1, \ldots, \nu_n$ and the observation vector $B = [\ldots, \beta(\nu_i), \ldots]^T$. The aim is to create an interpolant (metamodel) $\widehat{\beta}$. In this setup, it is assumed that β as well as its estimator $\widehat{\beta}$ are random fields and that $\widehat{\beta}$ is a linear combination of the given observations:

$$\widehat{\beta}(\nu) = \sum_{i=1}^{n} \lambda_i(\nu)\beta(\nu_i) \tag{5.22}$$

such that the variance $\mathrm{Var}[\widehat{\beta} - \beta]$ is minimized under the constraint that the expected value $E[\widehat{\beta} - \beta] = 0$. A linear regression model is used in this chapter, which means that the random variable $X(\nu) = \beta(\nu) - \sum_0^2 \alpha_i f_i(\nu)$ has zero expected value and a covariance function given by

$$E[X(\nu)X(\mu)] = R(\theta, \nu, \mu), \tag{5.23}$$

where the f_i span the space of linear functions for two parameters. Here, the covariance function is given by a cubic spline and θ is determined during the algorithm to best approximate. For this, the MATLAB® package DACE [LNS02] is used. Another choice is the SUMO toolbox [GCC+10], where comparable results would be expected.

The error is

$$\begin{aligned}\widehat{\beta}(\nu) - \beta(\nu) &= \sum_{i=1}^{n} \lambda_i(\nu)\beta(\nu_i) - \beta(\nu) \\ &= \sum_{i=1}^{n} \lambda_i(\nu)(\sum_{k=0}^{2} \alpha_k f_k(\nu_i) + X(\nu_i)) - (\sum_{k=0}^{2} \alpha_k f_k(\nu) + X(\nu)) \\ &= \sum_{i=1}^{n} \lambda_i(\nu)X(\nu_i) - X(\nu) + \sum_{k=0}^{2} \alpha_k (\sum_{i=1}^{n} \lambda_i(\nu) f_k(\nu_i) - f_k(\nu)) \end{aligned} \tag{5.24}$$

For an unbiased predictor, demand that $\sum_{i=1}^{n} \lambda_i(\nu) f_k(\nu_i) = f_k(\nu)$, such that the mean squared error of the predictor (5.22) is

$$\begin{aligned} E[(\widehat{\beta}(\nu) - \beta(\nu))^2)] &= E[(\sum_{i=1}^{n} \lambda_i(\nu)X(\nu_i) - X(\nu))^2] \\ &= E[(X^2(\nu) + \sum_{i=1}^{n}\sum_{k=1}^{n} \lambda_i(\nu)\lambda_k(\nu)X(\nu_i)X(\nu_k) \\ &\quad - 2\sum_{k=1}^{n} \lambda_i(\nu)X(\nu_i)X(\nu))] \\ &= 1 + \sum_{i=1}^{n}\sum_{k=1}^{n} \lambda_i(\nu)\lambda_k(\nu)R(\theta,\nu_i,\nu_k) - 2\sum_{k=1}^{n} \lambda_i(\nu)R(\theta,\nu_i,\nu), \end{aligned} \tag{5.25}$$

with Lagrange function using Lagrange multiplier μ

$$\begin{aligned} \mathcal{L}(\lambda,\mu) =& 1 + \sum_{i=1}^{n}\sum_{k=1}^{n} \lambda_i(\nu)\lambda_k(\nu)R(\theta,\nu_i,\nu_k) \\ &- 2\sum_{k=1}^{n} \lambda_i(\nu)R(\theta,\nu_i,\nu) - \mu(\sum_{i=1}^{n} \lambda_i(\nu)f_k(\nu_i) - f_k(\nu)). \end{aligned} \tag{5.26}$$

Imposing necessary optimality conditions using the notation $R_{ij} = R(\theta,\nu_i,\nu_j)$ for entries of the matrix R, $\lambda = \sum_{i=1}^{n} \lambda_i(\nu)$, $r = [R(\theta,\nu_1,\nu),\ldots,R(\theta,\nu_n,\nu)]^T$, $f = [f_0(\nu)f_1(\nu)f_2(\nu)]$ and $F = [f(\nu_1)\ldots f(\nu_n)]^T$ leads to the linear system

$$\begin{pmatrix} R & F \\ F^T & 0 \end{pmatrix} \begin{pmatrix} \lambda \\ \widetilde{\mu} \end{pmatrix} = \begin{pmatrix} r \\ f \end{pmatrix}, \tag{5.27}$$

with definition $\widetilde{\mu} = -\frac{\mu}{2}$. The solution is given as

$$\begin{aligned} \widetilde{\mu} &= (F^T R^{-1} F)^{-1} (F^T R^{-1} r - f), \\ \lambda &= R^{-1}(r - F\widetilde{\mu}), \end{aligned} \tag{5.28}$$

and the predictor is

$$\begin{aligned} \widehat{\beta}(\nu) &= (r - F\widetilde{\mu})^T R^{-1} [\beta(\nu_1) \dots \beta(\nu_n)]^T \\ &= r^T R^{-1} [\beta(\nu_1) \dots \beta(\nu_n)]^T \\ &\quad - (F^T R^{-1} r - f)^T (F^T R^{-1} F)^{-1} F^T R^{-1} [\beta(\nu_1) \dots \beta(\nu_n)]^T. \end{aligned} \tag{5.29}$$

The regression problem

$$F[\alpha_0 \alpha_1 \alpha_2]^T \simeq [\beta(\nu_1) \dots \beta(\nu_n)]^T \tag{5.30}$$

has the generalized least squares solution

$$[\alpha_0^\star \alpha_1^\star \alpha_2^\star]^T = (F^T R^{-1} F)^{-1} F^T R^{-1} [\beta(\nu_1) \dots \beta(\nu_n)]^T. \tag{5.31}$$

leading to the predictor

$$\begin{aligned} \widehat{\beta}(\nu) &= r^T R^{-1} [\beta(\nu_1) \dots \beta(\nu_n)]^T - (F^T R^{-1} r - f)^T [\alpha_0^\star \alpha_1^\star \alpha_2^\star]^T \\ &= f^T [\alpha_0^\star \alpha_1^\star \alpha_2^\star]^T + r^T R^{-1} ([\beta(\nu_1) \dots \beta(\nu_n)]^T - F[\alpha_0^\star \alpha_1^\star \alpha_2^\star]^T) \\ &= f(\nu)^T \alpha^\star + r(\nu)^T \gamma^\star, \end{aligned} \tag{5.32}$$

with $\alpha^\star = [\alpha_0^\star \alpha_1^\star \alpha_2^\star]^T$ and $\gamma^\star = R^{-1}([\beta(\nu_1) \dots \beta(\nu_n)]^T - F[\alpha_0^\star \alpha_1^\star \alpha_2^\star]^T)$. This means that the predictor is a radial basis function interpolation with radial basis function given by R with linear detrending [Ste99].

5.3.5 Comparison of Non-Rigorous Estimators

The non-rigorous estimators are compared on two examples. The coplanar waveguide model (section 4.1) as an example of a lossy broadband structure and a 2D antenna as an example of a highly resonant structure.

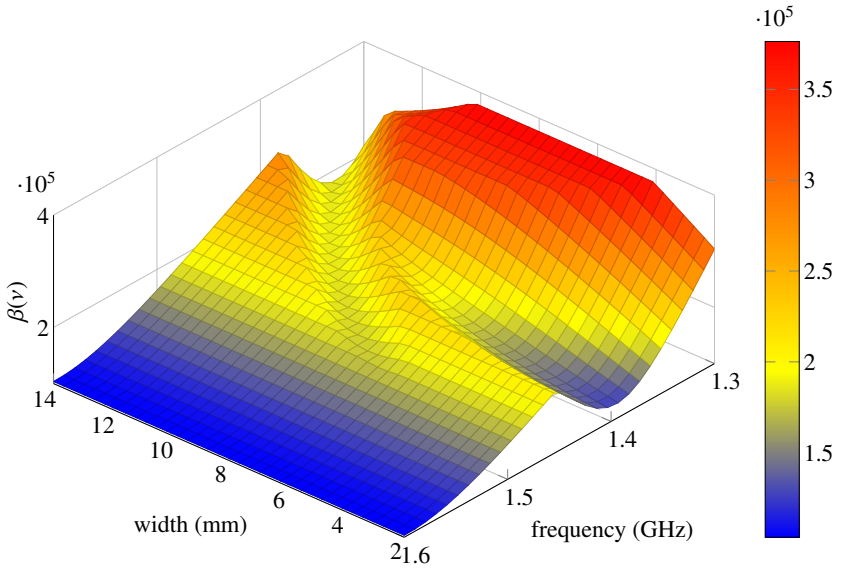

Figure 5.2: Coplanar waveguide: Stability constant plotted over parametric variation of frequency and geometry.

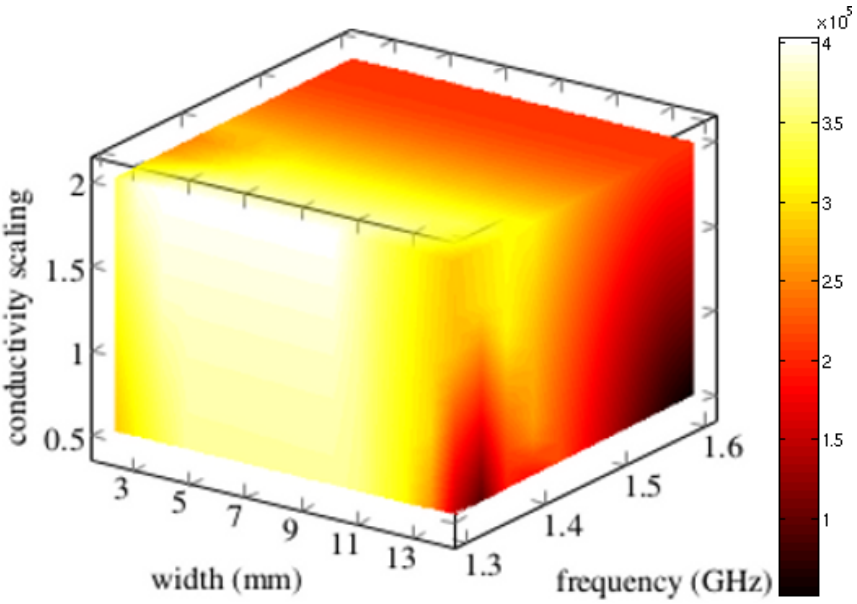

Figure 5.3: Coplanar waveguide: Stability constant plotted over parametric variation of frequency, geometry and conductivity scaling.

Coplanar Waveguide

The coplanar waveguide (section 4.1) is considered with two different parametrizations. The parametric variation of frequency and geometry defines a two-dimensional parameter domain and the additional variation of the conductivity defines a three dimensional parameter domain.

The parametric variation in the frequency is $\omega \in [1.3, 1.6]$ GHz and in the width of the middle strip line it is $p \in [2.0, 14.0]$ mm. In the three parameter model, the conductivity in the lower part additionally varies in $[0.005, 0.02]$ S/m and the conductivity in the upper part varies in $[0.01, 0.04]$ S/m. Both conductivities vary with the same conductivity scaling parameter and it does not have a particular application in mind, but is used formally to investigate the estimators on a three parameter model.

For the coplanar waveguide example, the discrete stability constant $\beta(\nu)$ is shown in Fig. 5.2 under parametric variation of frequency and the width of the middle strip line. Fig. 5.3 shows the three parameter example with additional parametric variation of the conductivity.

The two-dimensional parametric domain is sampled using latin hypercubes and the eigenproblem corresponding to the computation of $\beta(\nu)$ is solved at these parameter locations. As the main computational effort lies in solving the eigenproblems, the number of eigenproblems solved is plotted versus the relative approximation error to compare the approximation quality of the estimators.

The numerical results of the mean error (Fig. 5.4 and Fig. 5.5) and the maximum error (Fig. 5.6 and Fig. 5.7) over a fine grid of the parameter domain show a clear indication for the MinRes estimator. It is the only estimator which resolves the stability constant with a mean error of less than 1%. The SCM upper bounds and the Kriging method also show convergence, but at a lower rate than the MinRes approximation, while the Galerkin estimator does not show convergence and probably requires a significantly larger train set. As the Kriging method is non-intrusive, it can be readily applied to many problems, see [MN14] for the approximation of stability factors in nonlinear PDEs.

The mean and maximum errors are computed by taking the mean/maximum over the relative errors $e_{rel}(\nu) = \frac{|\beta(\nu) - \beta_N(\nu)|}{\beta(\nu)}$ of a sampled grid of dimension 30×35 in the two parameter scenario and $10 \times 10 \times 15$ in the three parameter case. This grid is independent from the Latin hypercube samples used in the training process.

Table 5.1 shows the computation times[1] of the estimators using five precomputed basis vectors (i.e. function evaluations in case of Kriging). The precomputation of the basis vectors took 160s, so this requires the largest portion of computational time. Thus, the computation of the estimators is dominated by evaluating the large-scale discrete stability constant, which is about 1.5 hours to generate the convergence plots.

[1] The computations were done in MATLAB2012b on a Ubuntu 12.04 operating system with an Intel(R) Core(TM)2 Quad CPU Q6700 @ 2.66GHz with 8GB RAM.

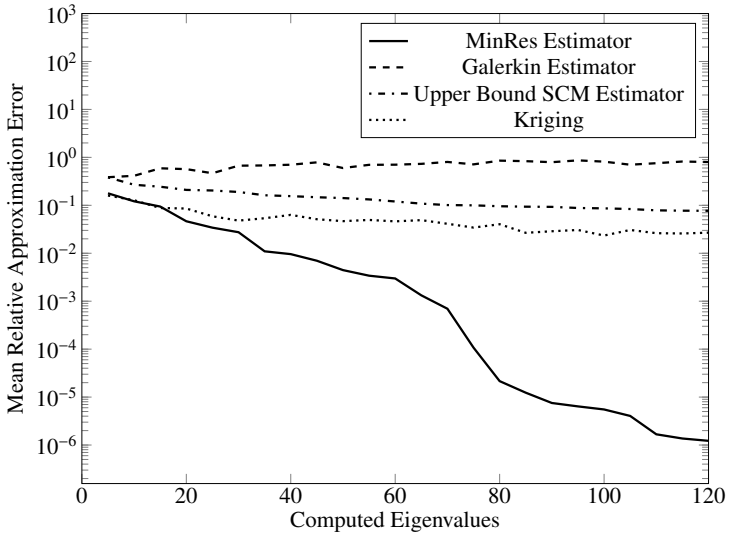

Figure 5.4: Coplanar waveguide: Convergence of mean error over fine reference sample set in the two parameter example. Plotted is the number of eigenproblems solved versus the mean relative approximation error.

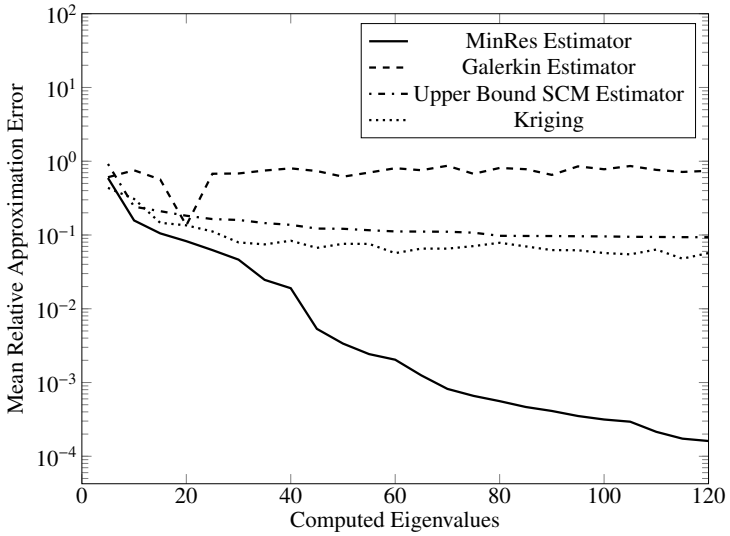

Figure 5.5: Coplanar waveguide: Convergence of mean error over fine reference sample set in the three parameter example. Plotted is the number of eigenproblems solved versus the mean relative approximation error.

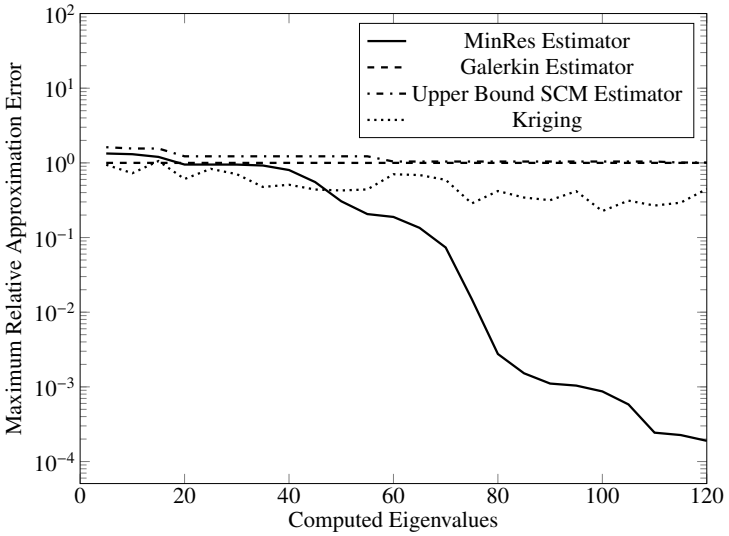

Figure 5.6: Coplanar waveguide: Convergence of maximum error over fine reference sample set in the two parameter example. Plotted is the number of eigenproblems solved versus the maximum relative approximation error.

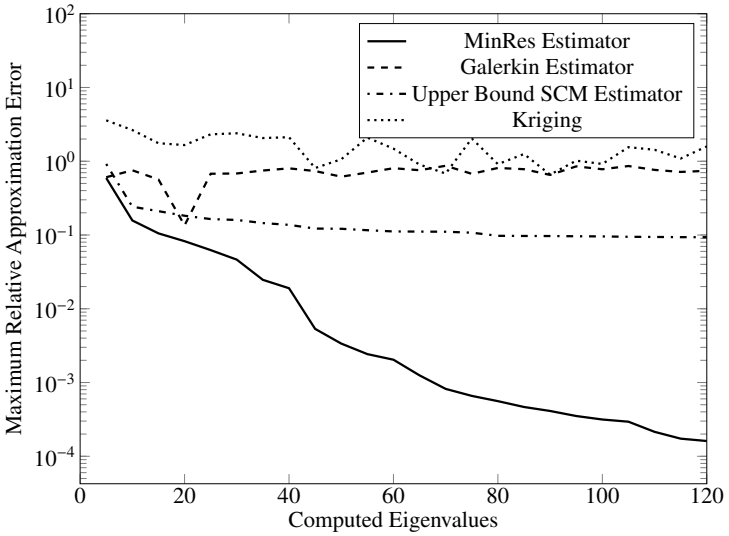

Figure 5.7: Coplanar waveguide: Convergence of maximum error over fine reference sample set in the three parameter example. Plotted is the number of eigenproblems solved versus the maximum relative approximation error.

Table 5.1: Comparison of Timings

Estimator	Computation Time
MinRes	12s
Galerkin	0.6s
SCM upper bounds	30s
Kriging	0.6s

Table 5.2: Improving MinRes

Number of Eigenvectors	mean relative error
1	0.1928
3	0.0152
5	0.0100

Evaluating the Galerkin and Kriging estimators over the sample set has a negligible computational time. Also the SCM upper bounds (30s) and MinRes (12s) have a computational time which is much less than the function evaluations. The SCM bounds take a larger computation time as the evaluation of the objective functional $\mathcal{J}(\nu, y)$ for all $y \in \mathcal{Y}_{UB}$ is expensive. Taking into account the time required for function evaluations however, the computation times of the estimators are comparable for the model under consideration. In our test case a single function evaluation takes 32s, so that adding additional observations in the Kriging for instance does exceed the total computation times of the other estimators.

In Table 5.2, the effect of using eigenvectors corresponding to the three and five smallest eigenvalues is investigated. The aim is to further increase the quality of the MinRes estimator. It uses 15 sample points in the two parameter example and collects the eigenvectors in the projection space X_N. The rationale behind this investigation is that the additional eigenvectors might serve as good approximations to the minimizers at other sample points. The numerical results show a significant improvement of the approximation quality for small increases in the number of eigenvalues. Also note that the computational time does not increase significantly by gathering additional eigenvectors.

The two variants of the Galerkin estimator (5.15) and (5.16) are compared in Table 5.3. Both tend to underestimate the stability constant, which leads to worse approximations when increasing the basis size. They are not effective for the model problem under consideration.

The MinRes estimator clearly manages to resolve the stability constant better

Table 5.3: Comparison of Galerkin variants

No. of Eigenvectors	**mean error** (5.15)	**mean error** (5.16)
120	0.800	0.352
240	0.693	0.440
360	0.812	0.466

than all the other estimators. To use this estimator in a practical setting, a heuristic stopping criterion can be used, in the sense that if newly computed stability constants are already well resolved, the algorithm can stop.

Antenna

As an example of a highly resonant structure, we consider a rod antenna in a 2D unit square. The material coefficients are given by $\mu_r = 1$, $\sigma = 0$ and ϵ_r is set to 1 in one half of the domain Ω_1, while it is a parameter in the other half of the domain Ω_2, satisfying $\epsilon_r \in [2, 6]$. The domain is shown in Fig. 5.8. The discretization has 4880 degrees of freedom and is done with 2D Nédélec finite elements and the boundary is PEC. The source term is applied as a sine wave over the rod Γ. Additionally, we consider a parametric variation in frequency of $\omega \in \left[\frac{3\pi}{2}, \frac{7\pi}{2}\right]$. The values of the stability constant are shown in Fig. 5.9, close to a resonance configuration the stability constant tends to zero. This is a modified version of the model discussed in [CHMR09].

The numerical results of the mean error (Fig. 5.10) and the maximum error (Fig. 5.11) over a fine grid of the parameter domain show a different picture. The difference is that the Galerkin estimator also provides accurate bounds, similar to the MinRes estimator, while the SCM upper bounds and the Kriging do not properly resolve the problem. Note that due to the many resonances, the maximum error remains large as it is difficult to resolve every sample point. The difference between maximum and mean error is three to four orders of magnitude in this example, while it is only about one order of magnitude in the waveguide example.

The mean and maximum errors are computed by taking the mean/maximum over the relative errors $e_{rel}(\nu) = \frac{|\beta(\nu) - \beta_N(\nu)|}{\beta(\nu)}$ of a sampled grid of dimension 170×150. This grid is independent from the Latin hypercube samples used in the training process.

Table 5.4 shows the computation times of the estimators using five precomputed basis vectors (i.e., function evaluations in case of Kriging), in the same way as done in Table 5.1 for the coplanar waveguide example. Since this model is of smaller size, namely 4880 degrees of freedom, the precomputation of the five basis vectors takes only 1 s, so the computational time lies in computing the estimates.

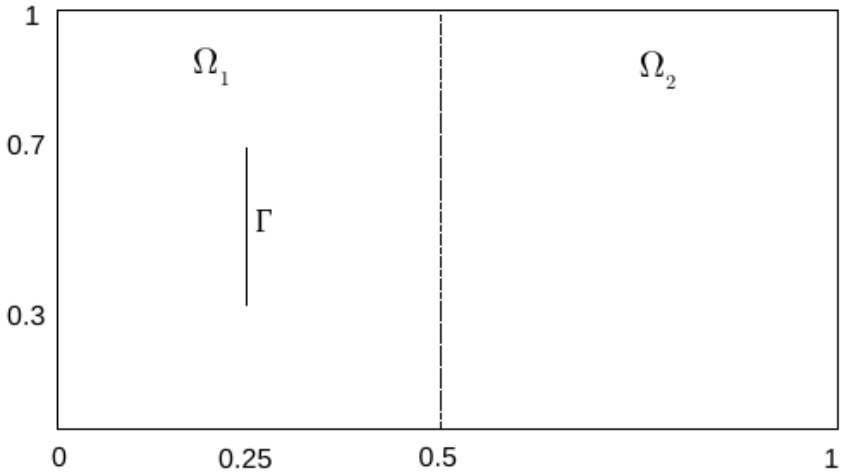

Figure 5.8: Computational domain of the rod antenna.

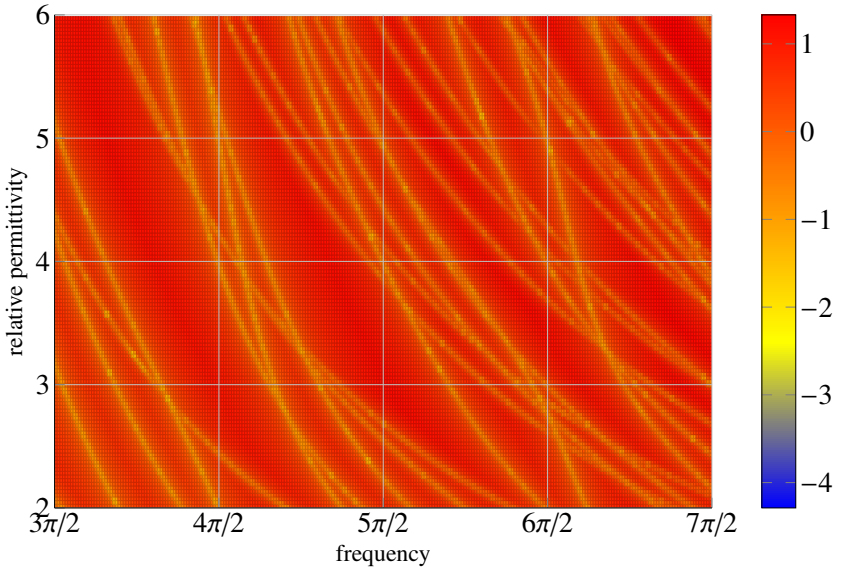

Figure 5.9: Log-plot of the stability constant plotted over parametric variation of frequency and relative permittivity in the antenna model.

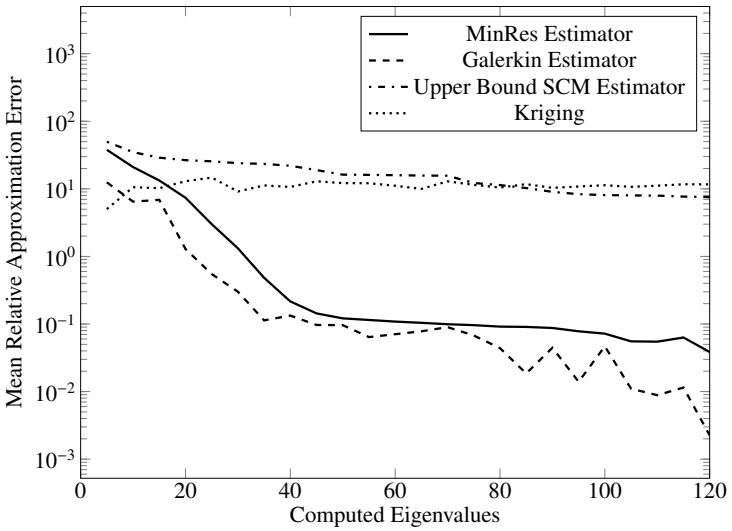

Figure 5.10: Convergence of mean error over fine reference sample set in the antenna example. Plotted is the number of eigenproblems solved versus the mean relative approximation error.

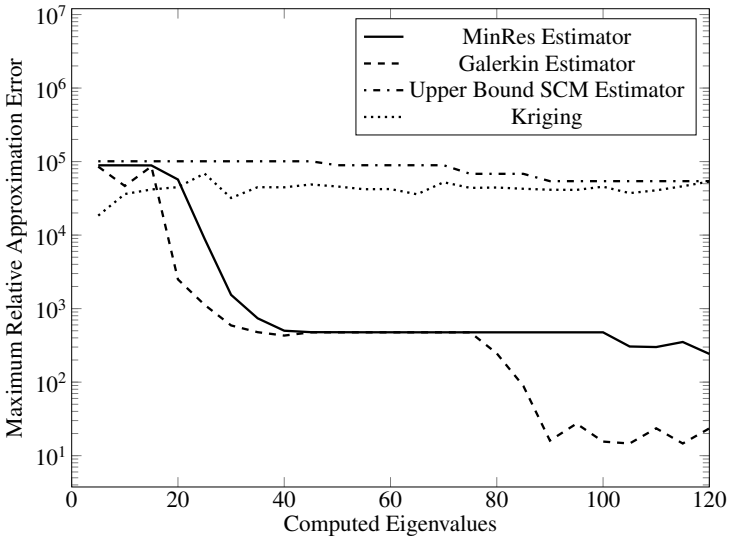

Figure 5.11: Convergence of maximum error over fine reference sample set in the antenna example. Plotted is the number of eigenproblems solved versus the maximum relative approximation error.

Table 5.4: Comparison of Timings excluding eigenvalue computation for the antenna example.

Estimator	Computation Time
MinRes	4 s
Galerkin	1.3 s
SCM upper bounds	3.8 s
Kriging	1.3 s

Evaluating the Galerkin and Kriging estimators over the sample set has a computational time of 1.3 s. The SCM upper bounds take 3.8 s and MinRes estimates 4 s. The ratio between the estimate changes in comparison to the coplanar waveguide example, since not only is the number of degrees of freedom smaller, but also the number of affine terms. Since $Q_a = 3$ for the antenna example is smaller than $Q_a = 15$ in the coplanar waveguide example, the algorithms which have a quadratic dependence on Q_a (i.e., MinRes and SCM upper bounds) perform better.

The computation time of Galerkin and SCM estimators increase in comparison to Table 5.1, since the antenna example uses a finer grid of 170×150 samples. The two parameter coplanar waveguide example uses a grid of 30×35 samples.

5.3.6 Comparison to Residual Based Estimators

We perform a comparison to established residual based estimators, where the stability constant is assumed to be one, i.e., no estimation of the stability constant takes place. The numerical results of the mean error (Fig. 5.12) from a reduced basis size of 55 to 80 show an advantage in model accuracy when using more precise stability constant estimates. For a fixed reduced basis size, the highest accuracy is achieved when using the precise Galerkin and MinRes estimates, while the SCM estimators give an average accuracy and the Kriging and only residual estimates ("no estimates") give the lowest accuracy. The relative error is measured in the L_2 norm of the electric field. The estimators use the stability constant estimates corresponding to 40 solved eigenproblems. Due to the many resonances in the model, the maximum relative error does not fall below 100% for all estimators.

In the coplanar waveguide example, no advantage can be observed when using more accurate estimates, see Fig. 5.13. This might be due to limited parametric variation in the model, such that the heuristic greedy-maximum sampling does not benefit from improved estimates.

The MinRes estimator manages to resolve the stability constant properly in the considered examples. The Galerkin estimator, which is computed faster than the

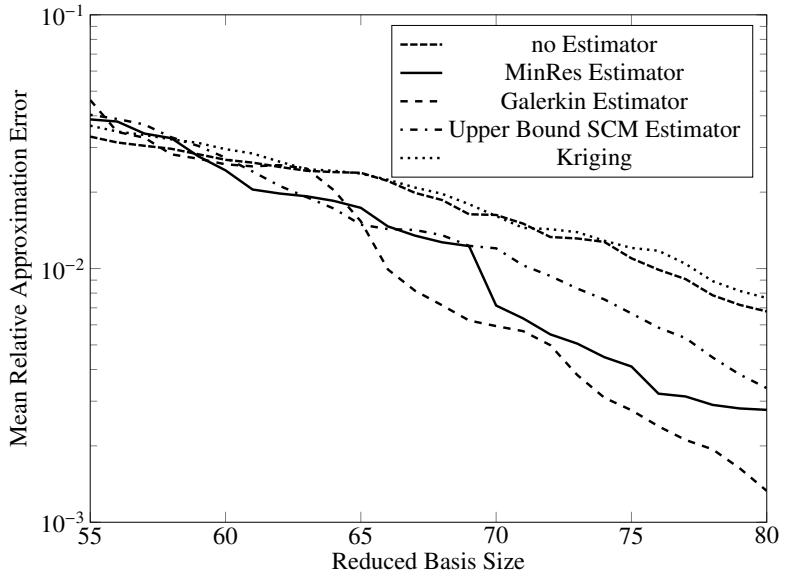

Figure 5.12: Reduced basis size versus the mean relative error in the field solution in the L_2 norm in the antenna example.

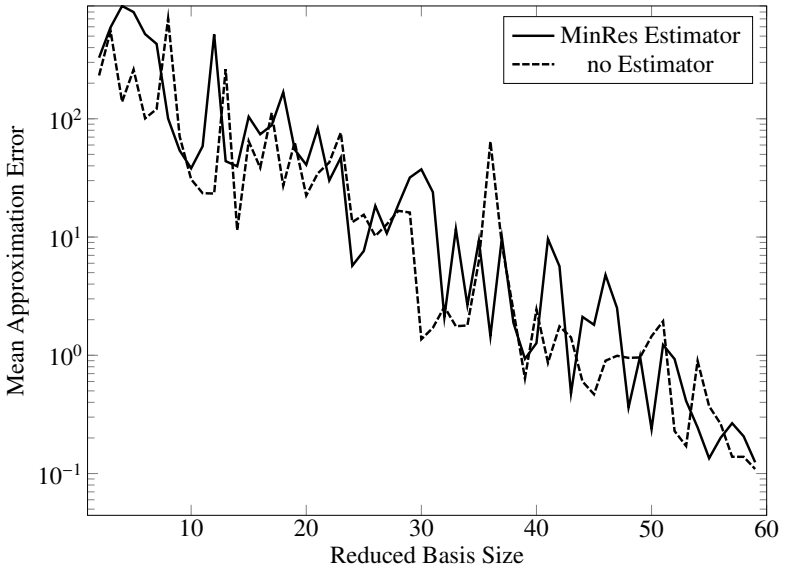

Figure 5.13: Reduced basis size versus the mean error in the field solution in the L_2 norm in the coplanar waveguide example.

MinRes estimator, also resolved the antenna example well. The computational effort of the estimators lies in solving the required eigenproblems. If this computational effort is not prohibitive, model reduction driven by error indicators can benefit from using these improved bounds. An advantage of using precise estimates of the stability constant is that the error estimates are rigorous, i.e., in a resonance model, the algorithm is aware of where the large errors occur, effectively being aware of the resonance locations. To use this estimator in a practical setting, a heuristic stopping criterion can be used, in the sense that if newly computed stability constants are already well resolved, the algorithm can stop. An open question is if and how the estimators can be incorporated into two-level approximation schemes for non-affine parameter dependence such as the one presented in [LMR12].

5.4 Successive Constraint Method with Matrix-Valued Constraints

Since the lower bounds generated by the SCM are not tight, the idea is to further constrain the set $\mathcal{Y}_{LB}$, such that the minimization

$$\alpha_{LB}(\nu) = \min_{y \in \mathcal{Y}_{LB}} \mathcal{J}(\nu, y),$$

yields better bounds on the coercivity constant α or inf-sup constant β, respectively. The technique is outlined here for the coercivity constant and not the inf-sup constant. It is however analogously applicable to the inf-sup constant, but much more technical. Since the obtained numerical results from a Poisson problem did not show a significant improvement, the implementation has not been taken to a level where it is applicable to the inf-sup constant.

To incorporate more data from the bilinear form than just the Rayleigh quotient, the bilinear form is sampled on 2- (or in general p-) dimensional subspaces, thus creating more constraints and effectively a smaller bounding set. This moves the problem from a linear programming problem to a general optimization problem with a concave objective function.

Define analogously to (5.11)

$$\begin{aligned} \mathcal{Y}^{2\times 2} = \{ & y = (Y_1, ..., Y_{Q_a}) | \exists u_1, u_2 \in X \\ & \text{with } u_1 \perp u_2, \|u_1\|_X = 1, \|u_2\|_X = 1, \\ & \text{s.t. } Y_q = \begin{pmatrix} a^q(u_1, u_1) & a^q(u_2, u_1) \\ a^q(u_1, u_2) & a^q(u_2, u_2) \end{pmatrix} \}, \end{aligned} \tag{5.33}$$

and the objective function as

$$\mathcal{J}(\nu; y) = \lambda_{min} \left(\sum_{q=1}^{Q_a} \Theta^q(\nu) Y_q \right). \tag{5.34}$$

The coercivity constant is then characterized by

$$\alpha(\nu) = \min_{y \in \mathcal{Y}^{2\times 2}} \mathcal{J}(\nu; y). \tag{5.35}$$

Define bounding box $\mathcal{B}$

$$\mathcal{B} = \{y = \{Y_1, \ldots, Y_{Q_a}\} | \sigma_q^- \mathbf{I} \leq Y_q \leq \sigma_q^+ \mathbf{I} \quad \forall q = 1, \ldots, Q_a\}, \tag{5.36}$$

where

$$\sigma_q^- = \min_{w \in X} \frac{a^q(w, w)}{\|w\|_X}, \tag{5.37}$$

$$\sigma_q^+ = \max_{w \in X} \frac{a^q(w, w)}{\|w\|_X}, \tag{5.38}$$

and for a constraint set of parameter samples C_K, define

$$\mathcal{Y}_{LB}^{2\times 2}(\mathcal{C}_K) \equiv \{\, y = (Y_1, ..., Y_{Q_a}) \in \mathcal{B} \mid \forall \mu' \in \mathcal{C}_K, \quad \begin{array}{l} \sum_{q=1}^{Q} \Theta_q(\nu') \mathbf{Y}_q \geq \Lambda_1(\nu') \mathbf{I} \quad \text{and} \\ \sum_{q=1}^{Q} \Theta_q(\nu') \mathsf{trace}\,(\mathbf{Y}_q) \geq \Lambda_1(\nu') + \Lambda_2(\nu') \end{array} \right\}.$$

Since $Y \subset Y_{LB}$, a lower bound is given by

$$\alpha_{LB}(\nu) = \min_{y \in \mathcal{Y}_{LB}^{2\times 2}} \mathcal{J}(\nu, y). \tag{5.39}$$

This optimization problem resembles a semidefinite programming problem with the exception of the objective function. Since the objective function minimizes the minimal eigenvalue of a 2×2 matrix, a semidefinite program solver can not be used, since the objective function cannot be cast as a linear functional in this case [VB96]. The use of a general optimization routine is therefore necessary. The computational time is thus greatly increased from the standard SCM, which requires only linear programs. Concludingly, since the experiments gave only minimal improvement in the lower bound (Fig. 5.14), this approach is in its current form not beneficial.

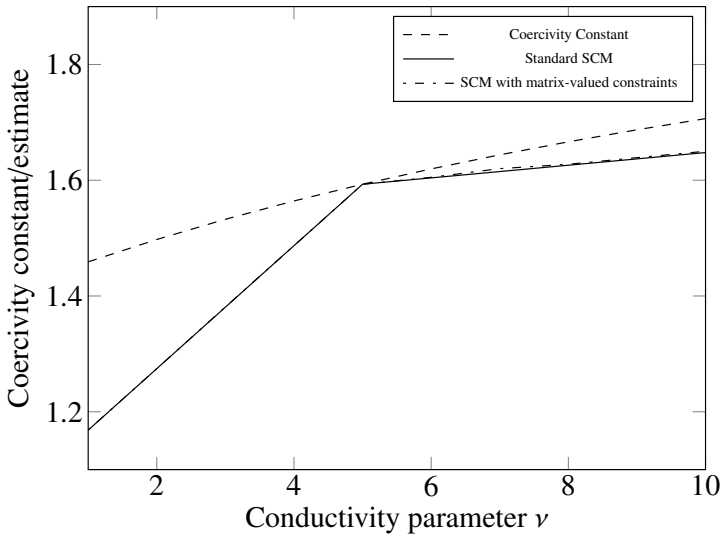

Figure 5.14: Comparison of standard SCM with matrix-valued SCM. The underlying problem is a Poisson problem, see the 'Thermal Block' example in [RHP08].

5.5 Stability Constant of the Expanded system

Numerical tests showed, that the stability constant is not invariant under the transformation to the expanded system (3.58). Nevertheless, the resonance configurations are maintained, i.e., the expanded system matrix $\mathcal{A}^\nu$ (3.60) has a zero eigenvalue if and only if the real, symmetric system matrix A^ν has a zero eigenvalue.

Theorem 5.5.1 (Invariance of Singularities for the Expanded System)**.** *The expanded system matrix $\mathcal{A}^\nu$ (3.60) is singular if and only if the real symmetric system matrix A^ν is singular.*

Proof:
"$\Rightarrow$"

Assume $\mathcal{A}^\nu$ is singular, i.e., there exists a vector $\begin{bmatrix} v_1 \\ v_2 \end{bmatrix}$ with $\mathcal{A}^\nu \begin{bmatrix} v_1 \\ v_2 \end{bmatrix} = \begin{bmatrix} 0 \\ 0 \end{bmatrix}$.

It is:

$$\begin{aligned} \mathcal{A}^\nu \begin{bmatrix} v_1 \\ v_2 \end{bmatrix} &= \begin{bmatrix} 2A^\nu - Q & -Q \\ -Q & -2A^\nu - Q \end{bmatrix} \begin{bmatrix} v_1 \\ v_2 \end{bmatrix} \\ &= \begin{bmatrix} 2A^\nu v_1 - Qv_1 - Qv_2 \\ -Qv_1 - 2A^\nu v_2 - Qv_2 \end{bmatrix}, \end{aligned}$$

so that

$$2A^\nu v_1 = Q(v_1 + v_2), \tag{5.40}$$
$$2A^\nu v_2 = -Q(v_1 + v_2), \tag{5.41}$$

from which follows that $A^\nu(v_1 + v_2) = 0$, i.e., A^ν is singular.

"$\Leftarrow$"

Assume A^ν is singular, i.e., there exists a v such that $A^\nu v = 0$.

It then holds:

$$\mathcal{A}^\nu \begin{bmatrix} v \\ -v \end{bmatrix} = \begin{bmatrix} 2A^\nu - Q & -Q \\ -Q & -2A^\nu - Q \end{bmatrix} \begin{bmatrix} v \\ -v \end{bmatrix} = \begin{bmatrix} 2A^\nu v \\ 2A^\nu v \end{bmatrix} = \begin{bmatrix} 0 \\ 0 \end{bmatrix},$$

i.e., $\mathcal{A}^\nu$ is singular.

6 Stochastic Coefficients

Working with a deterministic model configuration assumes that the model, i.e., boundary and initial conditions, sources, material parameters and geometry, is known to an unnatural degree of accuracy. The value of simulation results can thus be questioned and asked to be replaced by more meaningful statistical quantities.

Since the lithographic processes in semiconductor production are susceptible to inaccuracies, there is a certain need for numerical simulations to reflect these inaccuracies. The approach followed here, assumes normally distributed stochastic coefficients to define the geometry. This leads to an ensemble of field solutions, derived from realizations of the stochastic coefficients when taking the underlying distribution into account. The transfer function is then measured in terms of statistical moments (i.e., expectation and variance), which allows to quantify the system behavior. Assuming an underlying stochastic distribution for the parameters, does not imply that the transfer function follows the same underlying distribution, as will be seen from numerical examples.

Sampling the transfer function by Monte-Carlo (MC) or stochastic collocation (SC) enables the approximation of the statistical moments. The MC method suffers from a slow mean convergence as $\mathcal{O}(1/\sqrt{n})$, where n is the sample size [Gla03]. The SC sample sizes on the other hand, grow exponentially in the parameter dimension. This motivates the combination of sampling and model reduction. The basic idea is to compute a reduced model valid over the sample set and use this model in the MC and SC methods. Since the sample set will depend on the probability distribution, the model reduction should take the distribution into account. Weighting the error estimator with the probability measure is a natural approach to achieve this [CQR13]. In [BBM$^+$09] and [Wie13], the error estimation has been extended to the statistical moments, assuming boundedness in the random variations.

While there are numerous publications regarding stochastic coefficients (see [XH05], [XT06] or [CQR14a]), the particular application to time-harmonic Maxwell's equations can be found in [HWCW10], [BS15] or [HBon]. In contrast to previous work, this work considers stochastic collocation for models with several random geometric parameters.

The aim of the following computation is to show, that sampling strategies for the statistical moments benefit from the RBM and that it is necessary, since the solution at the mean parameter values is not the same as the mean of the ensembles.

As in [BBM$^+$09], realizations of the random solutions are associated with deter-

ministic solutions of a deterministic PDE with a parametrization corresponding to the stochastic coefficients. Of particular interest are small random variations in geometry, due to inaccuracies in the production process. As an example application, the coplanar waveguide is used, see section 4.1 for a model description.

6.1 The Weighted Reduced Basis Sampling

Let $(\Omega_\omega, \mathcal{F}, \mathcal{P})$ denote a probability space. Given is a square integrable random variable $Y : \Omega_\omega \to \Gamma \subset \mathbb{R}^p$ with probability density function ρ and a function $g : \mathbb{R}^p \to \mathbb{R}^d$, where p is the number of parameters. The function g corresponds to a mapping of realizations of a random variable to the output of the electromagnetic system such that $g(Y)$ also is square-integrable [BS15].

Assuming normally distributed random variables, the probability density for the random variable Y is given by the multivariate normal distribution

$$\rho(\nu) = \frac{1}{\sqrt{(2\pi)^p \det(\Sigma)}} \exp\left(-\frac{1}{2}(\nu-\mu)^T \Sigma^{-1}(\nu-\mu)\right), \tag{6.1}$$

with p-by-1 vectors ν of parameter realizations, μ of expectations and Σ a p-by-p symmetric positive definite covariance matrix. Since the parameter variations considered here are uncorrelated, Σ is diagonal.

In a precomputation phase, a reduced model is generated which gives approximate solutions to the sampling of the statistical moments. A greedy sampling with the error estimator (3.24) is typically unfeasible, since the stochastic parameter spaces are too large. Thus, the error estimator Δ_N is weighted with the probability distribution [CQR13], such that either

$$\Delta_N^{\rho,\beta}(\nu) = \frac{\|r(\cdot;\nu)\|_{X'}\rho(\nu)}{\beta_{LB}(\nu)}, \tag{6.2}$$

can be used, or the error indicator

$$\Delta_N^{\rho}(\nu) = \|r(\cdot;\nu)\|_{X'}\rho(\nu). \tag{6.3}$$

Since the sampling of the stability constant also becomes unfeasible under stochastic coefficients, the error indicator (6.3) is used. Using the greedy sampling 3.2.1 with Δ_N^ρ generates a model, which enables the statistical sampling.

6.2 Sampling Statistical Moments

In statistical analysis, the expectation and variance of quantities of interest like the response surface w.r.t. uncertain parameters is computed. Evaluating the expected

transfer function $\mathbb{E}(g(Y))$ and variance of the transfer function $\mathrm{Var}(g(Y))$ under parametric variations, is computing the integrals

$$\mathbb{E}(g(Y)) = \int_\Gamma g(x)\rho(x)dx, \tag{6.4}$$

and

$$\begin{aligned} \mathrm{Var}(g(Y)) &= \int_\Gamma (g(x) - \mathbb{E}(g(Y)))^2\rho(x)dx & (6.5)\\ &= \int_\Gamma (g(x))^2\rho(x)dx - (\mathbb{E}(g(Y)))^2, & (6.6) \end{aligned}$$

respectively.

To compute the expectation, the integral is replaced by a quadrature rule

$$E(g(Y)) = \int_\Gamma g(x)\rho(x)dx \approx \sum_{i=1}^{n} g(\xi_i)w_i, \tag{6.7}$$

with sample points ξ_i, weights w_i and sample size n.

The software package SGMGA [Bur11], computes Hermite Genz-Keister quadrature points and weights for the integral

$$\int_{-\infty}^{\infty} g(x)\exp(-x^2)dx \approx \sum_{i=1}^{n} g(x_i)w_i. \tag{6.8}$$

Applying integration by substitution to adjust to a (μ_i, σ_i) normally distributed random variable leads to

$$\mathbb{E}(g(Y)) \approx \frac{1}{\sqrt{\pi}} \sum_{i=1}^{n} g(\sqrt{2}\sigma_i x_i + \mu_i)w_i, \tag{6.9}$$

and

$$\mathrm{Var}(g(Y)) \approx \frac{1}{\sqrt{\pi}} \sum_{i=1}^{n} (g(\sqrt{2}\sigma_i x_i + \mu_i))^2 w_i - (\mathbb{E}(g(Y)))^2. \tag{6.10}$$

The number of sample points depends on the quadrature rule and the number of parameters in an irregular fashion, see [BS15] and the references therein. Monte-Carlo simulations use equally weighted samples, which are generated using the underlying distribution. A drawback of the Monte-Carlo simulation is its mean convergence rate of $\mathcal{O}(1/\sqrt{n})$. The stochastic collocation is performed with Hermite Genz-Keister sparse grids, generated by the Smolyak algorithm. These types of methods can exhibit a mean convergence rate of $O((\log n)^p/n)$, see [PT97].

6.3 Coplanar Waveguide with Stochastic Coefficients

This section covers the coplanar waveguide, investigated in section 4.1, with uncertain geometric parameters. Related approaches with uncertain geometries of microwave models can be found in [LPS99] or [HP06].

6.3.1 Model Setup

The model is governed by the second order time-harmonic Maxwell's equations in the electric field E

$$\nabla \times \mu^{-1} \nabla \times E + \imath\omega\sigma E - \omega^2 \epsilon E = -\imath\omega j_i \quad \text{in} \quad \Omega, \tag{6.11}$$

subject to essential boundary conditions $E \times n = 0$ on $\Gamma_{\text{PEC}} = \partial\Omega$. The parameter vector ν is introduced to denote parametric dependence in frequency ω, geometry and material coefficients (μ, σ, ϵ).

After discretization with $H(\text{curl})$-conforming Nédélec finite elements, solving (2.72) reduces to solving a parameter-dependent sparse linear system $A(\nu)x(\nu) = \imath\omega b(\nu)$ for the state vector $x(\nu)$, which represents the electric field solution $E(\nu)$ in the discrete space X.

Using the transformation outlined in example 2.3.3, the state vector x is split into real and complex parts $x = x_{real} + \imath x_{imag}$. The complex linear system is rewritten as an equivalent system of twice the dimension over the real numbers. This leads to a real and symmetric system matrix (2.79), where the parametric dependence on ν carries over through the transformation. The full order simulation has been performed with the finite element package FEniCS [LMW12].

The model setup at hand considers only geometric stochastic variations with a deterministic parameter in the frequency. However, the computational approach is also applicable to more general parametric variations.

In section 3.3.3, the affine transformations required to map to the reference domain are shown for a deterministic geometric parameter in the coplanar waveguide. Fig. 6.1 shows the separation of the middle stripline into subsections. In the model with 10 geometric parameters, the affine transformation for a single geometry parameter is extended to multiple parameters by splitting the computational domain into distinct parts and applying the transformation to each subdomain. The same separation is used for two and three geometric parameters. Most computations use the model with two geometric parameters, since a finer discretization leads to models too complex to sample.

The geometric variations lead to an affine parameter dependence in the bilinear form. The affine decomposition for a single geometry parameter is then extended to multiple parameters by splitting the computational domain into distinct parts and applying the transformation to each subdomain.

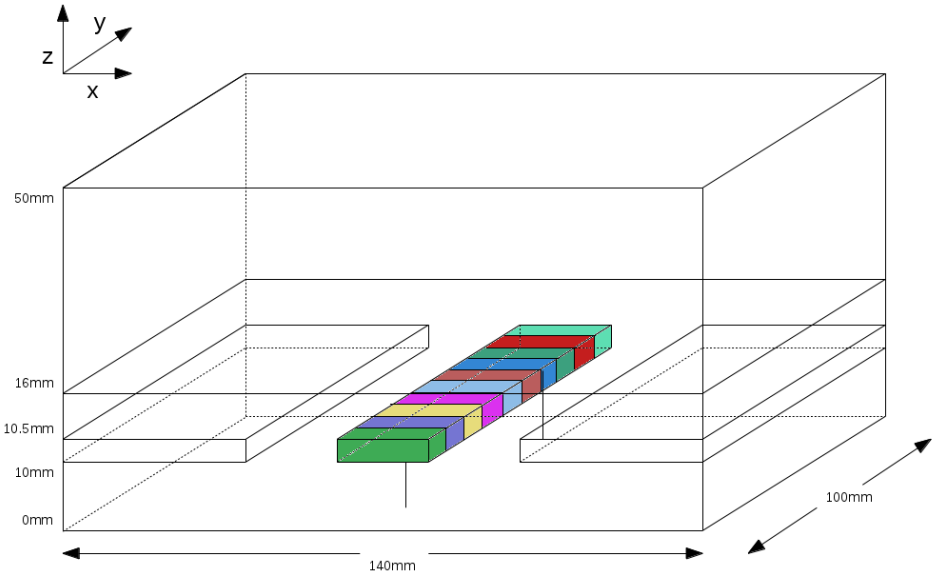

Figure 6.1: In the reference configuration, the width of the middle stripline is uniformly 6 mm. The width of the middle stripline varies for each colored part independently in the model with 10 geometric parameters.

The parameter setup assumes the segments of the middle stripline width to be normally distributed with mean 6 mm and standard deviation 0.1 mm. The underlying geometry gives bounds to the degree of parametric variations, so that technically a truncated normal distribution is considered. However, this difference is marginal, i.e., the probability is less than $1{\times}10^{-100}$ that a realization is outside the geometry bounds. The frequency range under consideration is $\omega \in [1.3, 1.6]$ GHz.

The reduced space X_N is built iteratively by a greedy sampling using the weighted error indicator (6.3). Starting from an initial reduced space, spanned by the snapshots at the expected values of the stochastic parameters, an error indicator is evaluated over the parametric domain. The next snapshot will then be chosen where the maximum of the error indicator is attained.

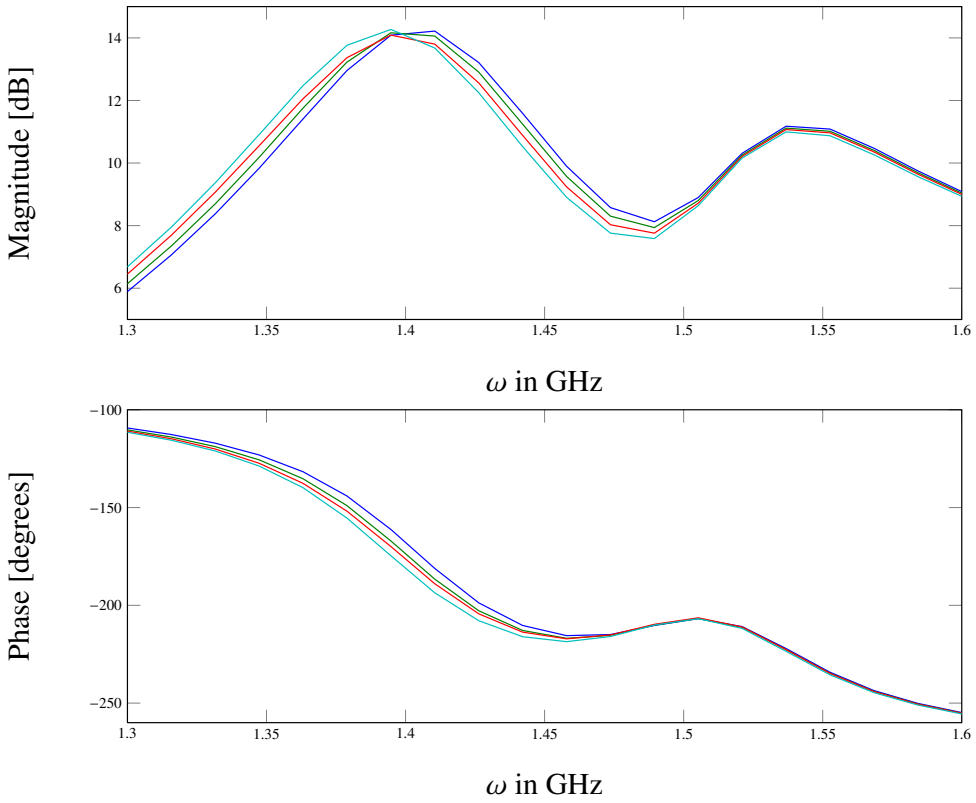

Figure 6.2: Bode plot over [1.3, 1.6] GHz. Sample expectation computed by Monte-Carlo simulation with a standard deviation of $\sigma = 0.1$ mm. Transfer function without geometric variation (dark blue), two geometric parameters (green), three geometric parameters (red) and ten geometric parameters (light blue).

6.3.2 Numerical Experiments

In Fig. 6.2 the frequency response is shown for different discretizations of the geometry. A Monte-Carlo simulation computed the mean trajectories. A direction is visible, in that with a finer resolution of geometry, the transfer function moves to the left until 1.45 GHz.

The weighted RBM uses a sample size of 20 in the frequency and 25 in the geometry. Only two geometric parameters are considered in the following. This is to keep the sample spaces reasonably small, since they grow exponentially with the number of parameters. The sample set in the geometric parameter covers the interval $[5.5, 6.5]$. Less than $1{\times}10^{-6}$ possible realizations of the normally distributed parameters are neglected by this interval, which ensures that most trajectories are well approximated.

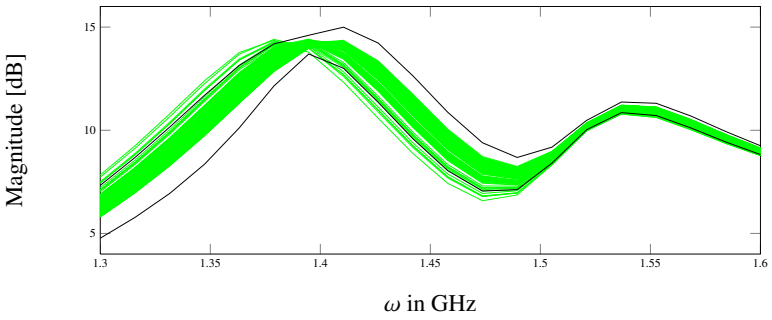

Figure 6.3: Realizations of the Monte-Carlo sampling with two geometric parameters (green). In black the $\pm 3\sigma_{\omega_p}$ deviations from the mean.

Fig. 6.3 shows the $\pm 3\sigma$ variations from the mean in black. The Monte-Carlo sampled transfer functions are shown in green. Of the realizations, 97% are within the $\pm 3\sigma$ deviation over the whole frequency interval.

Despite the use of an error indicator, the approximation quality can still be assessed. Computing the field solution at a number (here 20) of randomly chosen parameter locations (uniformly in the deterministic parameter and normally distributed in the stochastic coefficients), allows to check the error decay at these locations, see Fig. 6.4. Since only a one-sided projection is used here, the error decay is not as smooth as when using the two-sided projections with supremizing operators.

The reduced model of order 73 reaches an approximation tolerance of 5×10^{-6} and is used subsequently. It is plugged into a Monte-Carlo simulation with 20'000 solves, where the computation time is negligible, as the resulting systems are only of size 73×73. For the stochastic collocation RB the reduced system has been evaluated at the Hermite Genz-Keister (HGK) points. The 'mean expectation' shows the arithmetic mean of the computed expected transfer function as an indicator to compare the results. The 'mean relative error' shows the mean of the relative error in the transfer function with respect to the chosen reference solution. Each parameter configuration requires 20 solves to resolve the transfer function.

The 'mean expectation' shows the arithmetic mean of the computed expected transfer function as an indicator to compare the results. The 'mean relative error' shows the mean of the relative error in the transfer function with respect to the chosen reference solution. The 'mean std. deviation' shows the arithmetic mean of the computed sample standard deviation over the frequency range. Each parameter configuration requires 20 solves to resolve the transfer function. The table is ordered with respect to accuracy of the methods.

In Table 6.1 the Monte-Carlo simulation serves as a reference solution for the expectation. Most methods agree with the Monte-Carlo simulation up to an error of 1×10^{-3} and also the reduced order model shows comparable accuracy to the

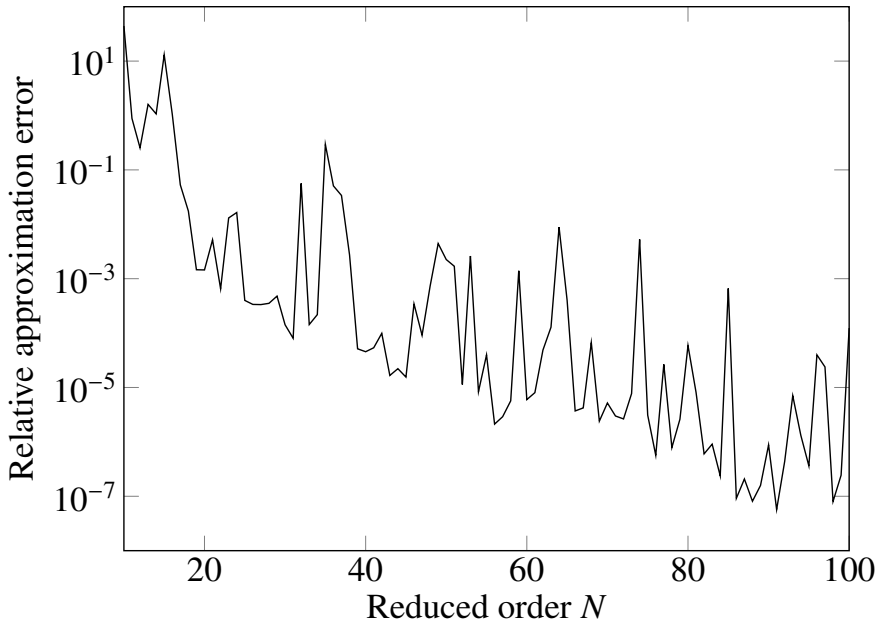

Figure 6.4: Mean relative approximation error in the H(curl; Ω) norm plotted against reduced basis size.

collocation and Monte-Carlo simulation. As the methods show a comparable mean relative error over the frequency range, it is reasonable to look at the stochastic collocation of order 4 as reference, which is shown in Table 6.2 and Table 6.3. The collocation rule of order 4 shows an agreement to 1×10^{-5} with the rules of order 3 and order 2 in the expectation. The reduced basis results confirm with an accuracy of 5×10^{-4}.

6.4 Possible Extensions

The approach presented here is heuristic in nature, since the convergence is only assumed from comparing results from different computational techniques, namely Monte-Carlo simulation and stochastic collocation, either with or without reduced basis model reduction. Depending on which result is taken as reference, very different conclusions on the achieved accuracy can be drawn, as was discussed on the presented results.

This can be remedied by extending the studies from [HUW13] to the Maxwell's equations. The studies provide error estimates in the expectation and variance for the coercive case, which can be extended to the inf-sup stable case. Since the problem studied here, depends affinely on the deterministic parameter and the stochastic

Table 6.1: Comparison of computed expectation using the Monte-Carlo simulation of the full system as reference.

Method	Linear Systems	mean expectation	mean relative error
Monte-Carlo	14'000 solves	3.372528	reference
HGK (order 4)	2'020 solves	3.373268	$1.1 \cdot 10^{-3}$
HGK (order 3)	900 solves	3.373268	$1.1 \cdot 10^{-3}$
HGK (order 2)	420 solves	3.373266	$1.1 \cdot 10^{-3}$
HGK (order 1)	100 solves	3.373639	$1.4 \cdot 10^{-3}$
Monte-Carlo RB	73 solves	3.373168	$1.8 \cdot 10^{-3}$
HGK (order 4) RB	73 solves	3.373436	$1.5 \cdot 10^{-3}$

coefficients, no empirical interpolation or Karhunen-Loève expansion is considered.

It is shown in [HUW13], that the expectation of the error bound for the deterministic problem gives on error bound on the error of the expectations between the full and reduced order model. This is formulated in Lemma 6.4.1 for the Maxwell's equations.

Lemma 6.4.1 (Error Bound on the Expectation)**.** *The error of the expectations of the full order solution $E(\nu, \omega)$ and reduced order solution $E_N(\nu, \omega)$ are rigorously bounded by the expectation of the error estimator for the deterministic case.*

$$|\mathbb{E}[E(\nu,\omega)] - \mathbb{E}[E_N(\nu,\omega)]| \leq \mathbb{E}[\Delta_N(\nu,\omega)] = \mathbb{E}[\frac{\|r(\cdot;\nu,\omega)\|_{X'}}{\beta_{LB}(\nu,\omega)}] \tag{6.12}$$

The proof uses the statement for the deterministic case, Lemma 3.2.1, and linearity of the expectation. Similar error estimates can be established for linear and quadratic outputs and for the variance. This procedure would allow a certification of the accuracy of the obtained results.

6.5 Further Computational Approaches

Besides stochastic collocation and Monte-Carlo simulation, other computational approaches are in use.

The stochastic Galerkin method [GS91] discretizes the space of uncertain parameters and is thus also termed as stochastic finite element method. The resulting

Table 6.2: Comparison of computed expectation using the stochastic collocation with Hermite Genz-Keister (order 4) rule as reference.

Method	Linear solves	mean expectation	mean rel. error
HGK (4th)	2'020	3.373268	reference
HGK (3rd)	900	3.373268	$1.8 \cdot 10^{-6}$
HGK (2nd)	420	3.373266	$3.3 \cdot 10^{-5}$
HGK (4th) RB	73	3.373436	$5.4 \cdot 10^{-4}$
MC RB (20k)	73	3.373168	$8.1 \cdot 10^{-4}$
MC	14'000	3.372528	$1.1 \cdot 10^{-3}$
MC RB (14k)	73	3.383087	$2.1 \cdot 10^{-2}$

systems are very large, as they assemble through a Kronecker product of the discretisation in physical space and parameter space.

The proper generalized decomposition (PGD, [CKL14]) is a technique to separate the parameter dependencies of the solution into a product of functions. Since the decomposition iteratively improves on the approximation quality, this can be used as a model reduction technique. It requires a priori knowledge on which parameter dependencies can be seperated. See [TMN14] for an application of the PGD to stochastic parameters.

6.6 Summary of Numerical Experiments

The RB approach to Uncertainty Quantification shows the potential to significantly reduce the computational costs. While a weighted sampling gave accurate results in the computed example, this result can be certified by using error estimators in the statistical quantities, see [HUW13] for more details.

The computational complexity does not only scale with the solved linear systems. The RB method requires additionally the evaluation of the residual over the parametric domain, which increases computational complexity by a factor between two and three. The cost for evaluating the residual thus becomes the bottleneck when using a tensor grid in higher parameter dimensions. Using appropriate sparse grids or other techniques as sampling space thus seems a viable future research perspective.

Table 6.3: Comparison of computed standard deviation using the stochastic collocation with Hermite Genz-Keister (order 4) rule as reference.

Method	Linear Systems	mean std. deviation
HGK (4th)	2'020	0.1015
HGK (3rd)	900	0.1015
HGK (2nd)	420	0.1004
HGK (4th) RB	73	0.1009
MC RB (20k)	73	0.0963
MC	14'000	0.1160
MC RB (14k)	73	0.0959

7 Reduced Basis Model Reduction for Time-Dependent Maxwell's Equations with Stochastic Temporal Dispersion

7.1 Reduced Basis Model Reduction of Time-Dependent Problems

As outlined in section 3.3.7, time-dependent problems are typically treated with a POD-Greedy approach [HO08], [Haa14]. The POD compression in time offers some tuning options. Either a fixed number of modes can be appended to the projection basis, or a number of modes corresponding to a percentage of the sum of the singular values. A high percentage, such as 99% is typically sufficient to resolve the trajectory accurately. This will be used here, such that the modes corresponding to the largest singular values are chosen until the sum of the associated singular values reaches 99% of the sum of all singular values.

In section 2.4, the time-dependent Maxwell's equations with temporal dispersion are derived. It is based on a single-pole expansion of the electric susceptibility χ. Such an expansion is also called a Debye model. To avoid computing the convolution integral, an auxiliary differential equation in the polarization is derived [Jin11], see (7.2) and (7.3). The resulting equations are termed Maxwell's equations with bipolar orientational temporal dispersion, or Maxwell-Debye model for short [BF08]. Here, the term $\epsilon_0 \epsilon_r E(t, \mathbf{x})$ is replaced by

$$\epsilon_0 \epsilon_\infty E(t, \mathbf{x}) + \epsilon_0 \int_{-\infty}^{t} E(t - \tau, \mathbf{x}) \chi(\tau) d\tau. \tag{7.1}$$

The Debye relaxation models polar molecules with a permanent dipole moment. Under the application of an external field, the molecules rotate and cause friction, which leads to an exponential damping.

The POD-Greedy approach evaluates the error indicator (3.67) over the parameter domain to select the next parameter configuration. At this parameter configuration, the trajectory is computed and condensed by the POD. The dominant modes are then appended to the projection basis.

7.2 Maxwell's Equations with Dielectric Relaxation - Computations on a Unit Square

Consider the Maxwell-Debye model formulated as second-order form in the electric field E and the polarization P

$$\frac{1}{\mu_0}\nabla \times \nabla \times E + \epsilon_0 \epsilon_\infty \partial_t^2 E = f - \partial_t^2 P \tag{7.2}$$

$$\partial_t P + \frac{1}{\tau} P = \frac{\epsilon_0(\epsilon_s - \epsilon_\infty)}{\tau} E \tag{7.3}$$

with relaxation time τ, relative permittivity at low-frequency limit ϵ_s and relative permittivity at high-frequency limit ϵ_∞, and a broadband input source f, which is modeled as a Gaussian pulse. The equations are discretized with Nèdèlec finite elements of first order over a 2D unit square, i.e., 1 m-by-1 m.

Either normalized physical values can be used or actual, physical values. This work uses physical values to simulate wave propagation through media such as water or foam. Since the relaxation time is in the range of nanoseconds, the time-stepping is chosen as $\Delta_t = 1 \times 10^{-11}$ s. To achieve a broadband input source, a Gaussian pulse is assumed at the center of the computational domain. To excite the system, the Gaussian pulse is taken in the magnetic fields z-component, perpendicular to the computational domain. The excitation to the electric field in the x- and y-component, occurs then by taking the curl of the pulse. Experiments have shown, that this excites a large number of frequencies. The derivative of the Gaussian pulse is used to excite the system in time.

The computational mesh consists of $9'680$ degrees of freedom and assumes a PEC condition on all boundaries. The time-stepping is realized by a Runge-Kutta-Nyström scheme in the electric field and an explicit Euler in the polarization. The Runge-Kutta-Nyström scheme [CSS92] makes use of the particular form $\ddot{E} = \mathcal{F}(t, E)$ found in (7.2) by a simple transformation so that $\partial_t^2 E$ is on one side of the equation and $\mathcal{F}(t, E)$ denotes the other side. The equations (7.2) and (7.3) are solved in turn, i.e. assuming an initial condition of $E(t, x) = 0$ and $P(t, x) = 0$, first (7.2) is solved and then the time derivative of (7.3) is solved for $\partial_t^2 P$ with $\partial_t E$ plugged in. The solution for $\partial_t^2 P$ is then used in (7.2) for the next timestep. The Runge-Kutta-Nyström scheme used here computes for each timestep t_k

$$
\begin{aligned}
k_1 &= \mathcal{F}(t_k, E(t_k) + \frac{3+\sqrt{3}}{6}\Delta_t \partial_t E(t_k)),\\
k_2 &= \mathcal{F}(t_k, E(t_k) + \frac{3-\sqrt{3}}{6}\Delta_t \partial_t E(t_k) + \frac{2-\sqrt{3}}{12}\Delta_t^2 k_1),\\
k_3 &= \mathcal{F}(t_k, E(t_k) + \frac{3+\sqrt{3}}{6}\Delta_t \partial_t E(t_k) + \frac{\sqrt{3}}{6}\Delta_t^2 k_2),\\
E(t_{k+1}) &= E(t_k) + \Delta_t \partial_t E(t_k) + \Delta_t^2(\frac{5-3\sqrt{3}}{24}k_1 + \frac{3+\sqrt{3}}{12}k_2 + \frac{1+\sqrt{3}}{24}k_3),\\
\partial_t E(t_{k+1}) &= \partial_t E(t_k) + \Delta_t(\frac{3-2\sqrt{3}}{12}k_1 + \frac{1}{2}k_2 + \frac{3+2\sqrt{3}}{12}k_3),
\end{aligned}
$$

such that $\partial_t^2 E(t_{k+1})$ can be computed by evaluating $\mathcal{F}$ at t_{k+1}, but this is actually not necessary, since $\partial_t^2 E(t_{k+1})$ is not required in (7.3).

In Fig. 7.1 and Fig. 7.2, two example trajectories are shown. Due to the smaller permittivities in Fig. 7.1, the propagation velocity is larger and the fields are not as strongly damped as in Fig. 7.2.

7.3 POD-Greedy Model Order Reduction

The model is parametrized by $\tau \in [1 \times 10^{-10}, 1 \times 10^{-6}]$ s and $\Delta_\epsilon = \epsilon_s - \epsilon_\infty \in [1, 5]$, defining the 2-dimensional parameter domain $D = [1 \times 10^{-10}, 1 \times 10^{-6}] \times [1, 5]$. A reduced model which accurately captures the dynamics in the parameter domain D is generated.

The greedy algorithm iteratively builds a basis for a reduced model by evaluating an error indicator over a sampled parameter domain and adding basis vectors at the parameter location where the error indicator attains its maximum. A parameter location is denoted by a parameter vector $\nu = [\tau, \Delta_\epsilon]$ and trajectories of 5000 timesteps were computed for each parameter evaluation.

An initial parameter location is chosen in the center of the parameter domain. The full-order model trajectory is computed at this parameter location (in the electric field and the polarization) and a POD-basis is computed for the polarization and the electric field independently from each other by capturing 99% of the energy of the modes. A composite basis of reduced dimension $2N$ is then established by taking the N largest modes from the POD-basis of the electric field and polarization, respectively. The error indicator is based on the residual $R(w; \nu)$, which is evaluated over the sampled parameter domain, i.e. 9-by-5 samples.

The greedy algorithm took four iterations to compute a basis which accurately captures the dynamics in the domain, i.e. the actual relative error is less than 1×10^{-6} at a reduced dimension of 150. The full order model is of dimension 9680.

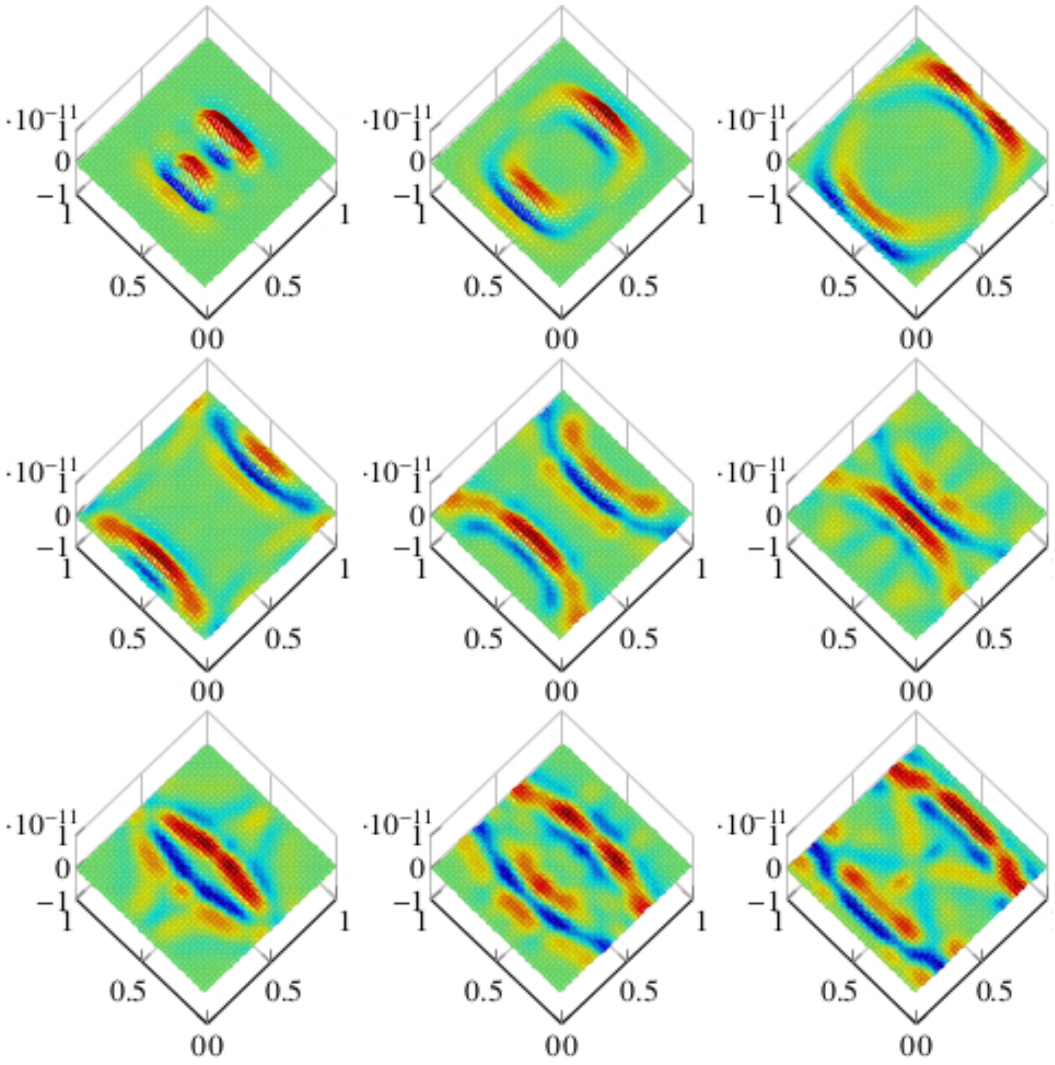

Figure 7.1: Snapshots of one component of the trajectory using $\epsilon_\infty = 1$, $\epsilon_s - \epsilon_\infty = 0.5$ and $\tau = 1 \times 10^{-9}$. From top left to bottom right, timesteps 100, 150, 200, 250, 300, 350, 400, 450 and 500.

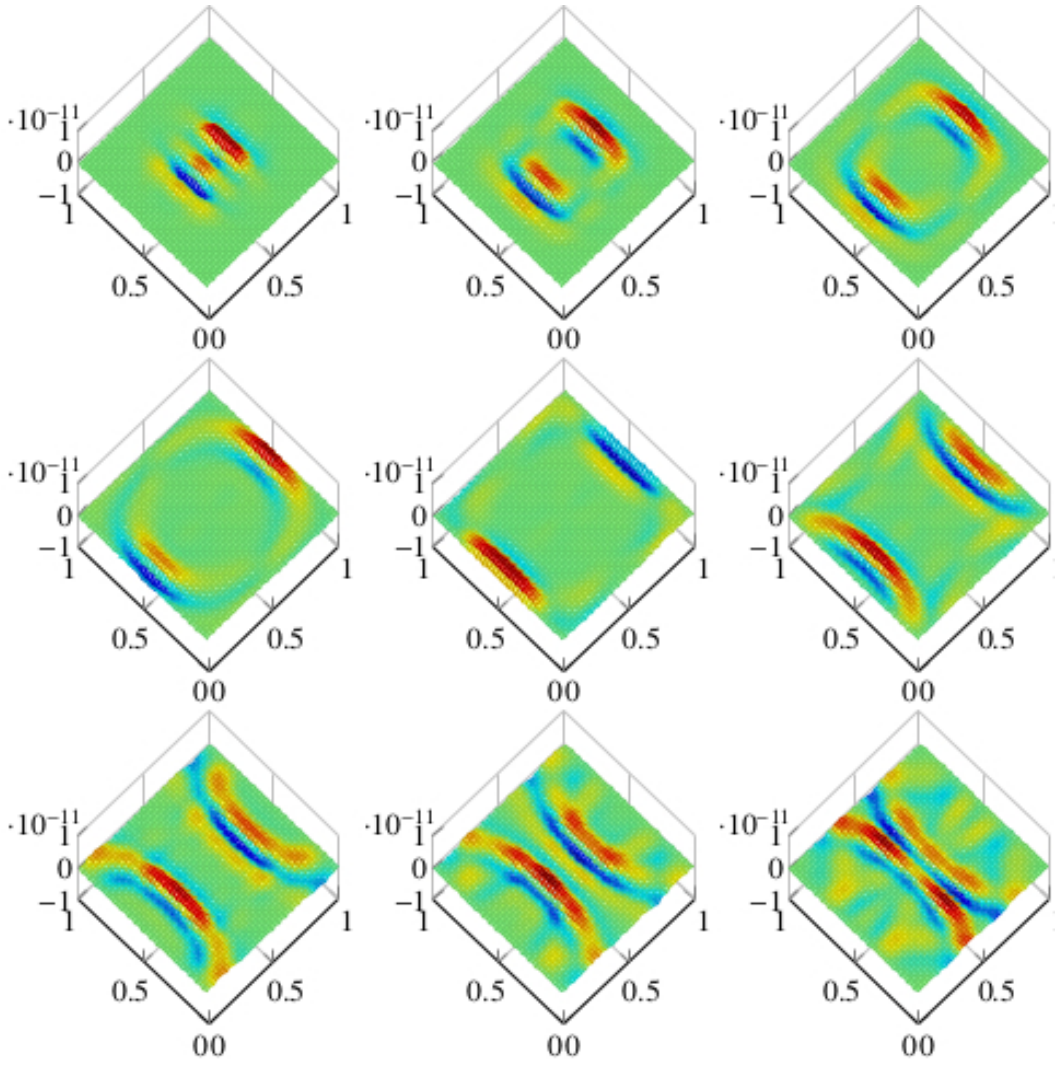

Figure 7.2: Snapshots of one component of the trajectory using $\epsilon_\infty = 2$, $\epsilon_s - \epsilon_\infty = 1.5$ and $\tau = 1 \times 10^{-8}$. From top left to bottom right, timesteps 100, 150, 200, 250, 300, 350, 400, 450 and 500.

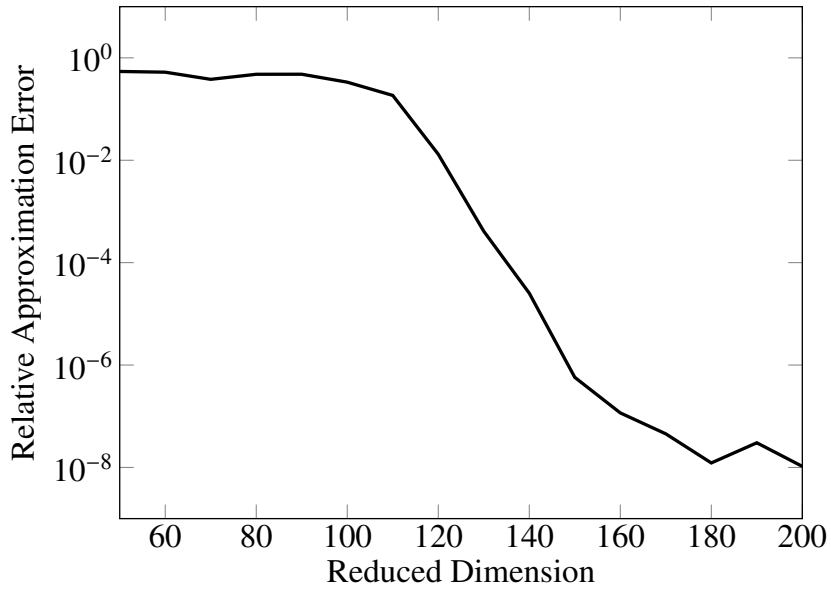

Figure 7.3: Maximum of the actual relative error plotted against the reduced model size.

Fig. 7.3 shows the actual relative error in the L2-norm for varying reduced model sizes. Plotted is the maximum attained over the sampled parameter domain, averaged over all timesteps. Exponential convergence speed can be seen, starting at a reduced basis size of about 110.

7.4 Uncertainty Quantification

Consider τ and Δ_ϵ as normally distributed, stochastically varying parameters of the generated reduced model. Using Monte-Carlo simulation, Hermite Genz-Keister stochastic collocation and Gauss-Hermite stochastic collocation, the expectation and variance can be computed and empirically validated by comparing the error amongst the different methods. The theoretical and computational approach taken is the same as outlined in chapter 6.

Using the reduced model significantly reduces computational costs, as each sample point evaluation uses the reduced model. The dominating computational effort then lies in the number of system solves used to generate the reduced model.

The stochastic setting could be already incorporated in the model reduction by using the weighted RB, which has been introduced in [CQR13]. In the weighted RB, the error indicator takes the probability distribution into account as well.

Both stochastic parameters are modeled as normally distributed random variables

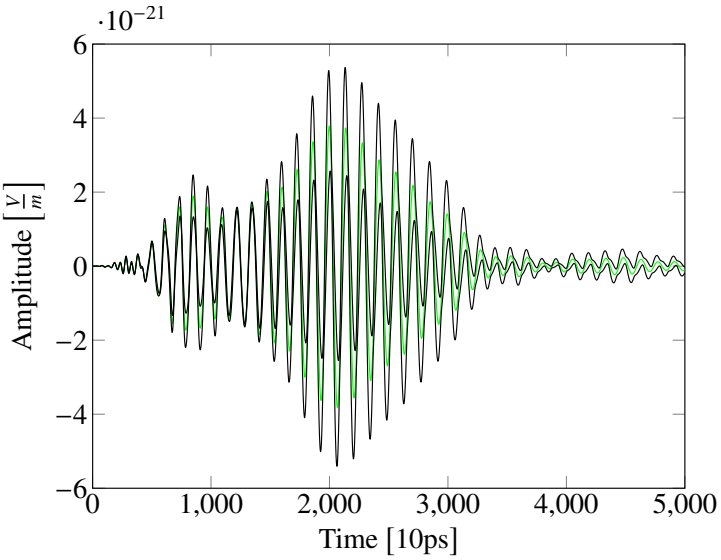

Figure 7.4: Mean trajectory of the Monte-Carlo simulation in green, the $\pm\,\sigma$-variation is shown in black. Of the Monte-Carlo realizations, 32% fit the σ-tube over all timesteps.

and are assumed to be stochastically independent from each other. The SGMGA package [Bur11] is employed for computation of Hermite Genz-Keister and Gauss-Hermite integration points and weights. A single degree of freedom has been chosen as output functional and trajectories of 5000 timesteps were computed for each parameter evaluation. In Table 7.1 the Gauss-Hermite (GH) stochastic collocation of order 4 serves as a reference solution for the expectation. The Hermite Genz-Keister (HGK) stochastic collocation of order 4 shows similar results when taken as a reference solution for the expectation. As the Monte-Carlo (MC) simulation coincides with other methods only to a level of 10^{-2}, the GH of 4th order is a more viable reference choice.

The RB model size used was 200 for all computations, which shows a relative error of $3 \cdot 10^{-10}$ to the full order model at the expectation values of the parameter. The Monte-Carlo simulation performed 10000 solves with the reduced model, while the collocation methods of 4th order only took 97 solves (GH) and 101 solves (HGK), respectively.

In summary, the RB approach to Uncertainty Quantification significantly reduces the computational costs, when used in a sampling with a weighted error indicator.

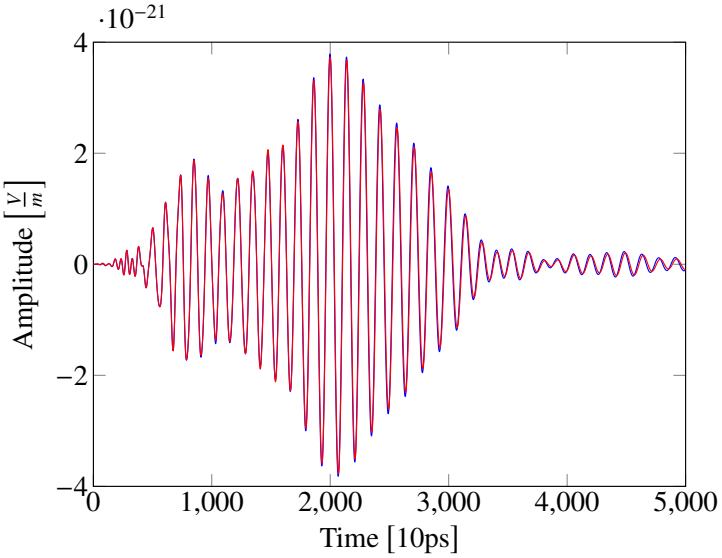

Figure 7.5: Solution at the mean parameter values (blue) and expectation of the Monte-Carlo simulation (red). Due to the oscillations around zero and the increasing shift between both trajectories, the error is larger than 50%.

Table 7.1: Comparison of methods using the stochastic collocation with Gauss-Hermite (order 4) rule as reference.

Method	mean expectation	mean rel. error	mean std. dev.
GH (4th)	$2.8577464 \cdot 10^{-25}$	reference	$4.4318510 \cdot 10^{-22}$
HGK (4th)	$2.8577467 \cdot 10^{-25}$	$1.52 \cdot 10^{-08}$	$4.4318509 \cdot 10^{-22}$
HGK (3rd)	$2.8577504 \cdot 10^{-25}$	$6.57 \cdot 10^{-07}$	$4.4318448 \cdot 10^{-22}$
GH (3rd)	$2.8577492 \cdot 10^{-25}$	$1.01 \cdot 10^{-06}$	$4.4318551 \cdot 10^{-22}$
HGK (2nd)	$2.8584345 \cdot 10^{-25}$	$1.63 \cdot 10^{-04}$	$4.4289067 \cdot 10^{-22}$
GH (2nd)	$2.8585074 \cdot 10^{-25}$	$1.65 \cdot 10^{-04}$	$4.4284254 \cdot 10^{-22}$
MC	$2.7470865 \cdot 10^{-25}$	$3.66 \cdot 10^{-02}$	$4.3727445 \cdot 10^{-22}$

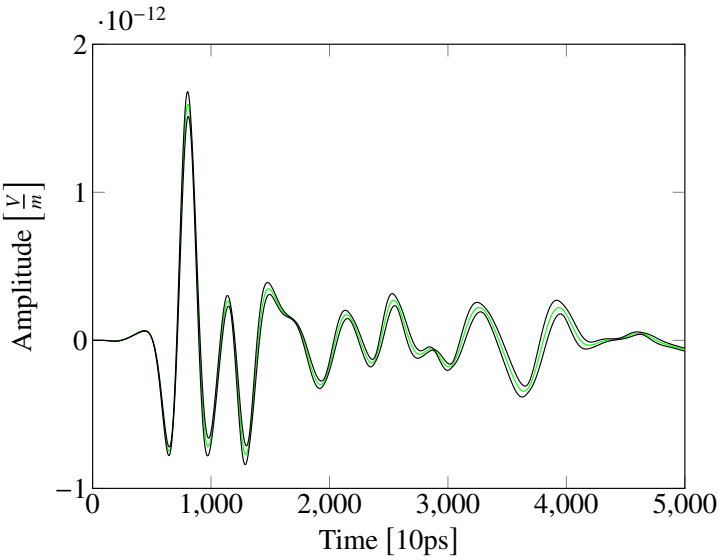

Figure 7.6: Trajectory of a degree of freedom, which was hit by the main wavefront. Mean trajectory of the Monte-Carlo simulation in green, the $\pm\,\sigma$-variation is shown in black.

8 Conclusions and Outlook

It could be shown, that the RBM computes low-order, accurate models of three-dimensional industrial applications governed by Maxwell's equations. The chosen input-output relation corresponds to Z-parameters, where the Petrov-Galerkin projection based on the supremizing operators turned out to significantly increase the approximation quality.

The central concept of the offline-online decomposition can be viewed from different angles, depending on the available resources. The standpoint of having a virtually infinite offline time, i.e., offline computations are performed on supercomputers and the task is broken down into parallelizable parts (for instance by a decomposition of the parameter domain), allows for rigorous error estimation, certifying the accuracy in the online phase. It potentially also generates the lowest-order models, as a large offline time can make use of compliant expanded formulations or use an optimization routine to determine the precise location of the current maximum error estimate. In practice, the offline time might be limited, such that heuristic techniques of stability constant estimation or checking the accuracy by computing the full order solution at a few random solutions are of value. While the offline computational times for rigorous error estimation are a matter of ongoing investigation, non-rigorous error estimation computes usable models in a reasonable time. In particular, the MinRes estimator gives accurate approximations to the stability constant, as shown in chapter 5.

In the case of geometries set by stochastic coefficients, the weighted RBM generates a reduced order model, valid over the range of the random variables. This potentially allows for multiple purposes. In this work, the benefit in collocation methods was shown. As the different collocation methods showed an agreement up to an order of 1×10^{-6} in the statistical moments using the reduced basis model, the weighted sampling can be considered usable. But even with a weighted error indicator, high dimensional stochastic parameter spaces require a huge number of residual evaluations. In this setting, the evaluations of the coefficient functions turned out to be limiting the runtime, such that the modeling with an EIM-like compression technique for affine expansions with many terms might be of use in more complex models. Using sparse grids as a sample space might also potentially remedy this situation. The reduced model could also be used in a stochastic Galerkin setting for instance. Since the affine parameter dependency is maintained in the reduced order model, the reduced order model could be computed a priori and then the stochastic Galerkin method is applied to the reduced order model. This would lead to significantly smaller system sizes in

the stochastic Galerkin method. Deriving error bounds in the statistical moments is desirable in this context.

Besides the time-harmonic Maxwell's equations, also the time-dependent case is amenable to the RBM. The case of temporally dispersive materials shows, that the RBM can compress even such complex, parametric models, thus enabling more physical simulations. In particular, nonlinear relations in Maxwell's equations are currently unexplored by the RBM, while being present in many engineering problems.

Comparing the RBM to established techniques for the model reduction in electromagnetics, namely the proper orthogonal decomposition (POD) and moment matching (MM), shows that the RBM gives comparable accuracy. A particular feature is the error estimation, which is not common in POD or MM, and could even give the RBM an advantage over POD and MM in more complex models. The comparison showed an advantage of the MM when considering the computational effort. The computation of additional moments is not expensive when the LU decomposition of the system matrix is available. This could be of use to the reduced basis methodology, in that also derivatives similar to the MM are included in the RB space. The potential advantage were a reduced offline time while maintaining the same accuracy. However, when directly using the RB Taylor spaces, such an advantage was not visible, although this might be due to model specific differences.

The RBM is designed as a black-box algorithm for parameter estimation in a wide variety of engineering tasks. Judging from the presented results, the RBM is beneficial in fast frequency sweeps, affine parameter dependencies with moderate (≤ 3) number of parameters and coupled linear problems, when a relaxed, i.e., non-rigorous, error estimation is used.

Theses

1. This work deals with the application of the reduced basis model reduction to electromagnetic problems. It shows that the reduced basis method is beneficial in parameter estimation tasks.

2. The fundamentals of computational electromagnetics and the reduced basis method are presented. Particularities, such as the Petrov-Galerkin projection and the MinRes estimator, which allow the successful application of the reduced basis method to computational electromagnetics are discussed in depth.

3. Numerical examples show an exponential convergence of the approximation error between the high-fidelity and reduced-order model.

4. The benefit of proper sampling with an error estimator instead of an error indicator is shown.

5. Since a rigorous error estimation can be too computationally involved due to the expensive inf-sup constant estimation, quickly computable, non-rigorous alternatives are explored. The MinRes estimator gave the most accurate approximations.

6. Stochastically varying parameters influence the transfer function, such that the solution at the mean parameter values does not match the expectation of the transfer function.

7. The stochastic collocation in combination with the reduced basis method provides an efficient computational technique for sampling the statistical moments.

8. Weighting the error estimator or error indicator with the probability density function allows to sample the parameter domain efficiently.

9. The reduced basis method is also applied to time-dependent Maxwell's equations with stochastically varying temporal dispersion, which shows the potential, that the reduced basis method can be used in more physically motivated models. In particular, nonlinear material relations are often encountered in Maxwell's equations, which might be amenable to the reduced basis model reduction.

10. In the case of a quickly oscillating time-dependent electromagnetic field with stochastically varying temporal dispersion, the solution at the mean parameter values and the expectation of the transfer function, show an increasing shift in time. This creates a significant relative error between both trajectories.

Bibliography

[AD11] M. Ahmadloo and A. Dounavis. Sensitivity analysis of microwave circuits using parametrized model order reduction techniques. *IEEE Transactions on Components, Packaging and Manufacturing Technology*, 1(11):1795–1805, 2011.

[ASB78] B. O. Almroth, P. Stern, and F. A. Brogan. Automatic choice of global shape functions in structural analysis. *AIAA Journal*, 16(5):525 – 528, 1978.

[BM08] B. Haasdonk and M. Ohlberger. Reduced basis method for finite volume approximations of parametrized linear evolution equations. *ESAIM: M2AN*, 42(2):277–302, 2008.

[BBG09] H. T. Banks, V. A. Bokil, and N. L. Gibson. Analysis of stability and dispersion in a finite element method for debye and lorentz dispersive media. *Numerical Methods for Partial Differential Equations*, 25(4):885–917, 2009.

[BMNP04] M. Barrault, Y. Maday, N. C. Nguyen, and A. T. Patera. An 'empirical interpolation' method: application to efficient reduced-basis discretization of partial differential equations. *Comptes Rendus Mathematique*, 339(9):667 – 672, 2004.

[BF14] P. Benner and L. Feng. A robust algorithm for parametric model order reduction based on implicit moment matching. In A. Quarteroni and G. Rozza, editors, *Reduced Order Methods for Modeling and Computational Reduction*, volume 9 of *Modeling, Simulation and Applications*, pages 159–185. Springer Switzerland, 2014.

[BH12] P. Benner and M. W. Hess. The reduced basis method for time-harmonic Maxwell's equations. *Proceedings in Applied Mathematics and Mechanics*, 12(1):661–662, 2012.

[BS15] P. Benner and J. Schneider. Uncertainty quantification for Maxwell's equations using stochastic collocation and model order reduction. *International Journal for Uncertainty Quantification*, 5(3):195–208, 2015.

[BF08] B. Bidégaray-Fesquet. Stability of FDTD schemes for Maxwell-Debye and Maxwell-Lorentz equations. *SIAM Journal on Numerical Analysis*, 46(5):2551–2566, 2008.

[BCD+11] Peter Binev, Albert Cohen, Wolfgang Dahmen, Ronald DeVore, Guergana Petrova, and Przemyslaw Wojtaszczyk. Convergence rates for greedy algorithms in reduced basis methods. *SIAM Journal on Mathematical Analysis*, 43(3):1457–1472, 2011.

[Bod13] A. Bodendiek. *Moment Matching based Model Order Reduction in Compuational Electromagnetism.* PhD thesis, TU Braunschweig, 2013.

[BM82] D. Bonin and D. A. Mellichamp. A unified derivation and critical review of modal approaches to model reduction. *Int. J. Control*, 35:829 – 848, 1982.

[BW12] A. Bostani and J. P. Webb. Finite-element eigenvalue analysis of propagating and evanescent modes in 3-d periodic structures using model-order reduction. *IEEE Transactions on Microwave Theory and Techniques*, 60:2677 – 2683, 2012.

[BBM+09] S. Boyaval, C. Le Bris, Y. Maday, N. C. Nguyen, and A. T. Patera. A reduced basis approach for variational problems with stochastic parameters: Application to heat conduction with variable robin coefficient. *Computer Methods in Applied Mechanics and Engineering*, 198(41–44):3187–3206, 2009.

[BEOR14] A. Buhr, C. Engwer, M. Ohlberger, and S. Rave. A numerically stable a posteriori error estimator for reduced basis approximations of elliptic equations. *Proceedings of the 11th World Congress on Computational Mechanics*, pages 4094–4102, 2014.

[Bur11] J. Burkardt. SGMGA toolbox - sparse grid mixed growth anisotropic rules. Technical report, 2011.

[CG14] S. Karmakar M. Pal R. Ghatek C. Goswami, S. Mukherjee. FDTD modeling of Lorentzian DNG metamaterials by auxiliary differential equation method. *Journal of Electromagnetic Analysis and Applications*, 6(5):106–114, 2014.

[CSS92] M. P. Calvo and J. M. Sanz-Serna. Order conditions for canonical Runge-Kutta-Nyström methods. *BIT Numerical Mathematics*, 32(1):131–142, 1992.

[CFCA13] Kevin Carlberg, Charbel Farhat, Julien Cortial, and David Amsallem. The {GNAT} method for nonlinear model reduction: Effective implementation and application to computational fluid dynamics and turbulent flows. *Journal of Computational Physics*, 242:623 – 647, 2013.

[CQR13] P. Chen, A. Quarteroni, and G. Rozza. A weighted reduced basis method for elliptic partial differential equations with random input data. *SIAM Journal on Numerical Analysis*, 51(6):3163 – 3185, 2013.

[CQR14a] P. Chen, A. Quarteroni, and G. Rozza. Comparison between reduced basis and stochastic collocation methods for elliptic problems. *Journal of Scientific Computing*, 59:187 – 216, 2014.

[CQR14b] P. Chen, A. Quarteroni, and G. Rozza. A weighted empirical interpolation method: a priori convergence analysis and applications. *ESAIM: Mathematical Modelling and Numerical Analysis*, 48:943–953, 7 2014.

[Che15] Y. Chen. A certified natural-norm successive constraint method for parametric inf-sup lower bounds. `arxiv.org/pdf/1503.04760`, 2015.

[CHM11] Y. Chen, J. S. Hesthaven, and Y. Maday. A seamless reduced basis element method for 2d Maxwell's problem: An introduction. In Jan S. Hesthaven and Einar M. Ronquist, editors, *Spectral and High Order Methods for Partial Differential Equations*, volume 76 of *Lecture Notes in Computational Science and Engineering*, pages 141–152. Springer Berlin Heidelberg, 2011.

[CHMR08] Y. Chen, J. S. Hesthaven, Y. Maday, and J. Rodriguez. A monotonic evaluation of lower bounds for inf-sup stability constants in the frame of reduced basis approximations. *Comptes Rendus Mathematique*, 346(23â24):1295 – 1300, 2008.

[CHMR09] Y. Chen, J. S. Hesthaven, Y. Maday, and J. Rodriguez. Improved successive constraint method based a posteriori error estimate for reduced basis approximation of 2d Maxwell's problem. *ESAIM: Mathematical Modelling and Numerical Analysis*, 43:1099 – 1116, 2009.

[CHMR10] Y. Chen, J. S. Hesthaven, Y. Maday, and J. Rodriguez. Certified reduced basis methods and output bounds for the harmonic Maxwell's equations. *SIAM Journal on Scientific Computing*, 32(2):970–996, 2010.

[CHM+12] Y. Chen, J. S. Hesthaven, Y. Maday, J. Rodriguez, and X. Zhu. Certified reduced basis method for electromagnetic scattering and radar cross section estimation. *Computer Methods in Applied Mechanics and Engineering*, 233â236(0):92 – 108, 2012.

[CKL14] F. Chinesta, R. Keunings, and A. Leygue. *The proper generalized decomposition for advanced numerical simulations.* Springer International Publishing, 2014.

[CGDD11] K. Crombecq, D. Gorissen, D. Deschrijver, and T. Dhaene. A novel hybrid sequential design strategy for global surrogate modeling of computer experiments. *SIAM Journal on Scientific Computing*, 33:1948 – 1974, 2011.

[dlRRM09] V. de la Rubia, U. Razafison, and Y. Maday. Reliable fast frequency sweep for microwave devices via the reduced-basis method. *IEEE Transactions on Microwave Theory and Techniques*, 57:2923 – 2937, 2009.

[Ded10] L. Dedé. Reduced basis method and a posteriori error estimation for parametrized linear-quadratic optimal control problems. *SIAM Journal on Scientific Computing*, 32(2):997–1019, 2010.

[Dep08] S. Deparis. Reduced basis error bound computation of parameter-dependent navier-stokes equations by the natural norm approach. *SIAM Journal on Numerical Analysis*, 46(4):2039–2067, 2008.

[DLK10] C. Duan, B. J. LaMeres, and S. P. Khatri. *On and Off-Chip Crosstalk Avoidance in VLSI Design.* Springer US, 2010.

[EPR10] J. L. Eftang, A. T. Patera, and E. M. Ronquist. An 'hp' certified reduced basis method for parametrized elliptic partial differential equations. *SIAM Journal on Scientific Computing*, 32(6):3170–3200, 2010.

[FHMS11] M. Fares, J.S. Hesthaven, Y. Maday, and B. Stamm. The reduced basis method for the electric field integral equation. *Journal of Computational Physics*, 230(14):5532 – 5555, 2011.

[FKDA13] F. Ferranti, L. Knockaert, T. Dhaene, and G. Antonini. Parametric macromodeling for S-parameter data based on internal nonexpansivity. *International Journal of Numerical Modelling: Electronic Networks, Devices and Fields*, 26:15 – 27, 2013.

[Fre04] R. W. Freund. SPRIM: Structure-preserving reduced-order interconnect macromodeling. In *Proceedings of the 2004 IEEE/ACM International conference on Computer-aided design*, ICCAD '04, pages 80 – 87. IEEE Computer Society, 2004.

[GHS12] M. Ganesh, J.S. Hesthaven, and B. Stamm. A reduced basis method for electromagnetic scattering by multiple particles in three dimensions. *Journal of Computational Physics*, 231(23):7756 – 7779, 2012.

[GDFZ99] J. De Geest, T. Dhaene, N. Faché, and D. De Zutter. Adaptive CAD-model building algorithm for general planar microwave structures. *IEEE Transactions on Microwave Theory and Techniques*, 47:1801 – 1809, 1999.

[GS91] R. G. Ghanem and P. D. Spanos. *Stochastic Finite Elements: A Spectral Approach*. Springer New York, 1991.

[GS02] M. Giles and E. Süli. Adjoint methods for PDEs: a posteriori error analysis and postprocessing by duality. *Acta numerica*, 11:145–236, 2002.

[Gla03] P. Glasserman. *Monte Carlo Methods in Financial Engineering*. Springer New York, 2003.

[GCC+10] D. Gorissen, K. Crombecq, I. Couckuyt, T. Dhaene, and P. Demeester. A surrogate modeling and adaptive sampling toolbox for computer based design. *Journal of Machine Learning Research*, 11:2051 – 2055, 2010.

[GMNP07] M. A. Grepl, Y. Maday, N. C. Nguyen, and A. T. Patera. Efficient reduced-basis treatment of nonaffine and nonlinear partial differential equations. *Mathematical Modelling and Numerical Analysis (M2AN)*, 41:575 – 605, 2007.

[Haa13] B. Haasdonk. Convergence rates of the POD-greedy method. *ESAIM: Mathematical Modelling and Numerical Analysis*, 47:859–873, 5 2013.

[Haa14] B. Haasdonk. Reduced basis methods for parametrized PDEs – a tutorial introduction for stationary and instationary problems. Technical report, 2014. Chapter to appear in P. Benner, A. Cohen, M. Ohlberger and K. Willcox: "Model Reduction and Approximation for Complex Systems", Springer.

[HO08] B. Haasdonk and M. Ohlberger. Reduced basis method for finite volume approximations of parametrized linear evolution equations. *ESAIM: M2AN*, 42(2):277–302, 2008.

[HUW13] B. Haasdonk, K. Urban, and B. Wieland. Reduced basis methods for parametrized partial differential equations with stochastic influences using the Karhunen-Loève expansion. *SIAM Journal on Uncertainty Quantification*, 1:79–105, 2013.

[Han91] M. S. Handcock. On Cascading Latin Hypercube Designs and Additive Models for Experiments. *Communications in Statistics - Theory and Methods*, 20:417 – 439, 1991.

[Har93] R. F. Harrington. *Field Computation by Method of Moments.* IEEE Press, Piscataway, NJ, 1993.

[Har04] R. F. Harrington. *Time-Harmonic Electromagnetic Fields.* IEEE Press, Piscataway, NJ, 2004.

[HC14] T. Henneron and S. Clenet. Model order reduction of non-linear magnetostatic problems based on POD and DEI methods. *Magnetics, IEEE Transactions on*, 50(2):33–36, Feb 2014.

[HB13a] M. W. Hess and P. Benner. Fast Evaluations of Time-Harmonic Maxwell's Equations Using the Reduced Basis Method. *IEEE Transactions on Microwave Theory and Techniques*, 61:2265–2274, 2013.

[HB13b] M. W. Hess and P. Benner. Reduced basis generation for maxwell's equations by rigorous error estimation. In *Proceedings of 19th International Conference on the Computation of Electromagnetic Fields (COMPUMAG 2013), Paper PD2-10 (2 pp.)*, 2013.

[HB14] M. W. Hess and P. Benner. A Reduced Basis Method for Microwave Semiconductor Devices with Geometric Variations. *COMPEL - The International Journal for Computation and Mathematics in Electrical and Electronic Engineering*, 33(4):1071–1081, 2014.

[HBon] M. W. Hess and P. Benner. Reduced basis modeling for uncertainty quantification of electromagnetic problems in stochastically varying domains. *10th International Conference on Scientific Computing in Electrical Engineering, Springer Series "Mathematics in Industry"*, accepted for publication.

[HGB15] M. W. Hess, Sara Grundel, and P. Benner. Estimating the Inf-Sup Constant in Reduced Basis Methods for Time-Harmonic Maxwell's Equations. *IEEE Transactions on Microwave Theory and Techniques*, 63:3549–3557, 2015.

[HSZ12] J. S. Hesthaven, B. Stamm, and S. Zhang. Certified reduced basis method for the electric field integral equation. *SIAM Journal on Scientific Computing*, 34(3):A1777–A1799, 2012.

[HW08] J. S. Hesthaven and T. Warburton. *Nodal Discontinous Galerkin Methods.* Springer, 2008.

[HRS15] Jan S Hesthaven, Gianluigi Rozza, and Benjamin Stamm. *Certified Reduced Basis Methods for Parametrized Partial Differential Equations.* Springer, 2015.

[HWCW10] J.S. Hesthaven, T. Warburton, C. Chauviere, and L. Wilcox. High-order discontinuous galerkin methods for computational electromagnetics and uncertainty quantification. In J. Roos and L. R. J. Costa, editors, *Scientific Computing in Electrical Engineering SCEE 2008*, volume 14 of *Mathematics in Industry*, pages 403–412. Springer Berlin Heidelberg, 2010.

[HP06] P. Heydari and M. Pedram. Model-order reduction using variational balanced truncation with spectral shaping. *Circuits and Systems I: Regular Papers, IEEE Transactions on*, 53(4):879–891, April 2006.

[Hip02] R. Hiptmair. Finite Elements in computational electromagnetism. *Acta Numerica*, pages 237 – 339, 2002.

[HKC+10] D. B. P. Huynh, D. J. Knezevic, Y. Chen, J. S. Hesthaven, and A. T. Patera. A natural-norm successive constraint method for inf-sup lower bounds. *Comput. Methods Appl. Mech. Engin.*, 199:29 – 33, 2010.

[HRSP07] D. B. P. Huynh, G. Rozza, S. Sen, and A. T. Patera. A successive constraint linear optimization method for lower bounds of parametric coercivity and inf-sup stability constants. *CR Acad. Sci. Paris*, 345(8):473 – 478, 2007.

[Jin11] J. M. Jin. *Theory and Computation of Electromagnetic Fields*. Wiley, 2011.

[Jin14] J. M. Jin. *The Finite Element Method in Electromagnetics*. Wiley, 2014.

[Jun12] N. Jung. *Error Estimation for Parametric Model Reduction and its Application*. PhD thesis, Technical University Munich, 2012.

[KPSC06] B. S. Kirk, J. W. Peterson, R. H. Stogner, and G. F. Carey. `libMesh`: A C++ Library for Parallel Adaptive Mesh Refinement/Coarsening Simulations. *Engineering with Computers*, 22(3–4):237–254, 2006. `http://dx.doi.org/10.1007/s00366-006-0049-3`.

[LKM03] A. Lamecki, P. Kozakowski, and M. Mrozowski. Efficient implementation of the cauchy method for automated CAD-model construction. *IEEE Microwave and Wireless Components Letters*, 13:268–270, 2003.

[LMR12] T. Lassila, A. Manzoni, and G. Rozza. On the approximation of stability factors for general parametrized partial differential equations with a two-level affine decomposition. *ESAIM: Mathematical Modeling and Numerical Analysis*, 46(6):1555–1576, 2012.

[LQR12] T. Lassila, A. Quarteroni, and G. Rozza. A reduced basis model with parametric coupling for fluid-structure interaction problems. *SIAM Journal on Scientific Computing*, 34(2):A1187–A1213, 2012.

[LPS99] Ying Liu, L.T. Pileggi, and A.J. Strojwas. Model order-reduction of RC(L) interconnect including variational analysis. In *Design Automation Conference, 1999. Proceedings. 36th*, pages 201–206, 1999.

[LMW12] A. Logg, K.-A. Mardal, and G. N. Wells. *Automated Solution of Differential Equations by the Finite Element Method*, volume 84 of *Lecture Notes in Computational Science and Engineering*. Springer Berlin Heidelberg, 1st edition, 2012.

[LNS02] S. N. Lophaven, H. B. Nielsen, and J. Søndergaard. DACE-A Matlab Kriging toolbox, version 2.0. Technical report, 2002.

[MA05] M. A. Grepl and A. T. Patera. A posteriori error bounds for reduced-basis approximations of parametrized parabolic partial differential equations. *ESAIM: M2AN*, 39(1):157–181, 2005.

[MMP01] L. Machiels, Y. Maday, and A.T. Patera. Output bounds for reduced-order approximations of elliptic partial differential equations. *Computer Methods in Applied Mechanics and Engineering*, 190(26â27):3413 – 3426, 2001.

[MPR02] Y. Maday, A. T. Patera, and D. V. Rovas. A Blackbox Reduced-Basis Output Bound Method for Noncoercive Linear Problems. *Studies in Mathematics and its Applications*, 31:533 – 569, 2002.

[MPT02] Y. Maday, A. T. Patera, and G. Turinici. Global a priori convergence theory for reduced-basis approximations of single-parameter symmetric coercive elliptic partial differential equations. *Comptes Rendus Mathematique*, 335(3):289 – 294, 2002.

[MPR02] Y. Maday, A.T. Patera, and D.V. Rovas. Chapter 24 - a blackbox reduced-basis output bound method for noncoercive linear problems. In Doina Cioranescu and Jacques-Louis Lions, editors, *Nonlinear Partial Differential Equations and their Applications Collége de France Seminar Volume XIV*, volume 31 of *Studies in Mathematics and Its Applications*, pages 533 – 569. Elsevier, 2002.

[MR02] Y. Maday and E. M. Ronquist. A reduced-basis element method. *Comptes Rendus Mathematique*, 335(2):195 – 200, 2002.

[MN14] A. Manzoni and F. Negri. Rigorous and heuristic strategies for the approximation of stability factors in nonlinear parametrized PDEs. Technical report, Mathematics Institute of Computational Science and Engineering, École Polytechnique Fédérale de Lausanne, Feb 2014.

[Mon03] P. Monk. *Finite Element Methods for Maxwell's Equations*. The Clarendon Press Oxford University Press, 2003.

[MWWI00] I. Munteanu, T. Wittig, T. Weiland, and D. Ioan. FIT/PVL circuit-parameter extraction for general electromagnetic devices. *IEEE Transactions on Magnetics*, 36 (4):1421 – 1425, 2000.

[Nag79] D. A. Nagy. Modal representation of geometrically nonlinear behavior by the finite element method. *Computers & Structures*, 10(4):683 – 688, 1979.

[NS10] T. V. Narayanan and M. Swaminathan. Preconditioned second-order multi-point passive model reduction for electromagnetic simulations. *IEEE Transactions on Microwave Theory and Techniques*, 58:2856 – 2866, 2010.

[Ned80] Jean-Claude Nedelec. Mixed finite elements in R^3. *Numerische Mathematik*, 35(3):315–341, Sep 1980.

[NRP09] N.-C. Nguyen, G. Rozza, and A. T. Patera. Reduced basis approximation and a posteriori error estimation for the time-dependent viscous Burgers equation. *Calcolo*, 46(3):157–185, 2009.

[Noo80] A. K. Noor. Reduced basis technique for nonlinear analysis of structures. *AIAA Journal*, 18(4):455 – 462, 1980.

[Oug06] K. E. Oughstun. *Electromagnetic and Optical Pulse Propagation 1: Spectral Representations in Temporally Dispersive Media*. Electromagnetic and Optical Pulse Propagation. Springer, 2006.

[PT97] A. Papageorgiou and J. F. Traub. Faster evaluation of multidimensional integrals. *Comput. Phys.*, 11(6):574–578, January 1997.

[PBWB14] B. Peherstorfer, D. Butnaru, K. Willcox, and H.-J. Bungartz. Localized discrete empirical interpolation method. *SIAM Journal on Scientific Computing*, 36(1):A168–A192, 2014.

[PR90] L. T. Pillage and R. A. Rohrer. Asymptotic waveform evaluation for timing analysis. *IEEE Trans. Computer Aided Design*, 9:352 – 366, 1990.

[PDEL97] S. V. Polstyanko, R. Dyczij-Edlinger, and J.-F. Lee. Fast frequency sweep technique for the efficient analysis of dielectric waveguides. *IEEE Transactions on Microwave Theory and Techniques*, 45:1118 – 1126, 1997.

[Pom10] J. Pomplun. *Reduced Basis Method for Electromagnetic Scattering Problems*. PhD thesis, Free University Berlin, 2010.

[PRV+01] C. Prudâhomme, D. V. Rovas, K. Veroy, L. Machiels, Y. Maday, A. T. Patera, and G. Turinici. Reliable real-time solution of parametrized partial differential equations: Reduced-basis output bound methods. *J. Fluids Eng.*, 124(1):70 – 80, 2001.

[RLM15] M. Rewienski, A. Lamecki, and M. Mrozowski. A goal-oriented error estimator for reduced basis method modeling of microwave devices. *Microwave and Wireless Components Letters, IEEE*, 25(4):208–210, April 2015.

[Roz09] G. Rozza. An introduction to reduced basis method for parametrized PDEs. *Applied and Industrial Mathematics in Italy (W. Scientific, ed.)*, 3:508 – 519, 2009.

[RHM13] G. Rozza, D. B. P. Huynh, and A. Manzoni. Reduced basis approximation and a posteriori error estimation for stokes flows in parametrized geometries: roles of the inf-sup stability constants. *Numerische Mathematik*, 125(1):115–152, 2013.

[RHP08] G. Rozza, D. B. P Huynh, and A. T. Patera. Reduced Basis Approximation and a Posteriori Error Estimation for Affinely Parametrized Elliptic Coercive Partial Differential Equations. *Archives of Computational Methods in Engineering*, 15:229 – 275, 2008.

[RIB13] T. Rylander, P. Ingelström, and A. Bondeson. *Computational Electromagnetics*. Springer, New York, 2013.

[SDK09] M. K. Sampath, A. Dounavis, and R. Khazaka. Parametrized model order reduction techniques for FEM based full wave analysis. *IEEE Transactions on Advanced Packaging*, 32:2 – 12, 2009.

[SC12] D. Schmidthaeusler and M. Clemens. Low-Order Electroquasistatic Field Simulations Based on Proper Orthogonal Decomposition. *IEEE Transactions on Magnetics*, 48:567 – 570, 2012.

[Sch03] A. Schneebeli. An H(curl;Ω)-conforming FEM: Nédélec's elements of first type. Technical report, 2003.

[Sen07] S. Sen. *Reduced Basis Approximation and A Posteriori Error Estimation for Non-Coercive Elliptic Problems: Application to Acoustics*. PhD thesis, Massachusetts Institute of Technology, 2007.

[Sen08] S. Sen. Reduced-basis approximation and a posteriori error estimation for many-parameter heat conduction problems. *Numerical Heat Transfer, Part B: Fundamentals*, 54(5):369–389, 2008.

[SVH+06] S. Sen, K. Veroy, D.B.P. Huynh, S. Deparis, N.C. Nguyen, and A.T. Patera. Natural norm a posteriori error estimators for reduced basis approximations. *Journal of Computational Physics*, 217(1):37 – 62, 2006. Uncertainty Quantification in Simulation Science.

[Sta12] K. K. Stavrakakis. *Model Order Reduction Methods for Parametrized Systems in Electromagnetic Field Simulations*. PhD thesis, Technical University Darmstadt, 2012.

[SWAW09] K. K. Stavrakakis, T. Wittig, W. Ackermann, and T. Weiland. Linearization of Parametric FIT-Discretized Systems for Model Order Reduction. *IEEE Transactions on Magnetics*, 45:1380 – 1383, 2009.

[Ste99] M. L. Stein. Interpolation of Spatial Data. Some Theory for Kriging. *New York, NY: Springer*, 1999.

[TMN14] L. Tamellini, O. Le Maitre, and A. Nouy. Model reduction based on proper generalized decomposition for the stochastic steady incompressible Navier–Stokes equations. *SIAM Journal on Scientific Computing*, 36(3):A1089–A1117, 2014.

[VHFP11] S. Vallaghe, A. Le Hyaric, M. Fouquembergh, and C. Prud'homme. A successive constraint method with minimal offline constraints for lower bounds of parametric coercivity constant. Technical report, 2011.

[VB96] L. Vandenberghe and S. Boyd. Semidefinite programming. *SIAM Rev.*, 38(1):49–95, March 1996.

[VP05] K. Veroy and A. T. Patera. Certified real-time solution of the parametrized steady incompressible Navier-Stokes equations: rigorous reduced-basis a posteriori error bounds. *International Journal for Numerical Methods in Fluids*, 47(8-9):773–788, 2005.

[VPP03] Karen Veroy, Christophe Prud'homme, and Anthony T. Patera. Reduced-basis approximation of the viscous Burgers equation: rigorous a posteriori error bounds. *Comptes Rendus Mathematique*, 337(9):619 – 624, 2003.

[Wei77] T. Weiland. A discretization method for the solution of Maxwell's equations for six-component fields. *Electron. Commun. AEUE*, 31(3):116 – 120, 1977.

[Wie13] B. Wieland. *Reduced Basis Methods for Partial Differential Equations with Stochastic Influences*. PhD thesis, Ulm University, 2013.

[WMSW02] T. Wittig, I. Munteanu, R. Schuhmann, and T. Weiland. Two-Step Lanczos algorithm for model order reduction. *IEEE Transactions on Magnetics 38*, 2:673 – 676, 2002.

[WSW06] T. Wittig, R. Schuhmann, and T. Weiland. Model order reduction for large systems in computational electromagnetics. *Linear Algebra and its Applications*, 415:499 – 530, 2006.

[XH05] D. Xiu and J. S. Hesthaven. High-order collocation methods for differential equations with random inputs. *SIAM Journal on Scientific Computing*, 27(3):1118–1139, 2005.

[XT06] D. Xiu and D. M. Tartakovsky. Numerical methods for differential equations in random domains. *SIAM Journal on Scientific Computing*, 28(3):1167 – 1185, 2006.

[YZC06] Yu Y. Zhu and A. C. Cangellaris. *Multigrid finite element methods for electromagnetic field modeling*. IEEE Press series on electromagnetic wave theory. Piscataway, N.J. IEEE Press Hoboken, N.J. Wiley-Interscience, 2006.

[Yue12] Y. Yue. *The Use of Model Order Reduction in Design Optimization Algorithms (Het gebruik van modelreductie in algoritmen voor ontwerpoptimalisatie)*. PhD thesis, Numerical Analysis and Applied Mathematics Section, Department of Computer Science, Faculty of Engineering Science, November 2012. Meerbergen, Karl (supervisor).

[Zag06] S. Zaglmayr. *High Order Finite Element Methods for Electromagnetic Field Computation*. PhD thesis, JKU Linz, 2006.

[ZFLB15] Y. Zhang, L. Feng, S. Li, and P. Benner. Accelerating pde constrained optimization by the reduced basis method: application to batch chromatography. *International Journal for Numerical Methods in Engineering*, 2015.

[ZDP00] T. Zhou, S. L. Dvorak, and J. L. Prince. Application of the Pade via Lanczos (PVL) algorithm to electromagnetic systems with expansion

at infinity. In *Proc. of 2000 Electronic Components and Technology Conference*, pages 1515 – 1520, 2000.

Statement of Scientific Cooperations

The work at hand has been developed in cooperation with various coauthors. In the following, the contributions of the coauthors are clarified. The following people contributed to this work:

- Peter Benner (PB), Max Planck Institute for Dynamics of Complex Technical Systems;
- Christopher Beattie (CB), Virginia Tech;
- Jan Hesthaven (JH), EPFL;
- Sara Grundel (SG), Max Planck Institute for Dynamics of Complex Technical Systems.

8.1 Chapter 4

PB provided the idea to pursue this topic and advised during the ongoing work.

8.2 Chapter 5

PB advised during the ongoing work, SG provided the Kriging method section 5.3.4 and numerical computations and CB provided the section 5.4 on the SCM with matrix-valued constraints.

8.3 Chapter 6

PB provided the idea to pursue this topic and advised during the ongoing work.

8.4 Chapter 7

JH provided the idea to pursue this topic and advised during the ongoing work.

Magdeburg, 22nd February 2016

Declaration of Honor

I hereby declare that I produced this thesis without prohibited assistance and that all sources of information that were used in producing this thesis, including my own publications, have been clearly marked and referenced.

In particular I have not wilfully:

- Fabricated data or ignored or removed undesired results.
- Misused statistical methods with the aim of drawing other conclusions than those warranted by the available data.
- Plagiarised data or publications or presented them in a disorted way.

I know that violations of copyright may lead to injunction and damage claims from the author or prosecution by the law enforcement authorities.

This work has not previously been submitted as a doctoral thesis in the same or a similar form in Germany or in any other country. It hast not previously been published as a whole.

Magdeburg, the 22nd February 2016

Schriftliche Ehrenerklärung

Ich versichere hiermit, dass ich die vorliegende Arbeit ohne unzulässige Hilfe Dritter und ohne Benutzung anderer als der angegebenen Hilfsmittel angefertigt habe; verwendete fremde und eigene Quellen sind als solche kenntlich gemacht.

Ich habe insbesondere nicht wissentlich:

- Ergebnisse erfunden oder widersprüchliche Ergebnisse verschwiegen,
- statistische Verfahren absichtlich missbraucht, um Daten in ungerechtfertigter Weise zu interpretieren,
- fremde Ergebnisse oder Veröffentlichungen plagiiert oder verzerrt wiedergegeben.

Mir ist bekannt, dass Verstöße gegen das Urheberrecht Unterlassungs- und Schadenersatzansprüche des Urhebers sowie eine strafrechtliche Ahndung durch die Strafverfolgungsbehörden begründen kann.

Die Arbeit wurde bisher weder im Inland noch im Ausland in gleicher oder ähnlicher Form als Dissertation eingereicht und ist als Ganzes auch noch nicht veröffentlicht.

Magdeburg, den 22. 02. 2016